Department of Precision and Microsystems Engineering

Automation of the clipping process in cryogenic electron tomography

Ronald van den Berg

Report no	:	2021.002
Coach	:	Thomas van der Heijden
Professor	:	Jo Spronck
Specialisation	:	MSD
Type of report	:	Master Thesis
Date	:	22 December 2020

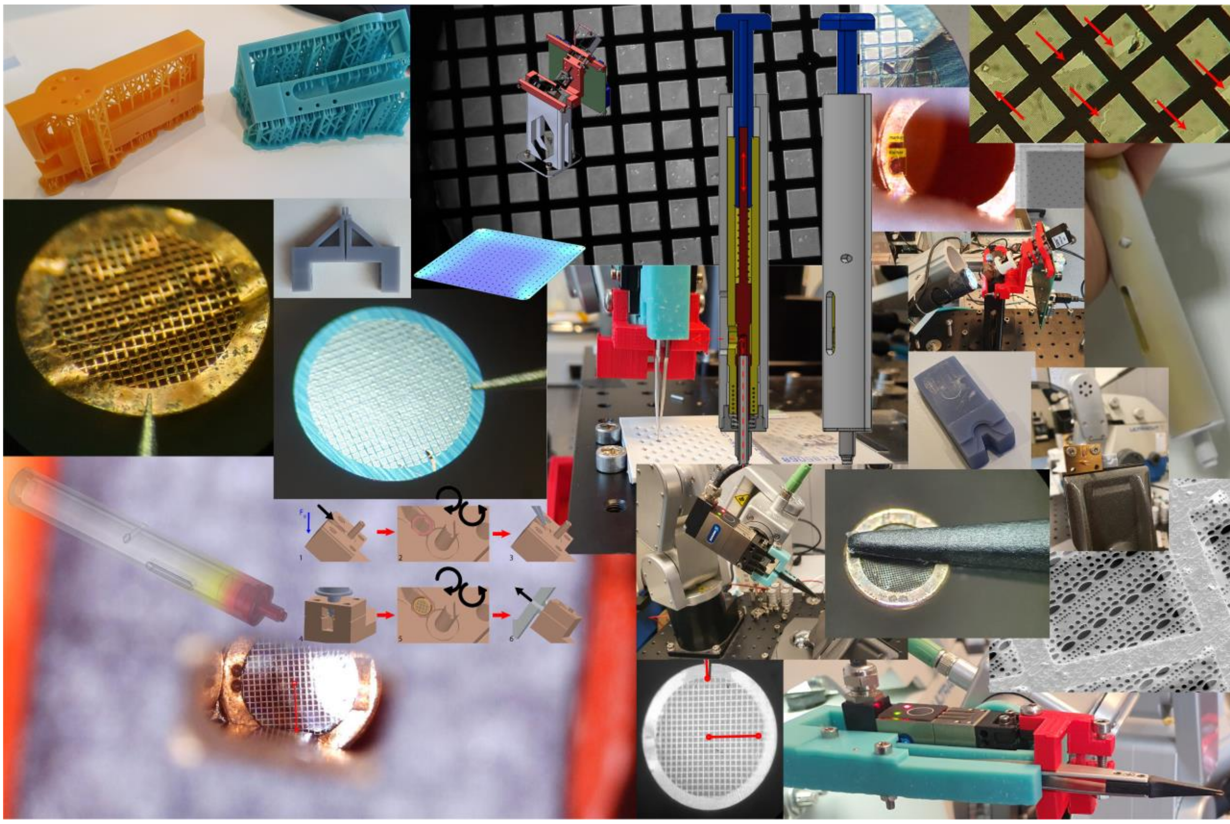

TU Delft Delft University of Technology

Challenge the future

Preface

Before you lies my thesis report: "Automation of the clipping process in cryogenic electron tomography". Looking back, I am happy and grateful that I could do my graduation project at Delmic. In the period I spent at Delmic I feel like I've learned a lot, and I am content with the final result.

Many thanks to Thomas van der Heijden for all the help and useful advice while supervising this project. Also, I would like to thank Jo Spronck from the TU Delft for giving good advice with perfect timing. Of course I would also like to thank all students and professors from the PME department who contributed during Monday morning meetings, and last, but definitely not least all other colleagues at Delmic who contributed and helped me out: Sander den Hoedt, Marcin Zielinski, Bas Bikker, Daan Boltje, Thera Pals, and all others.

I hope you enjoy your reading.

R. D. van den Berg
Delft, December 2020

Summary

Introduction Cryogenic electron tomography (cryo-ET) is currently the golden standard for observing cellular tissue at nanometer resolution. By imaging samples in different angles, a 3D representation of cellular tissue can be reconstructed. The workflow where you start with cellular tissue until you obtain the final image is however still very expensive, time-consuming, and labor-intensive. Moreover, some of the manual steps present in the current procedure can take over a year to master. Even after mastering all steps, the current procedure still has a low yield. Currently this promising technique is therefore only available to a select group of researchers capable of performing all the steps of this procedure. Automation shows great potential to solve these problems. If the cryo-ET workflow would be automated, this technique could be made available to a broader group of researchers. This would allow for the fast generation of large quantitative data sets, which would have a major beneficial effect on the progression of research aimed at targeting viruses (e.g. SARS-CoV-2, HIV-1, Dengue, and many more). Clipping of the Autogrid is a procedure in the cryo-ET workflow with a low yield, which could be majorly improved by automation. This procedure consists of four steps: c1) Autogrid cartridge placement, c2) TEM-grid placement, c3) c-clip insertion, and c4) retrieval of the clipped Autogrid. An illustration of these four steps is included in this abstract for reference (Figure 1). The aim of this project is to improve and automate the current clipping of the Autogrid, thereby increasing the yield of the cryo-ET workflow. A problem analysis was performed to investigate potential sources of damage during clipping (that were previously proposed in a literature survey), and to identify other problems during clipping.

Problem analysis The following four hypotheses on the potential sources of damage in the current clipping procedure were investigated: h_1) improper handling with tweezers causes damage of the TEM-grids, h_2) a volume (e.g. air or liquid nitrogen) is trapped between the current c-clip insertion tool and the thin carbon layer on the TEM-grid in the third clipping step (c_3) causing this layer to rupture, h_3) a rigid connection between the c-clip insertion tool and the c-clip allows for applying too much force on the TEM-grid through the c-clip, and h_4) the uncontrolled downwards motion of the c-clip causes damage on impact.

Automating the clipping procedure could majorly reduce damage of TEM-grids if the first hypothesis (h_1) were to be true. Automating the current clipping procedure would however not reduce damage caused by the second hypothesis (h_2). Multiscale modelling using finite element (FE) analyses was used to investigate the second hypothesis. Two models were used to first calculate the increase in air pressure between the current c-clip insertion tool and the TEM-grid, and then the effect of this increased air pressure on the thin holey carbon layer on the TEM-grid. Results of these analyses could not falsify the second hypothesis. Therefore, further experimental testing was required to investigate the second hypothesis. A free body diagram was used to investigate hypotheses h_3 and h_4. Based on these analytical calculations, hypothesis h_3 was still likely to be a cause of reduced yield in the current clipping procedure.

Other than a low yield, two other problems in the current clipping procedure were identified: p_1) the orientation of the TEM-grid with respect to the Autogrid cartridge is very hard to control, and p_2) the orientation of the clipped Autogrid with respect to the tweezers retrieving the clipped Autogrid is very hard to control.

Proposed solutions and methods for experimental testing A new procedure consisting of six clipping steps (C_1, C_2, C_3, C_4, C_5, and C_6) was proposed to solve the problems that were identified in the problem analysis (p_1 and p_2). In this procedure, two extra steps were included between the first and second clipping step (c_1 and c_2), and between the third and fourth clipping step (c_3 and c_4), of the old clipping procedure. In these two steps the Autogrid cartridge is rotated to a preferred orientation (C_2) before placing the TEM-grid (in C_3), and the Autogrid is rotated to a preferred orientation (C_5) before retrieving the Autogrid in the last step (C_6) of the new procedure. An illustration of the proposed new clipping procedure is given at the end of this summary for reference (Figure 2).

A new c-clip insertion tool was developed which allows for air or other mediums to flow through the c-clip insertion tool and which has a force-limiting mechanism. This new tool was used to test the second and third hypothesis on the potential sources of damage during clipping (h_2 and h_3). A FE analysis was performed

to analyse the heat distribution under cryogenic conditions in the new c-clip insertion tool with the selected materials. In the first experiment (experiment 1), this new c-clip insertion tool was compared with the current c-clip insertion tool. Four Autogrids were clipped with this new c-clip insertion tool and four Autogrids were clipped with the current c-clip insertion tool. All Autogrids were clipped under cryogenic conditions by an experienced user. Cryogenic light microscopy images of the carbon layer on the TEM-grids before and after clipping were used to compare the yield between the new and old c-clip insertion tool.

An Autogrid holder was developed to rotate the Autogrid cartridge and the clipped Autogrid in clipping steps C_2 and C_5. This rotation was used to solve problems p_1 and p_2. Two algorithms were developed to detect the markers on the bottom of the Autogrid cartridge: an algorithm using a Circular Hough Transform (CHT) and a Machine Learning (ML) algorithm. In the second experiment (experiment 2) these algorithms were experimentally compared (experiment 2A). Both algorithms were used to detect markers on the bottom of an Autogrid cartridge on 164 images. The detected markers were classified as true positive (TP), false negative (FN), and false positive (FP). From these three variables, the precision (P), recall (R), and F1 score were calculated. A paired samples t-test was used to compare the values for these six metrics (TP, FN, FP, P, R, and F1) between the two algorithms. Then, based on this experimental comparison, one of the algorithms was selected to be used in a proof of concept experiment (experiment 2B) in which a stepper motor was connected to the Autogrid holder to automatically obtain an orientation of the Autogrid cartridge where two markers are on the left side of the image. This proof-of-concept experiment was performed seven consecutive times.

Four gripper fingers (g_1, g_2, g_3, and g_4) for automatic handling of the Autogrid (cartridge) were designed, manufactured, and used in preliminary experiments. All gripper fingers were designed for, and tested with, the Mecademic Meca 500 six-axis industrial robot arm and the Mecademic MEGP 25 parallel gripper. Based on preliminary experiments, one of these four gripper fingers (g_3) was selected for the third experiment (experiment 3). In experiment 3 a clipped Autogrid was retrieved from the Autogrid holder seven times. The orientation of the Autogrid in the Autogrid holder was imaged using an USB-microscope. The orientation of the Autogrid after retrieving it was imaged using a different microscope next to the test setup. Images of the Autogrid orientation before and after retrieval were compared to investigate if the desired orientation was retained during retrieval.

All four gripper fingers mentioned above (g_1, g_2, g_3, and g_4) were used to automatically handle TEM-grids in preliminary experiments. One new pair of gripper fingers (g_5) was designed, manufactured, and used in the same preliminary experiments. This new pair of gripper fingers was selected for experiment 4. An algorithm was developed to map the orientation of the TEM-grid with respect to these gripper fingers to the Autogrid cartridge. Experiment 4 was divided in two sub-experiments. In experiment 4A two golden TEM-grids and five TEM-grids made of copper were automatically retrieved from a TEM-grid storage box and placed in an Autogrid cartridge. The carbon layer on these TEM-grids was imaged before and after placement, and damage of the carbon layer was quantified and compared. In Experiment 4B, five TEM-grids were placed in an Autogrid cartridge. The orientation of the TEM-grid with respect to the gripper fingers was mapped to the Autogrid cartridge ten times for each TEM-grid. This mapped orientation was compared to the orientation of the TEM-grid after placement, and the difference was reported.

Results from four experiments In experiment 1, the following values were obtained when quantifying the damage on the TEM-grids: The mean relative values for the total damaged grid holes after clipping that were not damaged before clipping with respect to the total amount of grid holes that were undamaged after clipping were 0.7% and 0.0% for the old and new c-clip insertion tool, respectively. The mean relative values of the total amount of grid holes that were damaged after clipping with respect to the total amount of grid holes that were undamaged after clipping were 1.4% and 1.9% for the old and new c-clip insertion tool, respectively.

In experiment 2A, marker detection using a ML approach performed significantly better then marker detection using a CHT approach, on all six metrics (TP, FN, FP, P, R, and F1). Using a ML approach while masking the center of the Autogrid yielded the best results with a mean (± SD) TP, FP, FN, P, R, and F1-score of 2.0 (± 0.3), 0.7 (± 0.9), 0.1 (± 0.3), 0.81 (± 0.22), 0.96 (± 0.11), and 0.86 (± 0.15), respectively.

In experiment 2B, the ML algorithm was successfully used to automatically rotate the Autogrid to an orientation where two markers were on the left side of the image seven consecutive times.

In experiment 3, in five out of seven tests, the Autogrid did not change orientation while automatically retrieving it from the Autogrid holder. In two out of seven tests, the orientation of the Autogrid did change. The orientation changed once while closing the gripper fingers, and once while retrieving the Autogrid after closing the gripper fingers.

In experiment 4A, the carbon layer on one of the two golden TEM-grids was successfully imaged before and after placement in the Autogrid cartridge. The only new location where the carbon layer on the TEM-grid was damaged, was the location on the TEM-grid where the gripper fingers were positioned too far over the rim of the TEM-grid. The other golden TEM-grid was successfully placed, but the manual retrieval of the Autogrid cartridge with TEM-grid inside was not successful. Two out of the five copper grids were successfully placed and imaged. The other three copper grids were successfully placed, but were unsuccessfully retrieved manually after placement (two TEM-grids), or images were obtained of insufficient quality (one TEM-grid). One of the TEM-grids that was successfully placed and imaged, did not show any newly damaged locations after placement. The other TEM-grid that was successfully placed and imaged only showed a damaged location where the gripper fingers were applied too far over the rim of the TEM-grid.

In Experiment 4B, the mean (± SD) difference between the mapped orientation of the TEM-grid in the Autogrid cartridge with the obtained orientation of the TEM-grid in the Autogrid cartridge for all 50 analyses was: 4.9°(± 2.4°). Compared to this mean standard deviation over all 50 analyses, the standard deviation of the difference between the mapped orientation and the obtained orientation within one TEM-grid was lower for all TEM-grids (SD = 1.4°, 1.0°, 0.7°, 1.7°, and 0.8°).

Discussion and conclusions In experiment 1, both for the current c-clip insertion tool and for the new c-clip insertion tool, the amount of damage on the TEM-grids was a lot less than anticipated. Moreover, the difference between the old and new c-clip insertion tool was small (< 1%). The time between the first encounter with the experienced user performing the test and testing of the new c-clip insertion tool was approximately 5 months. In this time period the experienced user had further mastered the technique of c-clip insertion. These results suggest that the only source of damage during the clipping process is human error. Automating the process of c-clip insertion is therefore likely to reduce the damage induced in this step to almost zero. Although the obtained results suggest that a yield near to 100% can be reached, future experiments in which the effect of samples present on the TEM-grid on the damage caused by c-clip insertion is investigated are required. A new design was proposed showing how already available components can be used to test such an automated c-clip insertion tool. This design includes the manufactured new clipping pen with one adjusted part, two plates, and the stepper motor that was used in experiment 2.

In experiment 2, the ML approach for marker detection performed significantly better than the CHT approach. Furthermore, the performance of the ML algorithm was well enough to be used in a proof of concept experiment where the orientation of the Autogrid was automatically set. Predictions were however not perfect. Other approaches to training the data where half visible markers are not included might improve the algorithm. Also, a more stable test setup with constant lighting conditions might help further improve the detection of markers.

In experiment 3, results suggested that the current gripper fingers could be used for retrieving the Autogrid from the Autogrid holder while retaining the orientation of the Autogrid. However, in two out of the seven tests in which the Autogrid was retrieved, the orientation of the Autogrid was not retained. Using a combination of different tweezers with the selected gripper fingers could improve the retention of the orientation of the Autogrid during retrieval. Also, better alignment procedures using a microscope, and a stable test setup could help improve the retention of orientation during Autogrid retrieval.

In experiment 4A, TEM-grids were successfully placed in the Autogrid cartridge using the selected gripper fingers. Because alignment of the gripper fingers with the TEM-grids was done manually (by eye), with two of the three TEM-grids (one golden and one made of copper) where all of the steps in this experiment succeeded, the points of the gripper fingers were slightly over the rim of the TEM-grid causing damage of the carbon layer at those locations. No other new damaged locations were observed on these two TEM-grids. Moreover, on the other TEM-grid (copper) with which all steps of the experiment succeeded, no new damaged locations were observed. These results suggest that when correctly aligning the selected gripper fingers with the rim of the TEM-grid, TEM-grids could be handled without damaging them in the process. In a final automated workflow, these gripper fingers should be well aligned. A test setup including a microscope that has an adjustable position could further improve this alignment. Such a microscope could also be used for obtaining images of the sample and for obtaining the images required for mapping the orientation of the TEM-grid to the Autogrid cartridge.

In experiment 4B, the orientation of the TEM-grid was successfully mapped to the Autogrid cartridge. The mean difference between the mapped orientation and the orientation obtained after placing the TEM-grid in the Autogrid cartridge, was well below an acceptable value when comparing this to the situation where it is not possible to adjust this orientation in the current clipping procedure. Some variation in the difference between these orientations is explained by the methods that were used for mapping the orientation of the TEM-grid to the Autogrid cartridge. Since the standard deviation of the difference within one TEM-grid placement test was smaller than the standard deviation over all tests, some variation is likely to come from a slightly adjusted orientation during placement of the TEM-grid. A more stable test-setup, better alignment procedures, and an improvement mapping algorithm, could further improve the mapping of the orientation of the TEM-grid to the Autogrid cartridge. Even without these adjustments the proposed method can already be considered as an improvement to the current procedure.

In general, experimental results of the different developed solutions for all clipping steps showed great potential of being implemented into a final automated solution. Although only c-clip insertion was tested at cryogenic temperature, results for all clipping steps look promising and no insurmountable problems were expected when testing at cryogenic temperatures. Follow-up experiments are required to confirm these expectations. Moreover, by using the current gripper fingers designed for automatic TEM-grid handling, the clipping procedure can be connected to the plunge freezing step. Plunge freezing is the step before clipping the Autogrid in the cryo-ET workflow. The proposed solution can thereby be used as connecting link for full automation of the cryo-ET workflow.

A final automated solution for clipping should include a stable environment with constant lighting conditions, a microscope that can be used for alignment procedures and for mapping the orientation of the TEM-grid, and either two robot arms or one robot arm with interchangeable gripper fingers. This solution to automatic clipping can then easily be extended to include plunge freezing and potentially even include the handling steps before plunge freezing.

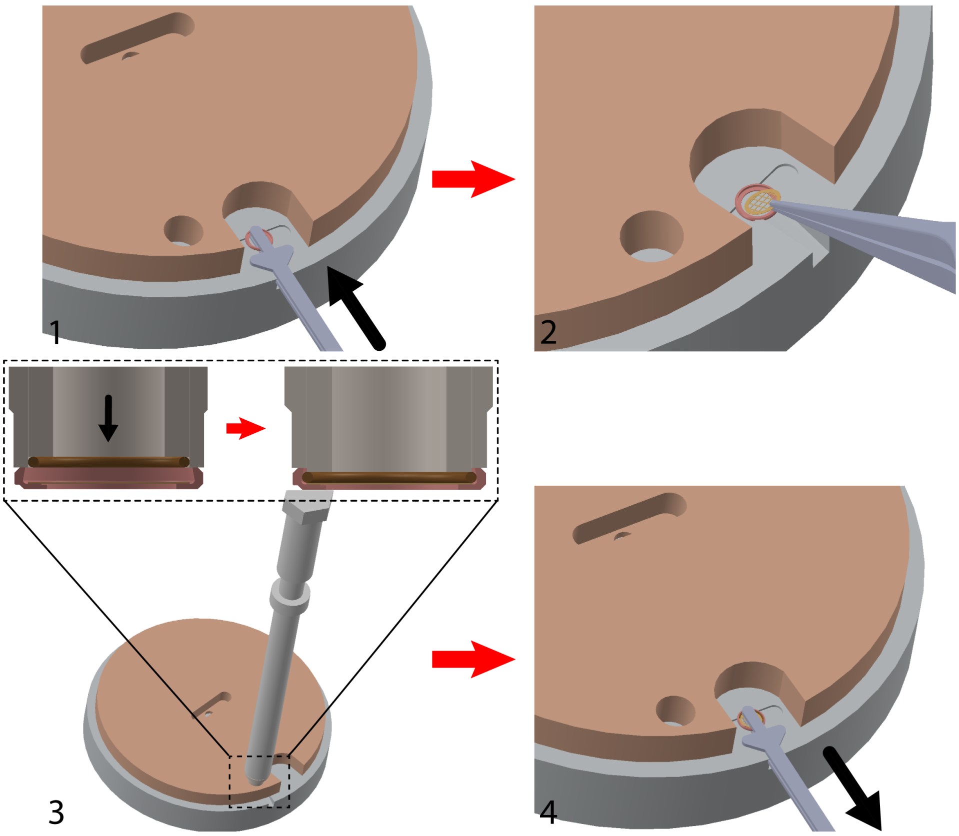

Figure 1: Illustration of the four steps (c_1, c_2, c_3, c_4) involved in clipping the Autogrid: c_1 Autogrid cartridge placement, c_2 TEM-grid placement, c_3 c-clip insertion, and c_4 retrieval of the clipped Autogrid.

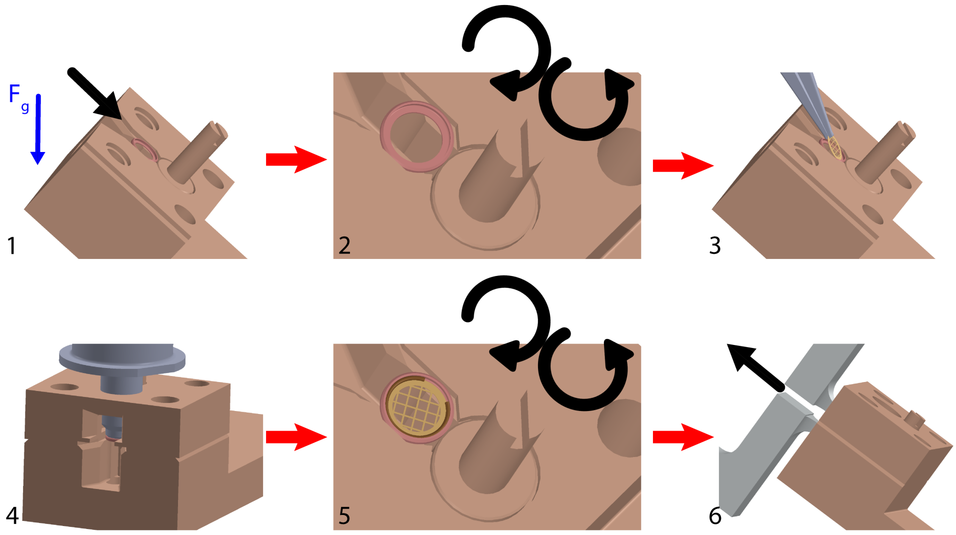

Figure 2: The six steps of the proposed new clipping procedure: C_1 Autogrid cartridge placement, C_2 rotation of the Autogrid cartridge to the preferred orientation, C_3 placement of the TEM-grid, C_4 c-clip insertion, C_5 rotation of the clipped Autogrid to the preferred orientation, C_6 retrieval of the clipped Autogrid. Variable F_g represents the gravitational force which is at an angle with the Autogrid holder.

Terminology and definitions

All terminology used in this report is listed below

Abbreviations

CHT_{mc} Circular Hough Transform masked center of the Autogrid

CHT Circular Hough Transform

cryo-CLEM Cryogenic Correlative Light and Electron Microscopy.

Cryo-FIB Cryogenic Focused Ion Beam, also used to refer to the apparatus using the focused ion beam.

Cryo-LM Cryogenic Light Microscope/Microscopy

FE Finite Element

FIB-SEM Focused Ion Beam Scanning Electron Microscope.

ML_{mc} Machine Learning masked center of the Autogrid

ML Machine Learning

PCB Printed Circuit Board

ROI Region Of Interest

SD Standard Deviation

SEM Scanning Electron Microscope/Microscopy

SLA Stereolithography

SPA Single-Particle Analysis

TEM Transmission Electron Microscope/Microscopy

Definitions

Autogrid Cartridge The ring in which a TEM-grid is placed when clipping the Autogrid.

Autogrid holder The designed holder that has a mechanism for rotating the Autogrid. The design for the Autogrid holder is described in Section 4.3.1.

Autogrid tweezers A type of tweezers that are specifically designed to handle Autogrids.

Autogrid Assembly of a TEM-grid and an Autogrid cartridge held together by a retaining ring also referred to as c-clip.

C-clip insertion tool See clipping pen.

C-clip The retaining ring that is inserted in an Autogrid cartridge to keep the TEM-grid that is inside, in place.

Clipping pen The tool that inserts the c-clip in the third clipping step, also referred to as c-clip insertion tool. The new clipping pen is the one that was designed for testing hypotheses h_2 and h_3. The old or current clipping pen is the clipping that is currently used to insert the c-clip in the cryo-ET workflow.

Clipping station The dedicated station in which all four clipping steps are performed.

Clipping the Autogrid The process where an Autogrid cartridge, TEM-grid, and c-clip are assembled into an Autogrid. Four steps in the clipping proces were identified (c_1, c_2, c_3, and c_4).

Confusion matrix A matrix that consists of TP, FP, FN, and TN. For object detection within an image, TN is not included.

Contamination Water molecules in the air around a frozen sample can stick to the outside of the sample and freeze. This causes the formation of crystalline ice on the outside of a vitrified sample over time.

Con and the total number of holes with carbon layer on the TEM-grid that were to contaminated with ice to determine if they were damaged in experiment 1.

Cryo-compatible Compatible with cryogenic conditions.

Cryo-ET Abbreviation for cryogenic Electron Tomography. Cryo-ET is defined as the entire process described in Section 2.2.

Cryofixation Fixating a sample by freezing it.

DaDb the total number of holes with carbon layer on the TEM-grid that were damaged after clipping and were damaged before clipping in experiment 1 (Damaged after Damaged before).

DaUb the total number of holes with carbon layer on the TEM-grid that were damaged after clipping and were not visible on the image before clipping in experiment 1 (Damaged after Unknown before).

DaUDb the total number of holes with carbon layer on the TEM-grid that were damaged after clipping but were undamaged before clipping in experiment 1 (Damaged after UnDamaged before).

Experiment 1 The first experiment that was not of preliminary nature. In this experiment the new and current c-clip insertion tool were compared. Methods, results, and discussion are given in Subsection 4.2.3, Section 5.1, and Section 6.1, respectively.

Experiment 2A In this experiment the different approaches to marker detection were compared. Methods, results, and discussion are given in Subsection 4.3.3, Subsection 5.2.1, and Subsection 6.2.1, respectively.

Experiment 2B In this proof-of-concept experiment the Autogrid was automatically rotated to a specified orientation. Methods, results, and discussion are given in Subsection 4.3.3, Subsection 5.2.2, and Subsection 6.2.2, respectively.

Experiment 3 In this experiment the Autogrid was automatically retrieved. Methods, results, and discussion are given in Subsection 4.4.3, Section 5.3, and Section 6.3, respectively.

Experiment 4A In this experiment the TEM-grid was automatically placed in the Autogrid cartridge, and damage was quantified. Methods, results, and discussion are given in Subsection 4.5.3, Subsection 5.4.1, and Subsection 6.4.1, respectively.

Experiment 4B In this experiment the TEM-grid was automatically placed in the Autogrid cartridge, and the orientation was mapped and compared. Methods, results, and discussion are given in Subsection 4.5.3, Subsection 5.4.2, and Subsection 6.4.2, respectively.

Gripper fingers For this report, the gripper fingers are defined as everything between the grippers and the object that is to be handled by the grippers. More specifically, the gripper fingers are everything between the MEGP 25 grippers and either the Autogrid or the TEM-grid.

Grippers In this report grippers refers to the MEGP 25 parallel grippers.

Lamella The thin section that is created using FIB milling.

Plunge freezing The process where a sample is vitrified by rapidly plunging it into a cryogen.

Sample carrier Samples (often) cannot be placed directly in a TEM, they are supported by a sample carrier. In the context of this report, sample carrier will refer to a TEM-grid.

TDa the total number of holes with carbon layer on the TEM-grid that were damaged after clipping in experiment 1 (Total Damaged after clipping).

TEM-grid Abbreviation for Transmission Electron Microscopy grid. This TEM-grid is used as sample carrier in a TEM. The TEM-grid consists of a round grid-like structure that is there to support a very thin electron transparent layer.

TUD the total number of holes with carbon layer on the TEM-grid that were not damaged after clipping in experiment 1 (Total UnDamaged).

Vitrification Process of freezing while forming noncrystalline ice.

Symbols

c_1, c_2, c_3, c_4 The four steps in the currently used clipping procedure: c_1: Autogrid cartridge placement, c_2: TEM-grid placement, c_3: c-clip insertion, and c_4: retrieval of the clipped Autogrid.

$C_1, C_2, C_3, C_4, C_5, C_6$ The six steps in the proposed new clipping procedure: C_1: Autogrid cartridge placement, C_2: rotation of the Autogrid cartridge to the preferred orientation, C_3: placement of the TEM-grid, C_4: c-clip insertion, C_5: rotation of the clipped Autogrid to the preferred orientation, C_6: retrieval of the clipped Autogrid.

$g_1, g_2, g_3, g_4, g_5, g_6$ The different gripper fingers that were used for preliminary testing explained in Section 4.4 and Section 4.5.

h_1, h_2, h_3, h_4 The four hypotheses concerning the sources of damage during the current clipping procedure: h_1: improper handling with tweezers causes damage of the TEM-grids, h_2: air or another medium (e.g. liquid nitrogen, or liquid nitrogen vapour) is trapped between the current c-clip insertion tool and the thin carbon layer on the TEM-grid in the third clipping step (c_3) causing this layer to rupture, h_3: a rigid connection between the c-clip insertion tool and the c-clip allows for applying too much force on the TEM-grid resulting in damage, and h_4: the uncontrolled downwards motion of the c-clip causes damage on impact.

$M1$, $M1C$, $M2$ The three FE models used to investigate the effect of an increasing air pressure on the carbon layer on a TEM-grid. A more elaborate explanation is given in Subsection 3.3.2

m_1, m_2, m_3, m_4 The four main steps of cryo-ET: m_1: plunge freezing, m_2: cryo-LM, m_3: cryo-FIB, m_4: cryo-TEM

p_1, p_2 The two problems in the current clipping procedure that were defined in Section 3.5. p_1: The orientation of the TEM-grid with respect to the Autogrid cartridge is very hard to control, and p_2: the orientation of the clipped Autogrid with respect to the tweezers retrieving the clipped Autogrid is very hard to control.

F1-score A score that represents both the precision and recall, defined as: $F1 = 2\frac{P \cdot R}{P+R}$

FN False Negative, defined as: the algorithm detects no object at the location where the object to be detected is present.

FP False Positive, defined as: the algorithm identifies an object in the image while the object that is to be detected is not there in reality.

PT1, PT2, PT3, PT4, PT5 Numbering of the different Placement Tests in experiment 4B.

P Precision, defined as: $P = \frac{TP}{TP+FP}$

R Recall, defined as: $R = \frac{TP}{TP+FN}$

TN True Negative, the algorithm predicts that the thing it is trained to detect is not there, and this thing is not there in reality. This option is excluded for object detection within an image.

TP True Positive, defined as: a correctly identified object in an image.

Contents

1
Introduction

Observing cellular structures at the nanometer scale is of great interest in a wide range of research. Current golden standard for imaging these structures at such a small scale is Cryogenic electron microscopy (cryo-EM). Cryo-EM has been used in a wide range of research from observing cellular interactions when a cell is infected by a virus [4, 5, 9, 11, 17, 18] to characterizing the crystal morphology of single-celled marine algae [56]. Depending on the size of the structure of interest, different cryo-EM techniques are available. For imaging biological structures with a size comparable to that of a single protein structure a cryo-EM technique called single-particle analysis (SPA) can be used.

That SPA cryo-EM is a promising technique is illustrated by the fact that SPA cryo-EM was named "Method of the Year" by Nature in 2016 [49]. Shortly after, Jacques Dubochet, Joachim Frank, and Richard Henderson were awarded with a Nobel prize for developing SPA cryo-EM in 2017.

Many biological structures that are of interest are however larger than single proteins. A single cell is typically too large to be imaged using SPA cryo-EM. Therefore imaging biological structures that are larger than single proteins requires some more effort. Current state of the art for imaging whole cells in their native environment is cryogenic electron tomography (cryo-ET).

While recent developments have led to major improvements of the SPA cryo-EM workflow, the entire process from culturing the cells to obtaining a final image still is a time-consuming expensive process that is known to be prone to failure. Risk of failure is even higher for the cryo-ET workflow, which compared to the workflow for SPA contains some extra steps. From start to end, the cryo-ET workflow consists of over 22 steps of which many still comprise of manual handling of the sample.

Cellular research often requires preparing many samples. Due to the low-yield time-consuming cryo-ET workflow, researchers spend a large amount of time on acquiring a single image. Moreover, the manual handling steps preceding final imaging require practice. Scientists interested in using this technique for their research therefore often spend a significant period of their time on practicing the manual handling steps that are still present in the current workflow. Together with the high costs involved in setting up a cryo-ET facility, this is the main reason that cryo-ET is only available to a select group of researchers.

In February 2020, researchers were able to identify the structure of the SARS-CoV-2 spike protein and its cellular receptor during infection using SPA cryo-EM. This was considered a major step forward for research trying to target the virus for medicinal purposes. In September that year Wolff et al. [59] used cryo-ET to identify a molecular pore on the SARS-CoV-2 membrane that could be a potential drug target. The only reason they were capable of identifying this structure relatively soon, is that the research was initiated some time before the pandemic started. Decreasing the time required for cryo-ET and making this technique available to more than only a select group of researchers, could have a major impact on research targeting such viruses for medicinal purposes.

Automation of the manual steps involved in the cryo-ET workflow could be a solution to increase the yield, decrease the time required for practicing manual handling steps, and increase the speed of acquiring images in general. Automation of the cryo-ET workflow can thereby enable the fast generation of large quantitative data sets. Needless to say, these large quantitative data sets will be of great scientific value for many research areas.

One of the manual steps that could be improved by automation is a step called: "Clipping of the Autogrid". This step could be regarded as one of the missing links for full automation of the cryo-ET workflow. Moreover, it is a step that requires practice and is known to be prone to failure [13]. Automation of this specific step in the cryo-ET workflow could therefore improve the yield and reduce the learning time required for the current workflow.

Clipping of the Autogrid
Clipping of the Autogrid is the process where an Autogrid is assembled from the three components shown on the left in Figure 1.1. The component in the middle is a TEM-grid which is used as a sample carrier for the sample to be imaged. The TEM-grid is inserted in an Autogrid cartridge (bottom-left component) to enable automatic handling by increasing the stiffness of the structure. A retaining ring referred to as c-clip (top-left component) is inserted at the top of the Autogrid cartridge to ensure the TEM-grid doesn't fall out. The clipped Autogrid is shown on the right in Figure 1.1. A more elaborate description of the different steps and tools involved in clipping the Autogrid is provided in 2.2.

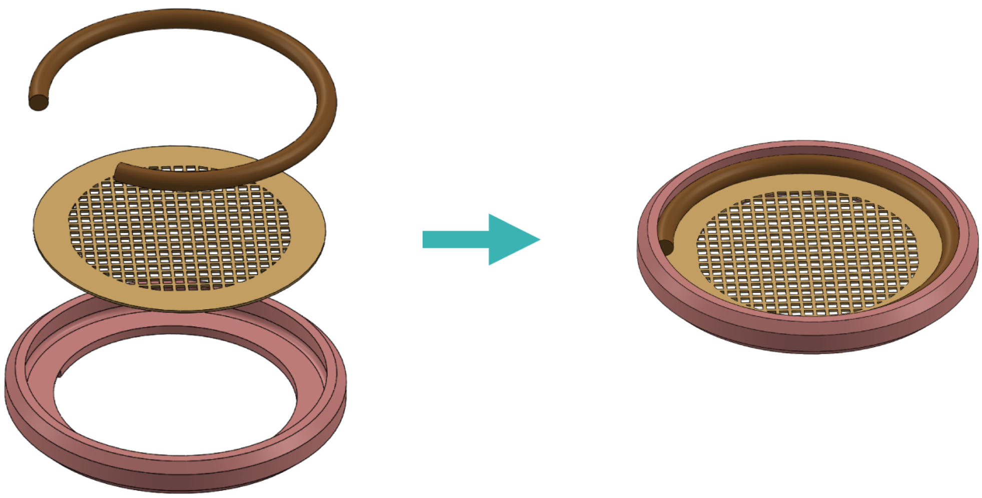

Figure 1.1: Clipping of the Autogrid is the assembly of an Autogrid from three components. The three components on the left from top to bottom are: C-clip, TEM-grid, Autogrid cartridge. On the right is the assembled Autogrid.

Aim of thesis
As automation of clipping of the Autogrid can improve the yield of the cryo-ET workflow, reduce time spend on practicing manual handling steps, and increase the speed of data collection, the aim of this thesis is to improve and automate the current clipping of the Autogrid. If successful this can be considered as a major step towards full automation of the cryo-ET workflow.

Structure report
To provide more background information on why cryo-ET is the current golden standard for imaging cells in their native environment, the first chapter of this report consists of background information (Chapter 2). Also, an elaborate description of clipping the Autogrid and some of the other sample preparation steps required for cryo-ET will be given (Section 2.2).

To achieve the final aim of automating the clipping procedure and increasing the yield of the cryo-ET workflow, the potential sources of damage in the current clipping procedure have to be identified. There could be certain aspects of the current clipping procedure that will induce damage on the TEM-grids even if they would be performed automatically by a machine. Therefore in the subsequent chapter, a problem analysis is described identifying potential sources of damage during clipping (Chapter 3).

Subsequently, designed solutions for automation and preliminary test results are presented for all steps in the clipping procedure (Chapter 4). After describing the proposed solutions for the clipping steps, methods for experimental testing are given.

In Chapter 5, the experimental results for all described experiments (experiment 1, 2A, 2B, 3, 4A, and 4B) are presented. The last two chapters consist of a discussion on the design choices and experimental results (Chapter 6), and a conclusion (Chapter 7).

2
Background

2.1. Cryo-ET as the current golden standard

Being able to observe structures at a small scale can help researchers understand a variety of processes that would otherwise have remained a mystery. Recent developments have enabled researchers in the medical and biological field to observe cellular interactions at near-atomic resolution. When observing structures at such a small scale, the wavelength of the light is the limiting factor for going for a smaller scale. When imaging at a scale beyond the optical resolution, electron microscopes are used where electrons are fired at the samples that are to be imaged. Thereafter a variety of things can be measured from the sample such as: backscattered electrons, secondary electrons, x-rays, cathodoluminescence, and transmitted electrons if the sample is thin enough [21]. Due to the smaller wavelength of electrons, with electron microscopy (EM) a much higher resolution can be obtained than is currently possible by using light microscopy.

To avoid energy loss of electrons due to collisions with molecules in the air, electron microscopes have to operate in vacuum. In general, biological tissues however contain a relatively large amount of water. When placing such tissue in a vacuum environment, this would quickly induce vacuum evaporation, which is very undesirable. Traditionally, samples are therefore dehydrated and chemically fixed before being imaged using EM. Such sample preparation methods are however know to cause deformation and deterioration of the biological tissue that is of interest [10, 35, 45]. Moreover, chemical fixation is associated with a certain amount of time delay before fully fixating the sample. When trying to capture the exact moment a virus enters a cell for medical purposes, such time delay is best prevented.

For reasons mentioned above, there is currently a gradual shift in life sciences from chemically fixating samples towards a relatively new technique where the sample is fixed with cryofixation. With cryofixation, a sample is rapidly frozen to capture a specific cellular event. This technique is not only faster, but it also allows for retaining the native cellular structure that is studied [45].

When freezing the sample, the formation of ice crystals should be prevented, as ice crystals could distort the structure of the sample. Therefore multiple methods (described in Subsection 2.2.1) have been used to rapidly freeze samples. The high cooling rates that can be reached using these methods induce the formation of so-called vitreous (glass-like) ice.

After the sample is frozen, it can be imaged using an electron microscope dedicated to be used for frozen samples. Often, a special sample stage is used that keeps the sample cold. If the temperature in the sample would increase, this would cause devitrification of the ice. The highest resolution electron microscopes are those where the electrons go through the sample. Such a Transmission Electron Microscope (TEM) can however only be used if the samples are sufficiently thin. If the biological structures are thin enough, single-particle analysis (SPA) can be used to image the sample. With this technique, a biological macromolecule is dissolved in an aqueous substance. Then, the different orientations of the macromolecule that are present in the solution can be used to reconstruct a 3D image. Many cellular structures and events are however to large to be imaged using this technique. Current golden standard for imaging such structures and events at a small scale is therefore cryogenic electron tomography (cryo-ET). With this technique, a sample is thinned to obtain the required thickness to be imaged in a TEM. Thereafter, to obtain a 3D image, a stage inside the TEM is tilted in different angles while firing the electrons through. An illustration of SPA and cryo-ET is given in Figure 2.1.

In the next section some of the sample preparation steps involved in the cryo-ET workflow are given to provide a broader overview of the different processes associated to cryo-ET.

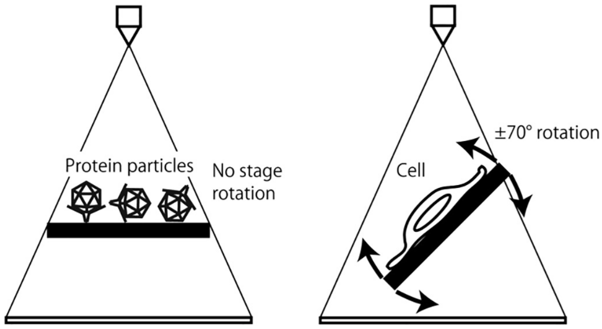

Figure 2.1: Schematic illustration of SPA (left) and cryo-ET (right) which requires additional tilting of the stage on which the sample is imaged, figure adapted from Murata et al., 2018 [36]

2.2. Workflow steps involved in cryo-ET

Although the entire cryo-ET workflow consists of over 22 steps, the workflow can be summarised as the four main steps shown in Figure 2.2: vitrification by plunge freezing (m_1), cryogenic light microscopy (cryo-LM, m_2), cryogenic focused ion beam (cryo-FIB) milling (m_3), and imaging in the cryo-TEM (m_4).

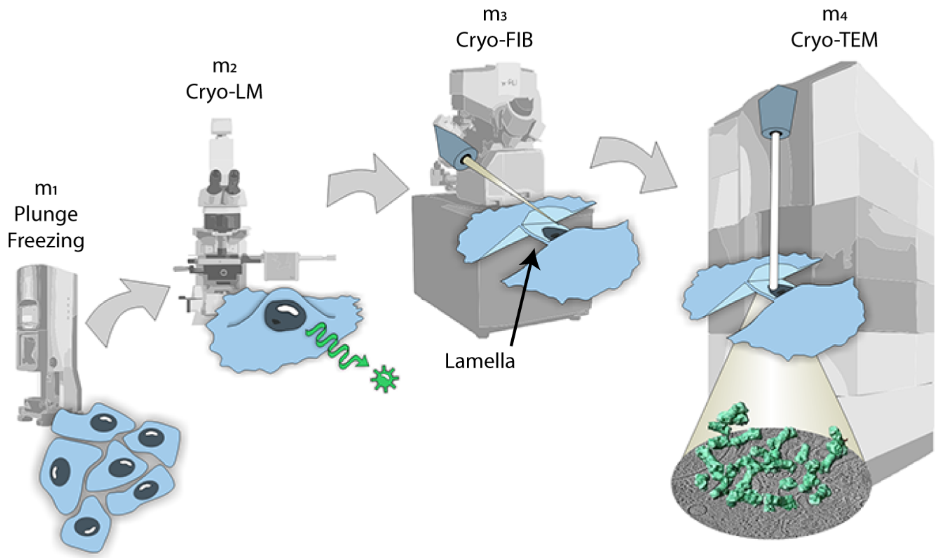

Figure 2.2: The four main steps in the cryo-ET workflow: m_1 plunge freezing, m_2 cryo-LM, m_3 cryo-FIB, m_4 cryo-TEM, figure adapted from Rigort et al., 2018 [44]

2.2.1. Vitrification

In the first main step (m_1) the sample is vitrified using plunge freezing. Plunge freezing relies on high cooling rates to cause the formation of vitreous ice [3]. To reach these high cooling rates, the sample is rapidly plunged into a cryogen (liquid ethane or liquid propane). Using this approach, samples up to 10 µm can be vitrified [39, 40]. Although other cryofixation techniques exist, plunge freezing is the technique that is currently used most. Other available techniques are for example Jet freezing [8, 42, 60], high-pressure freezing [1, 7, 28–31, 40, 55, 57], and slam freezing [2, 22, 23]. These techniques were described in more detail in my literature report [54] and will not be explained further in this report.

2.2.2. Cryogenic light microscopy

In the second main step in the cryo-ET workflow (m_2), light microscopy and specifically fluorescence light microscopy (FM) is used to localize areas of interest for electron microscopy. Where cryo-ET is capable of generating static 3D images at nanometer resolution, FM can be used to capture the dynamic processes in cells thereby providing information on the functional state of the tissue [58, 61]. Correlating light and electron microscopy is also referred to as (cryo-)correlative light and electron microscopy (cryo-CLEM). Sometimes an extra step using light microscopy is used after FIB-milling to verify that the region of interest is retained [16].

2.2.3. Cryogenic focused ion beam milling

For electrons to pass through the sample, samples have to be very thin. Ideally the thickness of a sample is below 300 nm [40]. As many biological cells do not meet these requirements [43], these samples are thinned using a variety of techniques. In the third main step (m_3) for cryo-ET, cellular samples are thinned using Focused Ion Beam (FIB) milling. With FIB milling, beams of heavy ions (typically Ga^+) are fired at the sample creating a thinned section on the sample. An illustration of this so-called lamella is given in Figure 2.2.

Other techniques are available for thinning cellular tissue such as cryo-ultramicrotomy where samples are cut with a diamond knife. A more elaborate explanation of different sectioning techniques was provided earlier in my literature survey [54].

2.2.4. Cryogenic transmission electron microscopy

After the samples are sufficiently thinned using cryo-FIB milling, they are imaged in a cryo-TEM (m_4). A stage with the sample on it is tilted in different angles in an electron beam and subtomogram averaging is used to obtain a 3D image. Current methods for cryo-TEM allow for automatic imaging of up to 12 samples.

Sample carrier

To image samples in a TEM they have to be supported by an electron transparent sample carrier, the so-called TEM-grid. A TEM-grid consists of a round grid-like structure that is there to support a very thin electron transparent layer.

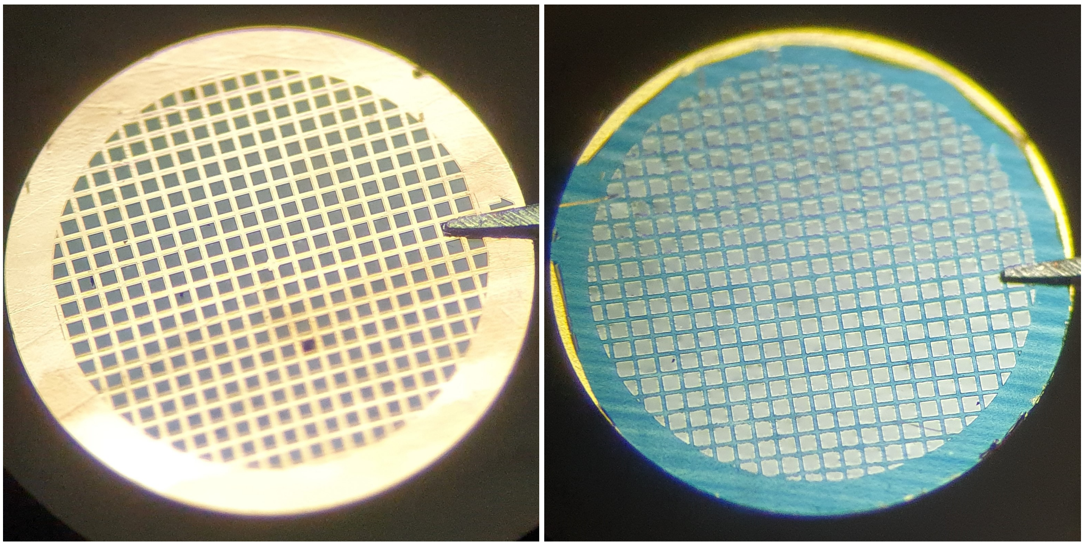

Figure 2.3: The top (left) and bottom side (right) of a golden TEM-grid. At the top, golden grid bars are clearly visible. At the bottom side the thin coating is visible that appears to be a slightly blue due to the lighting conditions.

Figure 2.3 shows the top and bottom side of a TEM-grid. The grid-like structure is available in a variety of materials such as copper, nickel, gold, aluminum, molybdenum, titanium and stainless steel [50]. For cryo-ET, cells are cultured on golden grids because the other materials are toxic to cells. TEM-grids have an outer diameter of 3 - 3.05 mm and a thickness of 25 µm [50]. The thickness of the grid bars and the spacing of the grid holes depend on the specific application the TEM-grid is used for.

The grid is coated with a 10-12 nm thick electron transparent layer. This thin layer is usually made of carbon although sometimes coating layers made out of Silicon dioxide or gold are used, depending on the application. This carbon layer can have holes with different shapes and sizes of which a few examples are shown in Figure 2.4.

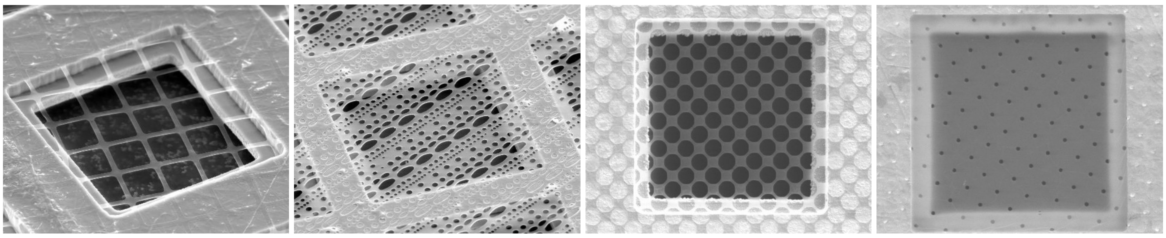

Figure 2.4: Four images of different sizes of holes in the thin carbon that is supported by the grid bars of an TEM-grid, images obtained from Quantifoil [41].

These fragile TEM-grids are damaged easily throughout the cryo-ET workflow. At locations where the carbon layer is damaged, the sample cannot be imaged and the TEM-grid lost it's use. If this happens to be the region of interest on the TEM-grid, the entire cryo-ET workflow has to start over. In the next subsection handling steps that are required before and in between the four main steps will be described.

2.2.5. Other steps in the cryo-ET workflow

In between the four main steps described before (m_1, m_2, m_3, and m_4), more handling steps are necessary to complete the cryo-ET workflow. Before plunge freezing, cells are cultured on a golden TEM-grid in a petri dish. When culturing the cells, the TEM-grid has to be in a horizontal position. This is illustrated in Figure 2.5a. The horizontal orientation makes it hard to retrieve the TEM-grids from the petri dish. Subsequently, during plunge freezing the orientation of the TEM-grid should be perpendicular (illustrated in Figure 2.5b) to the cryogen the grid is plunged in to avoid damage. After the TEM-grid with sample is plunge frozen, every time the TEM-grid is transferred, this should be done while avoiding devitrification. The TEM-grid is manually transferred between plunge freezing device, cryo-LM, cryo-FIB apparatus, and cryo-TEM, using dedicated tools. To simplify handling of the fragile TEM-grid, the TEM-grid is clipped in an Autogrid cartridge (clipping the Autogrid). An elaborate explanation on the clipping procedure will be provided in the next subsection.

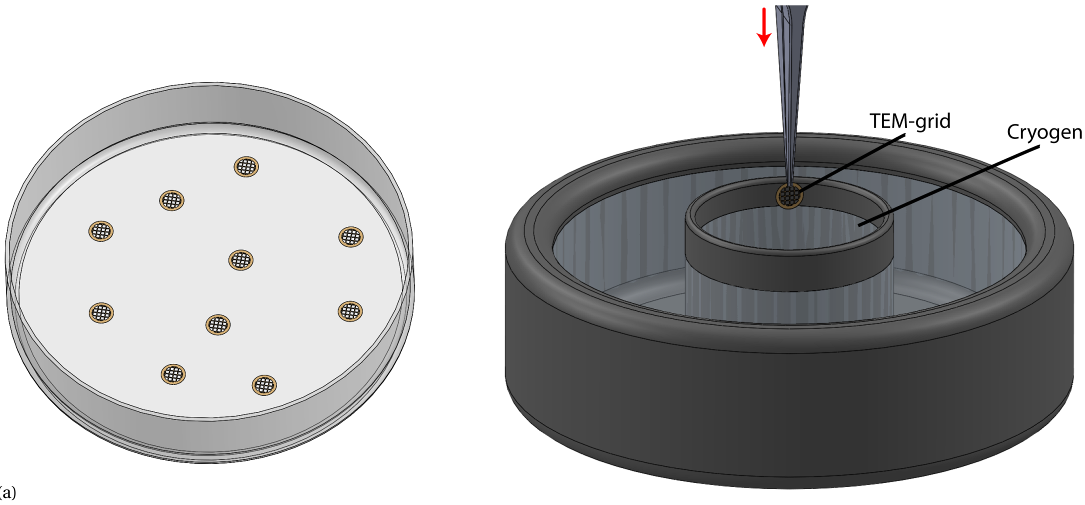

(a)

(b)

Figure 2.5: (a) Illustration of TEM-grid in a petri dish. (b) Illustration of plunge freezing.

2.2.6. Clipping of the Autogrid

Clipping the Autogrid is done after the sample is plunge frozen. The thermal mass of an Autogrid is higher than that of a TEM-grid. If the Autogrid would be clipped before plunge freezing, this could result in a cooling rate too low for vitrification of the sample [6]. Figure 2.6 shows an illustration of the four steps (c_1, c_2, c_3, c_4)

involved in clipping the Autogrid.

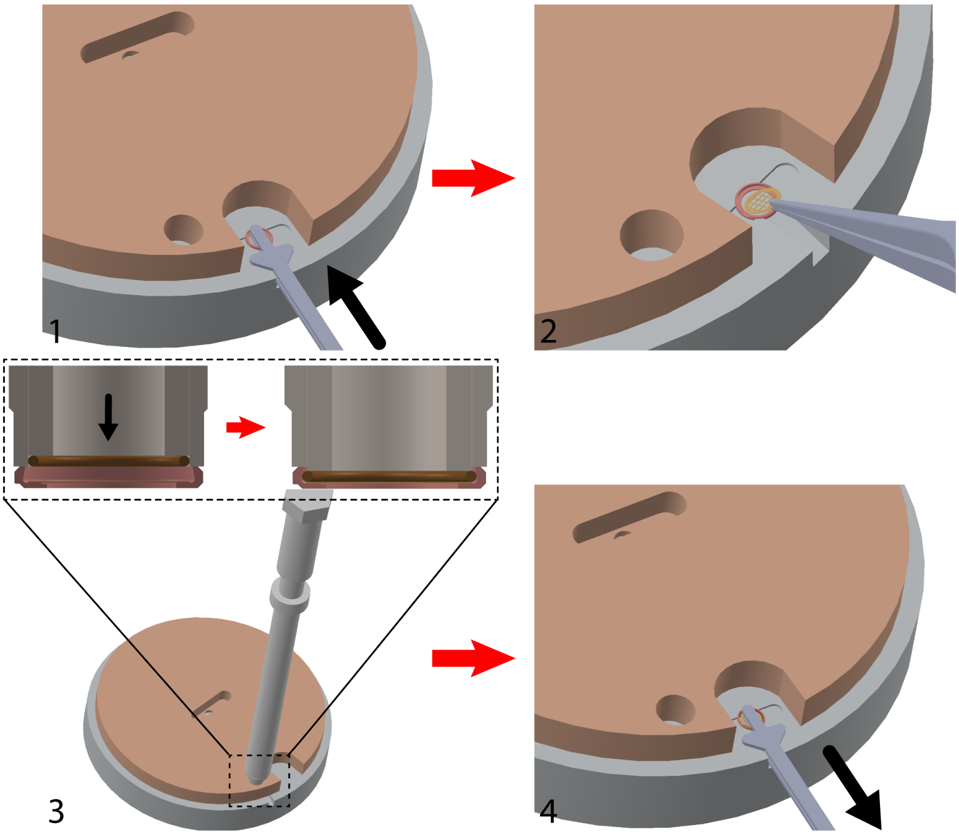

Figure 2.6: Illustration of the four steps (c_1, c_2, c_3, c_4) involved in clipping the Autogrid: c_1 Autogrid cartridge placement, c_2 TEM-grid placement, c_3 c-clip insertion, and c_4 retrieval of the clipped Autogrid.

In the first step (c_1), an Autogrid cartridge is inserted in the clipping station using a pair of Autogrid tweezers. This clipping station is designed with the sole purpose of enabling clipping of the Autogrid. The clipping station is surrounded by liquid nitrogen, and the Autogrid cartridge itself is covered in liquid nitrogen vapour, to avoid devitrification of the sample. The liquid nitrogen vapour also prevents contamination of the sample. Contamination is the process where water molecules present in the air surrounding the tissue stick to the sample and freeze. These water molecules from the surrounding air form crystalline ice, thereby reducing the quality of the images that can be obtained. In the second clipping step (c_2), a frozen TEM-grid (with frozen sample on it) is placed in the Autogrid cartridge. In the third clipping step, a pen-like tool is used to insert a c-clip in the Autogrid cartridge (clipping pen). This c-clip is used to retain the TEM-grid inside the Autogrid cartridge. The c-clip is inserted in the cylindrical bottom part of the clipping pen. Due to the pretension in the c-clip it remains in the clipping pen. Then, the clipping pen is cooled in liquid nitrogen vapour to ensure it doesn't induce devitrification of the sample. The top part of the clipping station is rotated to align an alignment hole with the Autogrid cartridge. Thereafter, the pen is used to press the c-clip down in the Autogrid cartridge. The pretension in the c-clip and the slight angle of the inside wall of the Autogrid cartridge cause the c-clip to stay at the position it is pressed in by the clipping pen. After the Autogrid is assembled, the Autogrid is retrieved from the clipping station in the fourth clipping step (c_4).

2.2.7. Missing link for the automation of the cryo-ET workflow

The clipped Autogrid has an increased stiffness which reduces the chances of damaging the fragile TEM-grid. This allows for automatic handling of up to 12 samples in the cryo-TEM (step m_4). Moreover, recently Gorelick et al. [16] were the first to integrate a cryo-LM into a FIB-SEM. Shortly after in October 2020, the first commercially available cryo-LM was launched that can be integrated with already existing cryo-FIB-SEM's [25]. Although this is not yet widely used in the cryo-ET workflow, this will in the near future merge the second (m_2) and third (m_3) main step of the cryo-ET workflow into one step. This reduces the amount of manual transfer steps that are required throughout the cryo-ET workflow.

These recent developments have reduced the chances of contaminating or damaging TEM-grids after clipping. Providing an automated solution for clipping the Autogrid, can therefore be the connecting link between plunge freezing and workflow steps following the clipping procedure. This can increase the yield of the cryo-ET workflow. Moreover, it will reduce the time required for practicing handling of fragile TEM-grids.

3
Problem analysis

3.1. Hypotheses on the potential causes of damaging TEM-grids during clipping

Before automating the clipping procedure, potential sources of damage have to be identified in the current clipping procedure. In this chapter, the feasibility of the potential sources of damage on TEM-grids that were identified in a previous literature survey [54], are investigated further using FE analyses and analytical calculations. The following hypotheses concerning the possible failure mechanisms of the current clipping procedure [54] are investigated in this chapter:

1. Improper handling of the TEM-grid while placing it in the Autogrid cartridge might damage the TEM-grid (h_1).
2. A volume (e.g. air or liquid nitrogen) is trapped between the current c-clip insertion tool and the thin carbon layer on the TEM-grid in the third clipping step (c_3) causing the carbon layer to rupture.
3. In the current clipping pen, there is a rigid connection between the thumb and the cylinder pushing the c-clip down. The rigid connection between the thumb and tip of the current clipping tool enables the possibility of applying to much force on the c-clip and via the c-clip also on the TEM-grid (h_3).
4. The uncontrolled downwards movement of the c-clip that is dominated by friction might cause stress concentrations in the TEM-grid upon contact (h_4).

In the last section of this chapter (Section 3.5), two other problems in the current clipping procedure will be described which are not related to damaging TEM-grids.

3.2. Hypothesis h_1: improper handling

Experienced users are capable of preparing less-damaged TEM-grids. Therefore the hypothesis that improper handling of TEM-grids is one of the main sources of failure during the clipping procedure is likely to be true. Although automating such a delicate procedure might prove to be difficult, automation has the potential to be able to reduce damage on TEM-grids or prepare TEM-grids without any damage. Designs used for automatic handling of TEM-grids, and methods for experimental validation of these designs are given in: chapter 4

3.3. Hypothesis h_2: Increased pressure as potential source of damage for TEM-grids

3.3.1. Observations of the current clipping tool.

When using the current clipping pen to assemble the Autogrid, the movement of the cylindrical structure in the pen-like tool can potentially cause an increase in pressure on the top side of the TEM-grid. For the analysis in this section, the volume above the TEM-grid is assumed to be filled with air. In reality, there might also be other mediums present (e.g. liquid nitrogen, or liquid nitrogen vapour). The current tool has a hole through the center that is (probably) there to allow air to travel through the center of the cylinder. This hole is connected to the side of the clipping pen, which is in contact with the air surrounding the clipping pen (indicated with the black arrow in Figure 3.1). When pressing the c-clip down, this hole is closed. Closing this hole might cause air to be trapped between the cylindrical part of the clipping pen pushing the c-clip down, and the fragile carbon layer on top of the TEM-grid.

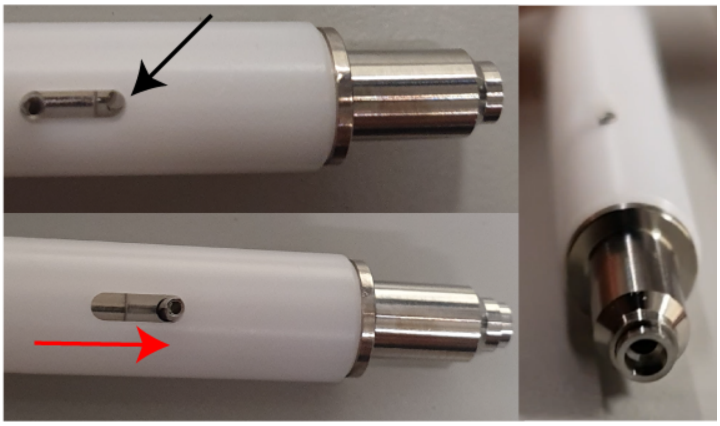

Figure 3.1: Figure showing how the hole through the old clipping pen is closed off when pressing the c-clip down. The left side of the image shows the clipping pen when it is pressed (bottom left) and when it is not pressed (top left). The right side of the image shows the bottom side of the tool when it is pressed, showing the hole that goes through the center. The black arrow indicates the hole that is closed off when the c-clip is inserted. The red arrow indicates the direction of movement of the cylindrical part on the inside of the tool.

Figure 3.2 is an illustration of the effect the increased air pressure might have on the carbon layer on the TEM-grid.

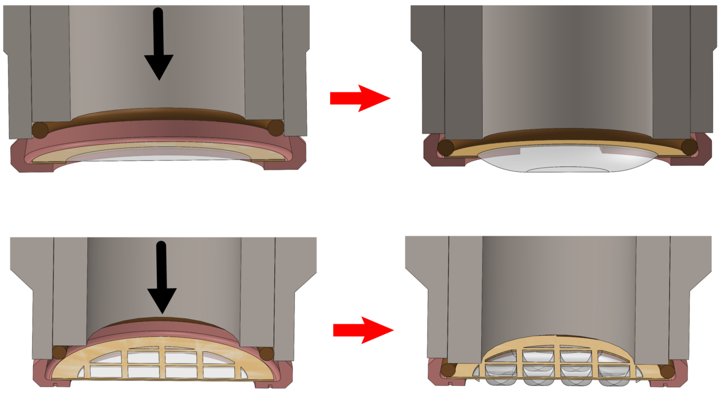

Figure 3.2: Illustration of the effect the increased air pressure might have on the carbon layer on the TEM-grid.

FE analyses were used to investigate the effect of closing the hole on the side of the clipping pen during c-clip insertion. The results of these analyses are described in the subsection below.

3.3.2. Finite element analyses

A multiscale modelling approach was used to investigate the effect of the increasing air pressure at the tip of the current clipping pen. First, the increase in air pressure near the TEM-grid when inserting the c-clip with the current clipping pen (model 1 old clipping pen: M1) was modelled. Then for comparison, the old clipping pen was modelled when the hole on the side would directly be in contact with the surrounding air (model 1 C: M1C). In the second model, one of the holes of a 200 mesh grid with holey carbon was modelled (model 2: M2). The air pressure obtained from the first model (M1) was used as input in model M2. All FE analyses were performed using COMSOL multiphysics 5.5.

Methods for FE analyses

Figure 3.3a shows the model of the old clipping pen. The blue selected structure represents the inner cylinder in the pen that is used to press the c-clip down. This inner cylinder was modelled using the multibody dynamics module in COMSOL. The situation is modelled were the hole on the side of the inner cylinder is closed and the inner cylinder moves into the Autogrid cartridge to press the c-clip down. This hole is indicated in Figure 3.3a with the red arrow, and in Figure 3.1 with the black arrow. A displacement of 0.02 mm is prescribed on the inner cylinder. This displacement causes the inner cylinder to move into the small cylindrical block labeled as: "air near TEM-grid". The air surrounding the pen was modelled as a fluid with laminar flow. A fluid structure interaction was modelled allowing for velocity transmission from the moving inner cylinder to the fluid. The outside of the clipping pen was modelled as a wall in the fluid domain. Between the outer part and the inner moving cylinder, a difference of 0.2 mm between the diameters was assumed to allow for the two parts to slide through each other. Material properties available in COMSOL multiphysics 5.5 for air and steel (AISI 316) were used to model the fluid and inner cylinder, respectively.

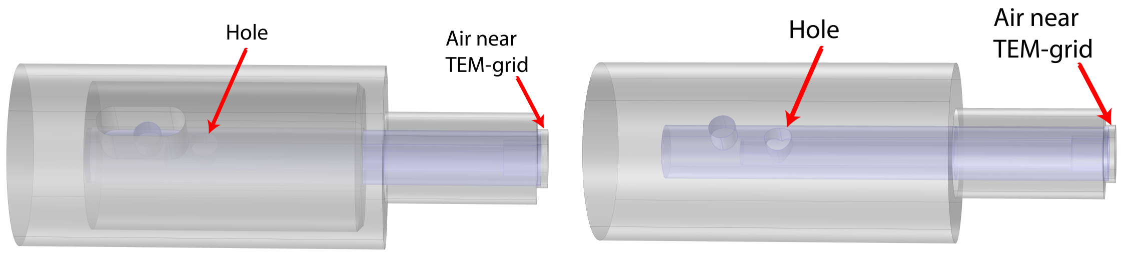

(a) (b)

Figure 3.3: The geometry used in (a) model M1, and (b) model M1C.

A time dependent analysis was performed in which the prescribed displacement was applied in two time steps of 0.005 seconds. This corresponds to a velocity of 2 mm/s for the inner cylinder. A pressure point constraint was used where a point far from the air volume near the TEM-grid was selected to have a pressure of 0 Pa. The average pressure over the surface on the right side of the air volume "air near TEM-grid" in Figure 3.3a was calculated and reported.

Then, the situation where the hole on the side of the inner cylinder would not be closed upon c-clip insertion was modelled (M1C). Here, the same modelling approach was used as for model M1 with only one difference: the outer part of the old clipping pen was removed to ensure the hole on the side was in direct contact with the surrounding air.

Based on the results from M1 and M1C, a realistic estimate of the increasing air pressure near the TEM-grid (during c-clip insertion) was used as boundary condition in the model M2. In model M2, the carbon layer covering one single grid hole on a TEM-grid was modelled. For this purpose, the dimensions of a grid hole of a 200 mesh TEM-grid were used. Commonly used dimensions for TEM-grids are given in Table 3.1.

Table 3.1: The dimensions of different commercially available TEM-grids, from Tedpella inc. [50], EOA = Extra Open Area.

Mesh	Hole (µm)	Bar (µm)
50	425	83
75	284	55
100	204	50
150	125	44
200	90	37
200 EOA	106	21
300	54	31
400	38	26
400 EOA	45	19
500	28	23

To model the carbon layer, shell elements with a thickness of 12 nm were used. Three sides of the shell structure were constraint in the z-direction (see coordinate system in Figure 3.5a). One side was constraint in all three directions (x, y, and z), and rotations were free on all sides. A geometrically nonlinear solid mechanics analysis was performed using the before-mentioned boundary conditions. A linear elastic material model was used. Different studies have been performed aimed at estimating the mechanical properties of carbon films [24, 26, 27, 37]. The mechanical properties of carbon largely depend on the atomic structure of the carbon atoms. If structured in one specific manner carbon atoms can form diamond which is known for it's high strength. At the time of writing there were no studies known to the author that estimated the mechanical properties of the carbon layer that is often used on TEM-grids. Values from different studies on the mechanical properties of carbon are reported in Table 3.2. For this analysis, the highest Young's modulus was used (500 GPa). The mean and maximum von Mises stress over the hole shell structure were calculated and reported.

Table 3.2: Different material properties of amorphous carbon found in literature.

Material	Density (ρ)	Poisson's ratio (ν)	Young's modulus (E)
Carbon	2100 $\frac{kg}{m^3}$ [24, 27]	0.2 [27]	4.1 GPa [27] 62 GPa [26] 500 GPa [37]*

* Calculated from the Bulk modulus (K) using the relation: $E = 3K(1-2\nu)$[12] . Here, ν is the Poisson's ratio.

Results from the multiscale FE analyses

Figure 3.4a shows pressure distribution after displacing the inner cylinder with 0.02 mm for model M1. Figure 3.4b shows pressure distribution after displacing the inner cylinder with 0.02 mm for model M1C.

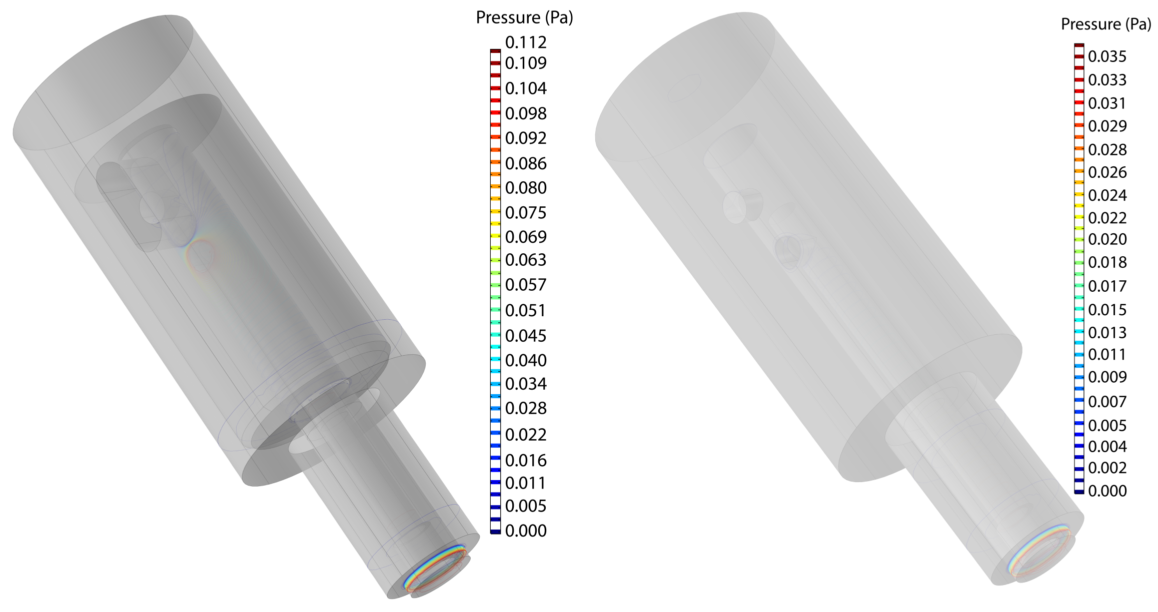

(a) (b)

Figure 3.4: (a) The pressure distribution after displacing the inner cylinder with 0.02 mm for model M1. (b) The pressure distribution after displacing the inner cylinder with 0.02 mm for model M1C.

The mean pressure (see "Methods for multiscale modelling" above) increase caused by displacing the inner cylinder was 0.11 Pa and 0.03 Pa, for M1 and M1C, respectively. Therefore, a face load ramping from 0 to 1 Pa was used as boundary condition on the holey carbon layer. Figure 3.5b shows the obtained mean and maximum von Mises stress in the carbon layer. At a pressure of 0.10 Pa, the mean and maximum von Mises stress in the carbon layer were 0.3 MPa and 4 MPa, respectively. At a pressure of 1 Pa, the mean and maximum von Mises stress in the carbon layer were 1.5 MPa and 24 MPa, respectively. Figure 3.5a shows the von Mises stress distribution in the holey carbon layer when a pressure of 1 Pa is applied.

Discussion on the multiscale FE analyses

The aim of these multiscale FE analyses was to investigate if the increase in air pressure at the TEM-grid when inserting the c-clip with the current clipping pen could be a source of damage during clipping. At the

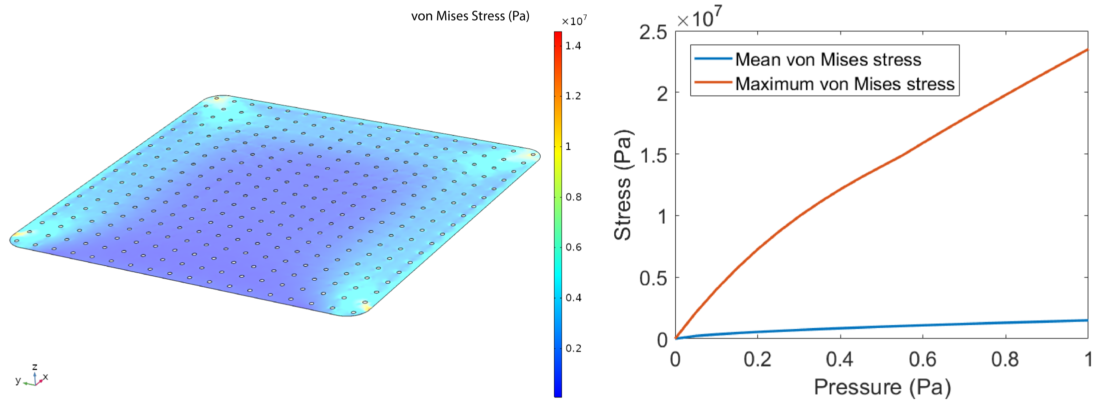

(a) (b)

Figure 3.5: (a) The von Mises stress distribution in the holey carbon layer when a pressure of 1 Pa is applied. (b) The obtained mean and maximum von Mises stress in the carbon layer

obtained increase in pressure of approximately 0.1 Pa, the von Mises stress in the holey carbon layer does not exceed the yield strength of amorphous carbon, which can be around 76 MPa [27]. In the current modelling approach a difference between the inner moving part and the outer part of the old clipping pen of 0.2 mm was assumed. In reality this difference will be a lot smaller. When observing the current clipping pen (Figure 3.2) the difference between these two parts is more likely to be one order of magnitude smaller (approximately 0.02 mm). Such tolerances are easily reached with standard fittings (e.g. $h7 : {}^{+0.000}_{-0.010}$ with $E7 : {}^{+0.024}_{+0.014}$, where the maximum difference in diameter would be 0.034). In reality the increase in air pressure caused by c-clip insertion is therefore likely to be larger. Modelling such a small difference in diameter would however require the use of elements that are smaller than the difference in diameter in the FE model. The computational power required for such an analysis is very large. Therefore for this project, such an analysis was not done. At an increase in pressure of 1 Pa, the maximum von Mises stress did not exceed 76 MPa. Although, with 24MPa it was in the same order of magnitude. In reality the holey carbon layer will not be perfect as it is in the model. Small imperfections in the holey carbon layer could potentially increase the stress levels at these locations to values above the yield strength value. Also, for these analyses only the stiffest value of the three values found for the Young's modulus was used. Using other Young's moduli will of course have it's effect on the stress distribution in the carbon layer, as would other aspects such as the pattern of holes in the carbon layer. One other aspect to be considered is the velocity with which the inner cylinder of the clipping pen moves. For these analyses, the inner part of the clipping pen had a velocity of 2 mm/s. Although air is a medium with a low viscosity, moving the inner part of the clipping pen with a higher velocity will have it's effect on the pressure at the air near the TEM-grid. This effect would be even greater if another medium is present in the pen. For the models described in this section, the volume near the TEM-grid was assumed to only consist of air. In reality other mediums could be present such as liquid nitrogen or liquid nitrogen vapour. This would increase the pressure caused by inserting the c-clip with the current c-clip insertion tool. Moreover, in the currently used FE models, only a small displacement of the inner cylinder was used. Using a larger displacement would most likely increase the air pressure near the TEM-grid. Lastly, the mean pressure increase in the model where the outer part of the clipping pen is removed (M1C) was approximately three times lower than the pressure increase calculated in model M1.

For all of the reasons mentioned above, designing a new c-clip insertion tool in which this increase in air pressure is reduced could potentially reduce damage of the carbon layer during clipping. In Section 4.2 a new c-clip insertion tool is proposed in which the increase in air pressure is reduced. Testing this new c-clip insertion can help with obtaining knowledge on the failure mechanisms in the current clipping procedure.

3.4. Hypotheses h_3 and h_4: Is there a force required for pressing the c-clip down?

In this section, hypotheses h_3 and h_4 are investigated. A free body diagram is used to predict if there is a certain amount of force required for pushing the c-clip down, and the amount of force required for pressing the c-clip down is estimated.

3.4.1. Free body diagram of the c-clip

If the c-clip is inserted in the circular opening of the Autogrid cartridge, there are two possible scenarios. In scenario one, the friction forces are larger than the forces pushing the c-clip down. In this case, the c-clip will remain in static equilibrium at the opening of the Autogrid cartridge. If this were to be true, hypothesis h_4 is not likely to be true. Hypothesis number h_3 is however still a likely candidate. The second possible scenario is the one where the friction forces are smaller than the forces pushing the c-clip down. In this case the c-clip will move down in the Autogrid until it reaches the TEM-grid which will then be locked into place by the c-clip. If this scenario were to be the true, both hypotheses (h_3 and h_4) can still hold true. However, a well-designed c-clip insertion tool would not exert any forces on the c-clip after releasing it at the top of the Autogrid as it would slide down on its own.

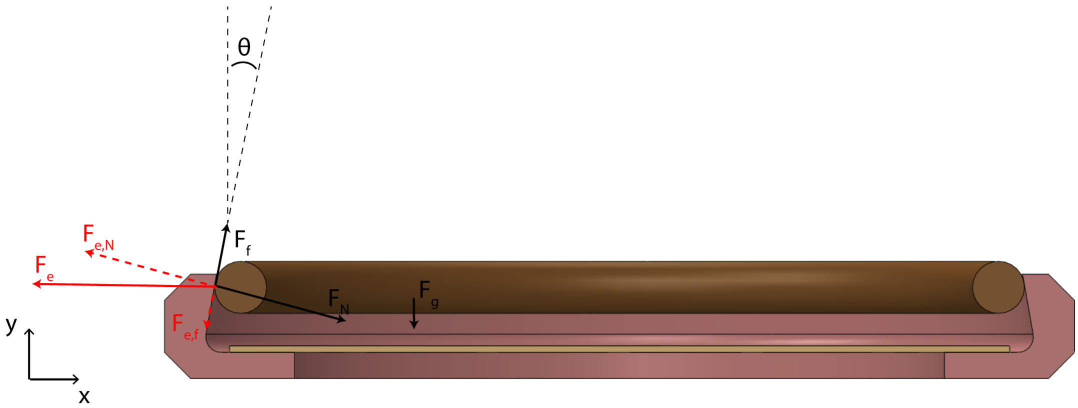

Figure 3.6: The free body diagram of the c-clip in the Autogrid cartridge. Here, F_f, F_N, F_e, F_g, and θ respectively are the friction force, normal force, the elastic force exerted by the c-clip caused by pretension, the gravitational force caused by the mass of the c-clip, and the angle between the friction force and the y-axis.

A simple free body diagram was used to estimate the forces acting on the c-clip upon insertion in the Autogrid. Figure 3.6 shows the free body diagram of the c-clip. Here, F_f, F_N, F_e, F_g, and θ respectively are the friction force, normal force, the elastic force exerted by the c-clip caused by pretension, the gravitational force caused by the mass of the c-clip, and the angle between the friction force and the y-axis.. Force F_e can be decomposed into components $F_{e,N}$ and $F_{e,f}$ which are the components of the elastic force in the normal direction and in the opposite direction of the friction force. These components can be defined as a function of the elastic force using the angle θ as defined in Figure 3.6 using:

$$F_{e,N} = cos(\theta)\, F_e \tag{3.1}$$

and:

$$F_{e,f} = sin(\theta)\, F_e \tag{3.2}$$

By assuming that the normal force is proportional to the friction force and that the amount of friction is independent of the area of contact between the c-clip and the Autogrid cartridge, the friction force (F_f) can be defined using the friction coefficient μ:

$$F_f = \mu F_N = \mu cos(\theta)\, F_e \tag{3.3}$$

For a c-clip with a round wire, the radial elastic force at 90° from the center of the gap (as indicated in Figure 3.7) can be approximated by [48]:

$$F_e = \frac{Ed^4 u}{4D^3} \tag{3.4}$$

Here, E is the Young's modulus, d is the wire diameter of the c-clip, u is the radial deflection of the c-clip at 90° (at the location of F_e in Figure 3.7), and D is the outer diameter of the c-clip. The sum of all forces in the direction normal to the surface in the contact point can then be written as:

$$\sum F_{\to N} = F_{e,N} - F_N + F_g sin(\theta) = cos(\theta)\, F_e - cos(\theta)\, F_e + F_g sin(\theta) \tag{3.5}$$

The sum of all forces in the direction of the friction forces in the contact point can then be written as:

$$\sum F_{\to f} = -F_{e,f} + F_f - F_g cos(\theta) = -sin(\theta)\, F_e + \mu cos(\theta)\, F_e - F_g cos(\theta) \tag{3.6}$$

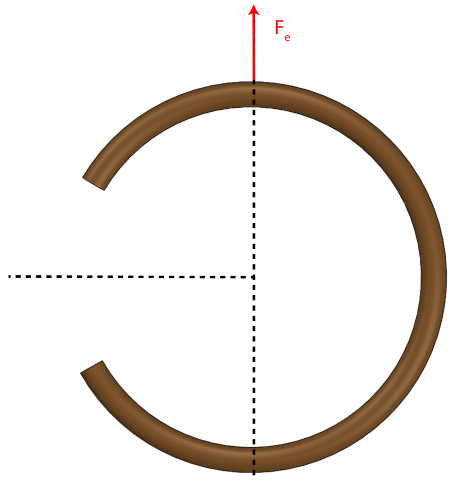

Figure 3.7: The c-clip with the elastic force F_e indicated with the red arrow.

Using the material parameters reported in Table 3.3, the gravitational force can be calculated as:

$$F_g = \rho V g \approx 2.3 \cdot 10^{-5}\text{N} \tag{3.7}$$

Using equation 3.4 with a radial deflection of 1 mm results in an elastic force of 0.6 N ($F_e = 0.6$N). The elastic force in the c-clip is therefore a few orders of magnitude larger than the gravitational force acting on the c-clip. The sum of all forces can therefore be rewritten using:

Table 3.3: Material properties of the c-clip, used properties are those of phosphor bronze [51, 52]

ρ	E	d	D	V	g	θ
8900 [51] $\frac{\text{kg}}{\text{m}^3}$	116 Gpa [52]	0.2 mm	3.1 mm + u	2.4 mm^3	9.8 $\frac{\text{m}}{\text{s}^2}$	10°

$$F_{e,f} + F_g cos(\theta) \approx F_{e,f} \tag{3.8}$$

and:

$$F_{e,N} + F_g sin(\theta) \approx F_{e,N} \tag{3.9}$$

The sums of forces in both directions are then:

$$\sum F_{\rightarrow N} = cos(\theta)\, F_e - cos(\theta)\, F_e = 0 \tag{3.10}$$

and:

$$\sum F_{\rightarrow f} = -sin(\theta)\, F_e + \mu cos(\theta)\, F_e \tag{3.11}$$

The c-clip will therefore slide down if:

$$sin(\theta) > \mu cos(\theta) \tag{3.12}$$

With $\theta = 10°$, the c-clip will slide if $\mu < 0.18$. This holds only if the assumption: $F_g << F_e$ is true. Although friction coefficients can vary between different experimental setups, friction coefficients smaller than 0.18 are usually only obtained between materials if some sort of lubrication is used.

Based on these results it is therefore likely that a certain amount of force is required for pushing the c-clip down once it exits the clipping tool and enters the Autogrid cartridge. This hypothesis is strengthened by previous observations where the c-clip was stuck at the top-side of the Autogrid without sliding down.

Equation 3.11 can be rewritten to obtain the required force (F_{req}) for pushing the c-clip down:

$$\sum F_{\rightarrow f} = -sin(\theta)\, F_e + \mu cos(\theta)\, F_e - cos(\theta)\, F_{req} \tag{3.13}$$

In this case, the required force is defined as a body force in the $-y$ direction (similar to F_g in Figure 3.6). Equation 3.13 can be rewritten to obtain the required force:

$$F_{req} > \frac{-sin(\theta)\, F_e + \mu cos(\theta)\, F_e}{cos(\theta)} \tag{3.14}$$

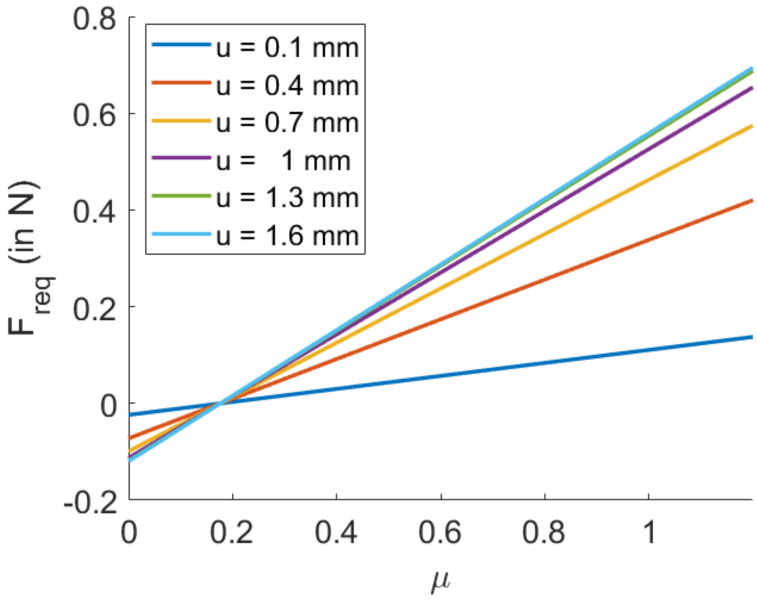

Figure 3.8: Figure showing an estimate for the force that is required for pushing the c-clip down.

Figure 3.8 shows a visualisation of the right-hand side of equation 3.14 for different values of μ and u. The previously calculated value of $\mu < 0.18$ can also be observed at the point where the required force is zero.

Based on these calculations, the magnitude of the force that is required for pushing the c-clip down will be in the range from 0 N to 1 N. These calculations suggest that it is likely that the user of the c-clip insertion tool applies too much force on the c-clip upon insertion (h_3), as only a small amount of force is required. To put this into perspective, a person playing piano exerts forces ranging from 0.6 N to 20 N on a piano key [38] where 0.6 N is the absolute minimum for holding down a key.

3.5. Problems with orientation in the current clipping procedure

Two other problems in the current clipping procedure were identified (mentioned before in the literature survey leading to this project [54]) namely: p_1) the orientation of the TEM-grid with respect to the Autogrid cartridge is very hard to control (during clipping step (c_2)), and p_2) the orientation of the clipped Autogrid with respect to the tweezers retrieving the clipped Autogrid is very hard to control (during clipping step c_4).

3.5.1. Orientation of the TEM-grid with respect to the Autogrid cartridge

That these two relative orientations are important is related to the step in the cryo-ET workflow where the sample is thinned using FIB-milling (m_2). FIB-milling is done after the Autogrid is clipped. The shallower the angle of incidence of the ions on the sample, the larger the usable area of the thin lamella that is created [34]. To allow for this shallow angle, the Autogrid cartridges have a special cutout on the bottom. Figure 3.9 shows how the ions are fired at the bottom side of the Autogrid at an angle (left). It also shows the special cut-out (right). This figure also shows the markers that are present to help identify on which side of the Autogrid the cutout is. The locations that can be reached by the FIB-beam are determined by the orientation of the TEM-grid with respect to the Autogrid cartridge. This orientation also determines the direction in which the sample is hit by the ion beam. In the current clipping procedure this orientation is very hard to control. Once the Autogrid cartridge is placed in the clipping station (c_1), it's orientation in the clipping station cannot be observed because of the lack of markers on the top-side of the Autogrid cartridge. Moreover, even if the orientation of the Autogrid cartridge in the clipping station would be known, manually placing the TEM-grid in the preferred orientation (c_2) is very difficult.

3.5.2. Orientation of the Autogrid with respect to the tweezers retrieving the Autogrid

In the last clipping step (c_4), the Autogrid is retrieved from the clipping station. Adjusting the orientation of the Autogrid with respect to the tweezers retrieving the Autogrid, is important in a later stage of the cryo-ET

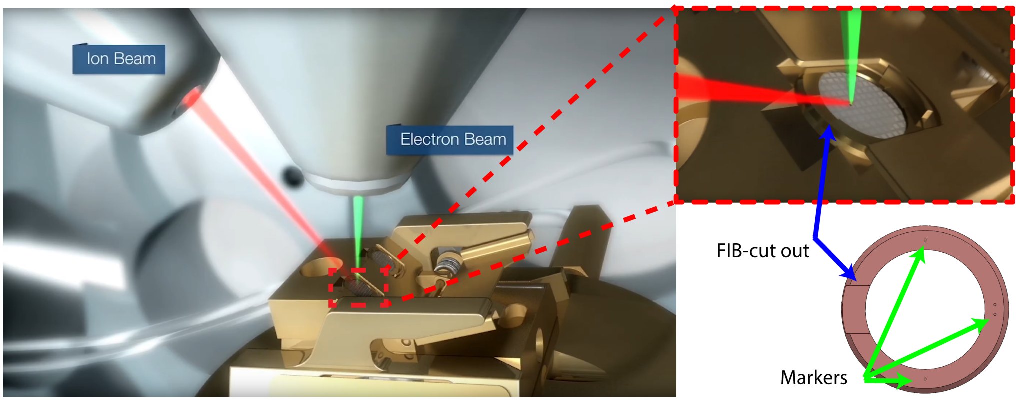

Figure 3.9: The image on the left shows how the ions are fired at the bottom side of the Autogrid at an angle, image was adapted from Fernández-Busnadiego [14], the image on the right shows the cut-out and markers on the bottom of the Autogrid cartridge.

workflow. Before the last main step in the cryo-ET workflow (m_4), the Autogrid is placed in a cassette (left image in Figure 4.1). Then, this cassette is placed in a transfer unit that can be inserted in the cryo-TEM (right image in Figure 4.1). Inside the cryo-TEM, up to 12 Autogrids are automatically retrieved and imaged. The tilting angle of the stage in the cryo-TEM (see section 2.1) should be aligned with the lamella created on the TEM-grid. As the lamella on the TEM-grid is aligned with the FIB-cutout, the tilting angle should be aligned with the FIB-cutout on the Autogrid.

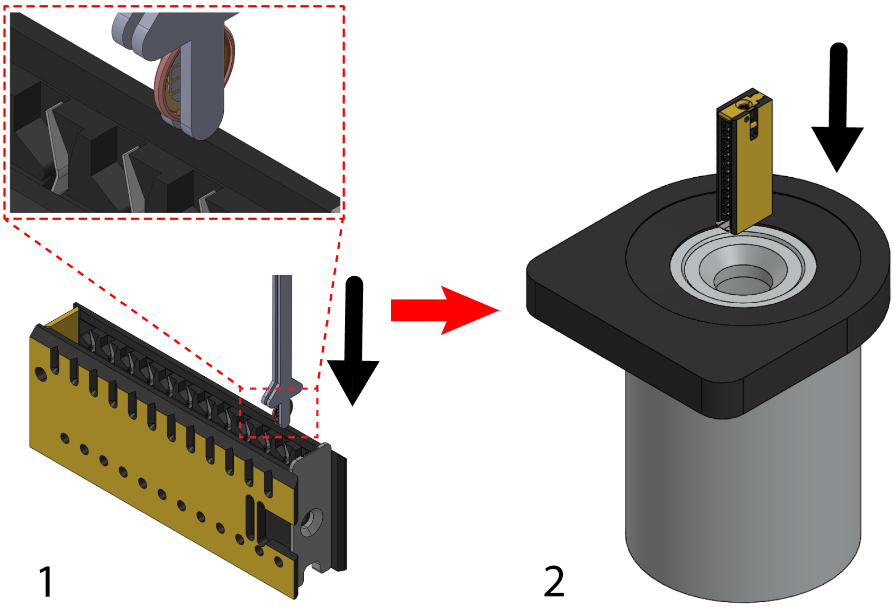

Figure 3.10: Left image: the Autogrid is placed in a cassette, right image: the cassette is placed in a transfer unit that can be inserted in the cryo-TEM

To align the tilting angle of the cryo-TEM with the FIB-cutout, the Autogrid has to be inserted in the cassette in the correct orientation shown in Figure 3.11. Adjusting the orientation of the Autogrid before the last clipping step (c_4) will enable the automatic placement of the Autogrid in the cassette after clipping. Currently, the orientation of the Autogrid with respect to the cassette is manipulated manually using a pair of tweezers, which is quite challenging. Enabling adjustment of the orientation of the Autogrid with respect to the tweezers in clipping step c_4 will therefore bring the full automation of the cryo-ET workflow one step closer.

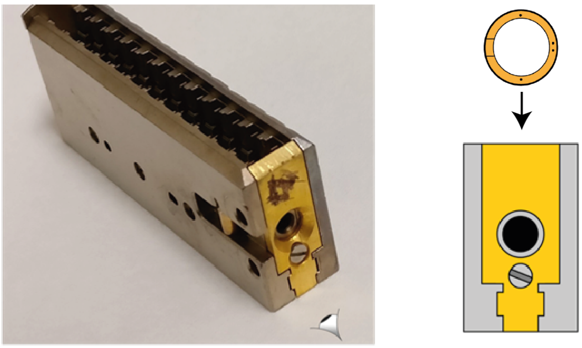

Figure 3.11: Correct orientation of the autogrid in the cassette, Figure adapted from Medeiros et al., 2018 [34]

4

Proposed designs and methods for experimental testing

4.1. Proposed new clipping procedure

A new clipping procedure is proposed to solve the two problems described in the previous section (Section 3.5). The new clipping procedure consists of six clipping steps: C_1 Autogrid cartridge placement, C_2 rotation of the Autogrid cartridge to the preferred orientation, C_3 placement of the TEM-grid, C_4 c-clip insertion, C_5 rotation of the clipped Autogrid to the preferred orientation, C_6 retrieval of the clipped Autogrid. Figure 4.1 shows the six clipping steps of the new procedure (C_1, C_2, C_3, C_4, C_5, and C_6).

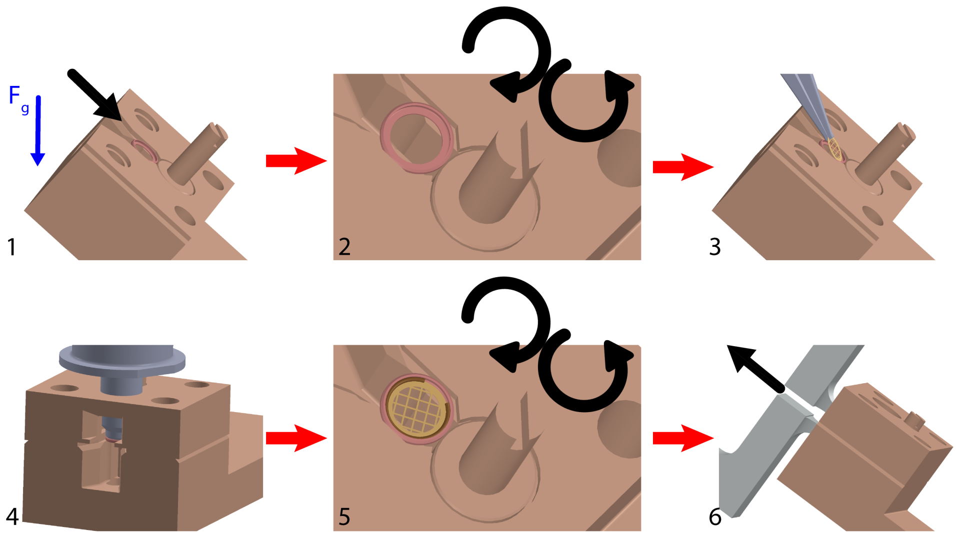

Figure 4.1: The six steps of the proposed new clipping procedure: C_1 Autogrid cartridge placement, C_2 rotation of the Autogrid cartridge to the preferred orientation, C_3 placement of the TEM-grid, C_4 c-clip insertion, C_5 rotation of the clipped Autogrid to the preferred orientation, C_6 retrieval of the clipped Autogrid. Variable F_g represents the gravitational force which is at an angle with the Autogrid holder.

This new clipping procedure consists of the four steps that were already present in the old clipping procedure (c_1, c_2, c_3, and c_4), with two extra steps (C_2 and C_5). If the orientation of the TEM-grid with respect to the tweezers or grippers placing the TEM-grid in the Autogrid cartridge in the third clipping step of the new procedure (C_3) is known, the Autogrid cartridge can be rotated to obtain the desired relative orientation of the TEM-grid (w.r.t. the Autogrid cartridge). Using this approach, the same mechanism that rotates the Autogrid cartridge in step C_2 can be used to rotate the clipped Autogrid in step C_5.

In the following sections, first, the design for a new c-clip insertion tool will be described (Section 4.2). This newly designed tool was used for testing hypotheses h_2 and h_3 (see Section 3.1) to investigate the sources of damage during clipping. Thereafter, the design for an Autogrid holder with a mechanism to rotate the Autogrid cartridge (C_2) and Autogrid (C_5) is proposed to solve the two problems (p_1 and p_2) that are described in Section 3.5 (Section 4.3). Subsequently, designs and preliminary test results for automatic handling of Autogrid cartridges, Autogrids, and TEM-grids are presented (Section 4.4 and Section 4.5). At the end of each section, methods for the experimental studies that were done for validation purposes, are given.

4.2. C-clip insertion

4.2.1. Design of manual c-clip insertion tool for testing hypotheses

Based on the problem analysis performed in the previous chapter (Chapter 3), two hypotheses on the potential sources of damage during c-clip insertion remained feasible namely: h_2 air or liquid is trapped between the current c-clip insertion tool and the thin carbon layer on the TEM-grid causing this layer to rupture, and h_3) a rigid connection between the c-clip insertion tool and the c-clip allows for applying too much force on the TEM-grid resulting in damage.

To experimentally test these hypotheses, a new manual c-clip insertion tool was designed and manufactured. Figure 4.2 shows a technical assembly drawing of the designed c-clip insertion tool.

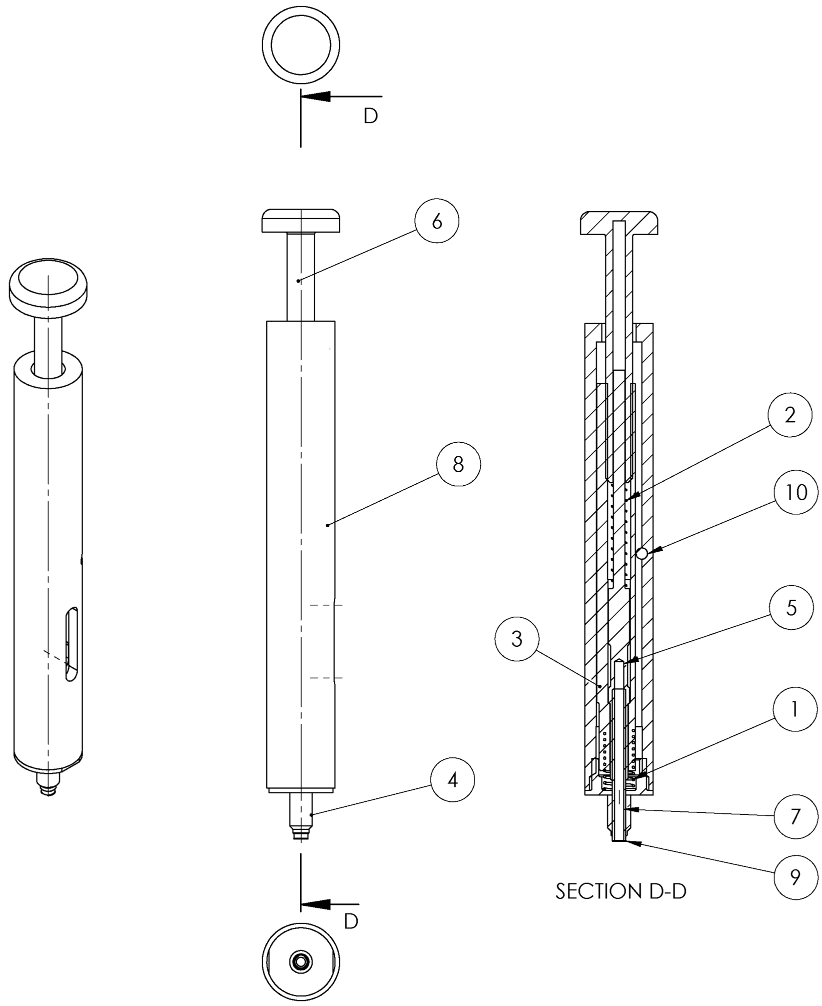

Figure 4.2: Technical drawing of the assembly of the new clipping pen. Parts are numbered to enable explaning the mechanisms in the new clipping pen.

Similar to the old clipping pen, with this new clipping pen the c-clip is pressed down into the Autogrid cartridge using a cylindrical part. To test hypothesis h_2, a hole through this cylindrical part is connected to a hole on the side of the new clipping pen. This hole ensures the air or fluid above the TEM-grid is in contact with the air surrounding the clipping pen while inserting the c-clip. The pathway of air through the new clipping pen is indicated with a dashed line in Figure 4.3.

To test hypothesis h_3 a spring mechanism is included in the new clipping pen that limits the force that can be applied on the c-clip. All parts of the new clipping pen are described below to explain the force-limiting mechanism and to explain how the hole through the center of the pen remains in contact with the hole through the side. The numbering of the parts is given in Figure 4.2. Figure 4.4 shows a 3D representation of all the parts wherein some of the holes in the parts are marked and labeled (H_1 - H_6).

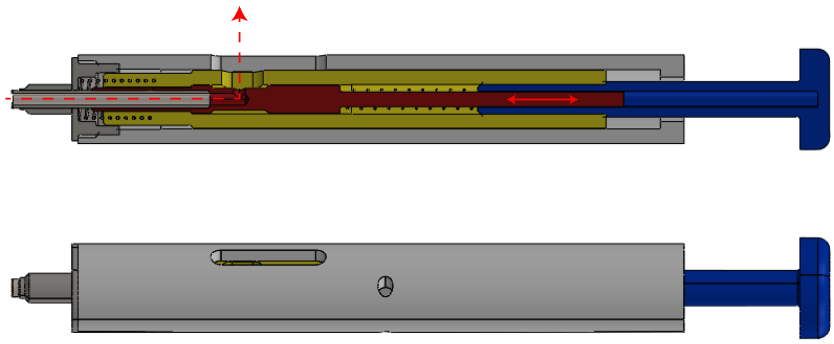

Figure 4.3: Image of a cross-section of the 3D CAD model. The dashed red arrow indicates the pathway of air through the pen.

Part 4 was designed to interface with the current clipping station (see Section 2.2.6). For this reason, the current clipping station and clipping pen were measured using a caliper. Part 7 is a hollow cylinder that can move through part 4 thereby pressing the c-clip down. Part 7 is connected to part 5 with an interference fit. If the interference fit is not sufficient to connect the two parts, A hole through the side of part 5 (H_1) allows for applying a tap on part 7 to ensure interference. If this is still not sufficient, glue can be applied through the same hole. Part 5 can slide inside part 6 (red double-headed arrow in Figure 4.3). Part 2 is a spring that acts between the two parts (part 5 and part 6). Part 6 has a thread on the outside that is used to screw it in part 3. How far part 6 is screwed in part 3, determines the maximum and minimum amount of force the spring acts on part 5, and thereby on the c-clip via part 7, when the clipping pen is pressed down. The maximum and minimum amount of force that is applied on the c-clip can therefore be adjusted by tightening or loosening part 6 in part 3. Another spring (part 1) is included that acts between part 4 and 3. This spring causes parts 7, 5, 4, and 6 to retract when releasing the clipping pen after pressing it down. A dowel pin (part 10) through H_2 is included to interface with the flat side of part 3. This dowel pin ensures H_3 and H_4 remain aligned during c-clip insertion. H_5 is inside a chamber that is in contact with H_3 making sure that H_6 is always connected with H_4 allowing air to flow through the clipping pen (dashed line Figure 4.3). Lastly, part 8 and 4 have a thread that is used for connecting these two parts. Part 4 has two flat surfaces to allow for tightening using a wrench.

4.2.2. Material choice for new manual clipping pen

The new clipping pen was tested under cryogenic conditions to make a comparison under realistic conditions. The choice of materials for the custom parts should therefore be compatible with cryogenic conditions (cryo-compatible). Other than cryo-compatible, the materials for the parts should be chosen such that the tip of the clipping pen (part 4) remains cold, to avoid contaminating the sample, while the part that is held by the user (part 8) remains at approximately room temperature. For this reason, parts 3, 5, 6, and 8 were made from Torlon (4203) while parts 4 and 7 were made from Stainless Steel (AISI 316). A FE analysis was used to investigate the thermal conduction through parts 4 and 8. Here, radiative and convective heat transfer were neglected. Convective and radiative cooling of the surface of part 8 by liquid nitrogen vapour would also be present on the outside of the current clipping pen. Therefore for this preliminary analysis, the main risk was assumed to be caused by conductive heat transfer.

The FE analysis was performed using COMSOL Multiphysics 5.5. The situation was modelled where the clipping pen is held in liquid nitrogen for some while to cool the tip of the pen. The geometries of parts 4 and 8 were imported from Solidworks 2020. A temperature of 77 K was set at the outside boundaries of the bottom of the clipping pen (part 4). An open boundary with a temperature of 293.15 K was used at the outside of part 8. An initial temperature of 293.15 K was applied for both parts. Material properties available in the COMSOL material library for Torlon (4203) and stainless steel (AISI 316) were used. Automatic meshing by COMSOL was used to apply a fine mesh. A time dependent analysis was performed for 600 seconds with time increments of 1 second.

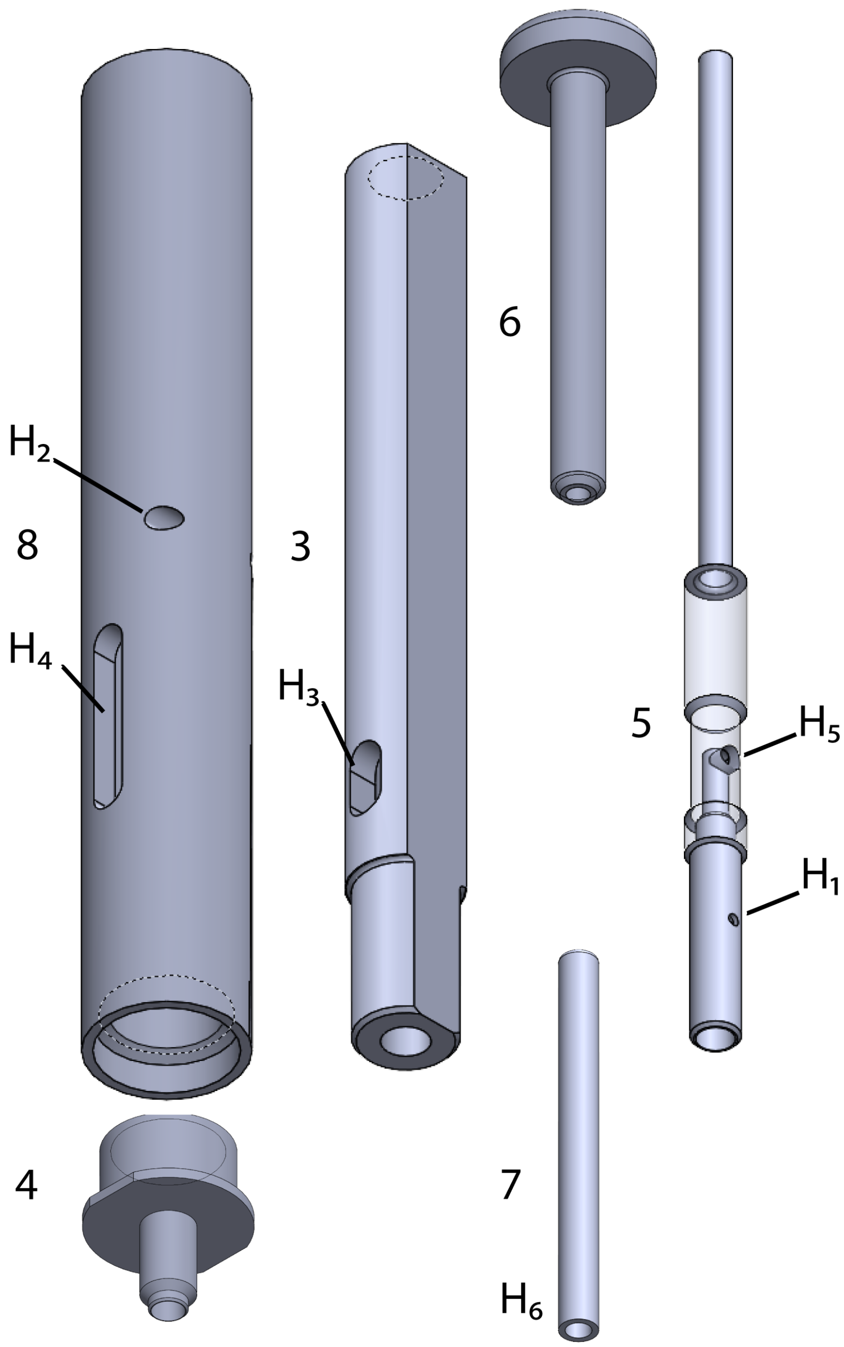

Figure 4.4: CAD model of the custom-made parts for the new manual clipping pen. Some holes are numbered as H_1-H_6 to help explain the working mechanisms of the pen.

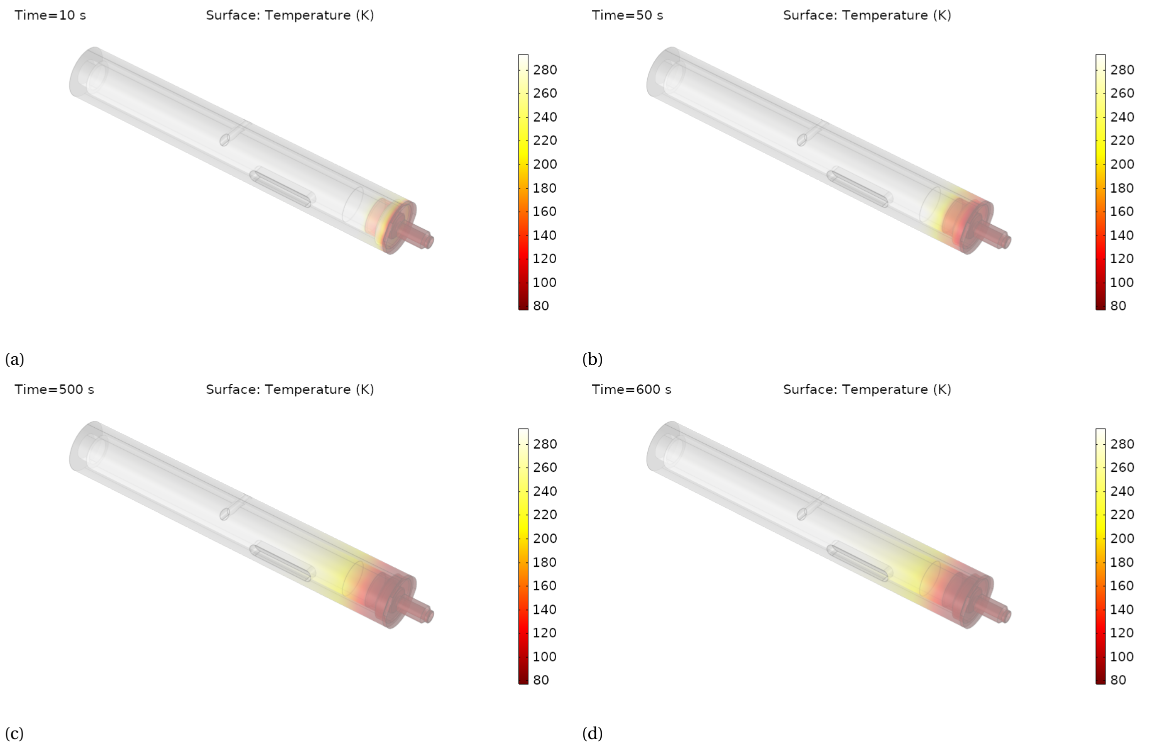

Figure 4.5: Results from the heat analysis of the new clipping pen with the temperature distribution in the pen after (a) 10 seconds, (b) 50 seconds, (c) 500 seconds, and (d) 600 seconds.

Figure 4.5 shows the temperature distribution in the clipping pen after 10 seconds (4.5a), 50 seconds (4.5b), 500 seconds (4.5c), and 600 seconds (4.5d). These results suggest that the temperature in the clipping pen after some time reaches a steady state in which the top part of the clipping pen remains at approximately room temperature. Furthermore, these results suggest that the clipping pen can still be held by hand while cooling it in liquid nitrogen. The previously described materials were therefore selected to be used for manufacturing. All parts were designed to be manufactured using a lathe with some small adjustments afterwards using a milling machine and drill. A picture of the assembled clipping pen can found in Appendix B.

4.2.3. Experiment 1: Methods for the experimental comparison of the two clipping pens

The new clipping pen was compared to the old clipping pen in an experiment: Four Autogrids were clipped using the old clipping pen, and four Autogrids were clipped using the new clipping pen. Clipping was done under cryogenic conditions using the current clipping station. Before clipping, the TEM-grids were plunge frozen using a Leica EM GP2. Clipping was performed by an experienced user to lower the chances of damaging the TEM-grids in other clipping steps (e.i. c_1, c_2, and c_4). Images of TEM-grids were taken before and after clipping using a cryo-LM (Leica DM6 FS). The TEM-grids did not have many distinct features since there were no samples on the TEM-grids. The images could therefore not be merged automatically. Therefore, the images were merged manually. The fragile carbon layer on the TEM-grids was inspected before and after clipping using these images. The number of damaged and undamaged holes before and after clipping were counted, and relative values were calculated. Results from these experiments are given in Section 5.1. The implications of these results on designing an automated c-clip insertion device will be addressed in the discussion in Section 6.1.

4.3. Rotating the Autogrid cartridge

4.3.1. Design of Autogrid holder

The new clipping procedure described in Section 4.1 includes two extra steps to solve the two problems described in Section 3.5 (p_1 and p_2). The Autogrid cartridge is rotated in step C_2. If the orientation of the TEM-grid that is placed in the Autogrid cartridge is known, rotating the Autogrid cartridge can be used to adjust the relative orientation of the TEM-grid with respect to the Autogrid cartridge. The clipped Autogrid is rotated in clipping step C_5, to adjust the orientation of the Autogrid with respect to the gripper fingers retrieving the Autogrid in the last clipping step (C_6). Using this approach, the same mechanism can be used for rotation in clipping steps C_2 and C_5. Multiple conceptual designs were considered whereafter one of them was selected for preliminary testing and manufacturing.

Figure 4.6 shows the technical drawing of the design that was selected for manufacturing. This holder was designed for holding and rotating the Autogrid and Autogrid cartridge. The holder will hereafter be referred to as Autogrid holder.

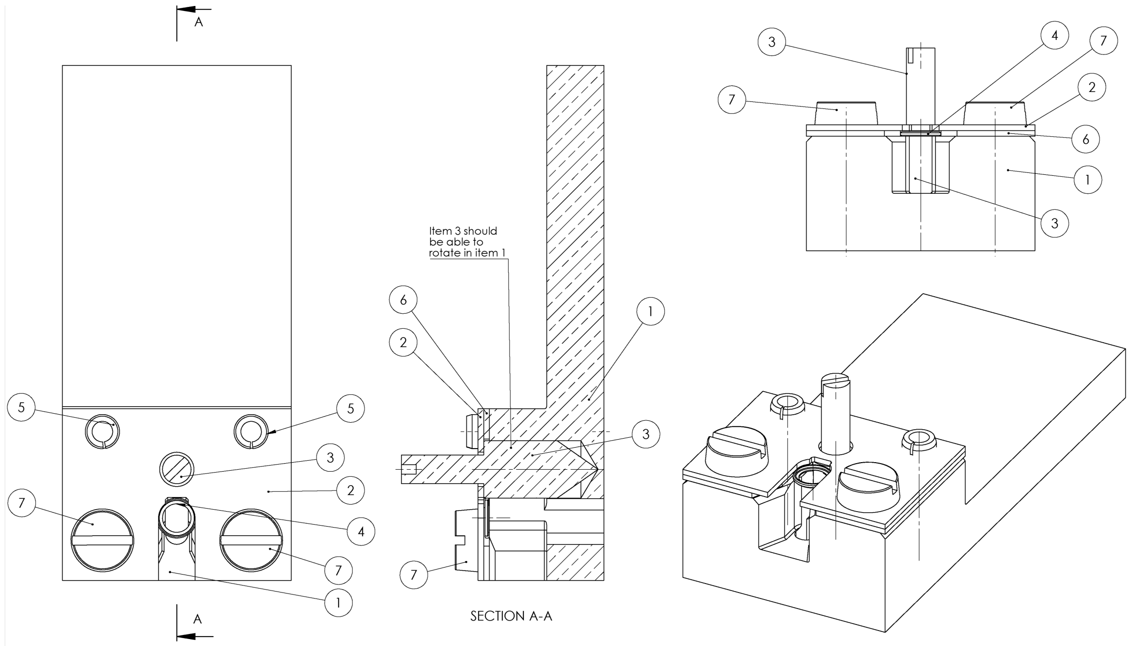

Figure 4.6: Technical drawing of the assembly of the Autogrid holder. Parts are numbered to help explain the mechanisms in the Autogrid holder.

First, preliminary tests were performed using a 3D printed preliminary version of the design shown in Figure 4.6. Figure 4.13b shows how an Autogrid cartridge is retrieved from one of the 3D-printed preliminary versions of the Autogrid holder. The mechanism of the 3D printed versions was similar to that of the design selected for manufacturing. Therefore, the mechanism used for rotating the Autogrid will be described using the drawing given in Figure 4.6.

The Autogrid holder consists of four main parts: a milled part (part 1), two plates on top of the milled part (parts 6 and 2) that are laser cut, and a part that rotates in the milled part (part 3) made on a lathe. The Autogrid (part 4 is an Autogrid cartridge included in the assembly) is aligned with part 3 using the two plates. The sides of the Autogrid interface with part 6, the top of the Autogrid interfaces with part 2, and the bottom of the Autogrid interfaces with the milled part (part 1). By placing the Autogrid holder under an angle with the gravitational forces the side of the Autogrid will remain in contact with the rotating part (part 3). This was illustrated before in Figure 4.1 where the Autogrid holder without the top plate (part 2) and gravitational forces are shown. The angle between the gravitational force and the Autogrid should be such that the frictional force, which is determined by the normal force between the rotating part and the Autogrid (and thus by the angle between the Autogrid and the gravitational force), is large enough to rotate the Autogrid. The friction force between the rotating part and the Autogrid should therefore also be large enough to overcome any frictional forces acting on the sides of the Autogrid by the plates. Two spring pins (part 5) are used to align the two plates with the milled part, and two screws (part 7) are used to hold the parts together. With the Autogrid holder, the frictional forces between part 3 and the Autogrid are used for rotating the Autogrid. In preliminary tests with 3D printed versions of the Autogrid holder slip was observed between the rotating part and the Autogrid. A hole through the bottom of the milled part allows for observing the markers that are at the bottom of the Autogrid cartridge. Using this approach, a certain amount of unpredictable slip is acceptable since the orientation of the Autogrid cartridge can be monitored. The two perpendicular flat surfaces of the milled part (part 1) can be used to align the Autogrid holder. A cut-out on top of the rotating part (part 3) can be used as interface with a flat screw driver to manually rotate the Autogrid. More pictures of the manufactured parts of the Autogrid holder can be found in Appendix B.

For a final design the rotating part can be connected to an actuator. Part 3 or a newly designed part can be used for this purpose. The Autogrid holder can also be extended by an additional milled part to help align the c-clip insertion tool in clipping step C_4. An example is shown in Figure 4.1 in the illustration of the fourth clipping step (C_4).

Preliminary tests were done to determine an optimal angle of the Autogrid holder with respect to the gravitational forces using a bench vise (Figure 4.7a). Here, the normal force between the Autogrid and rotating part of the Autogrid holder should be large enough to enable rotation of the Autogrid with the Autogrid holder. Furthermore, the TEM-grid should fall into the Autogrid cartridge when releasing it above the Autogrid cartridge.

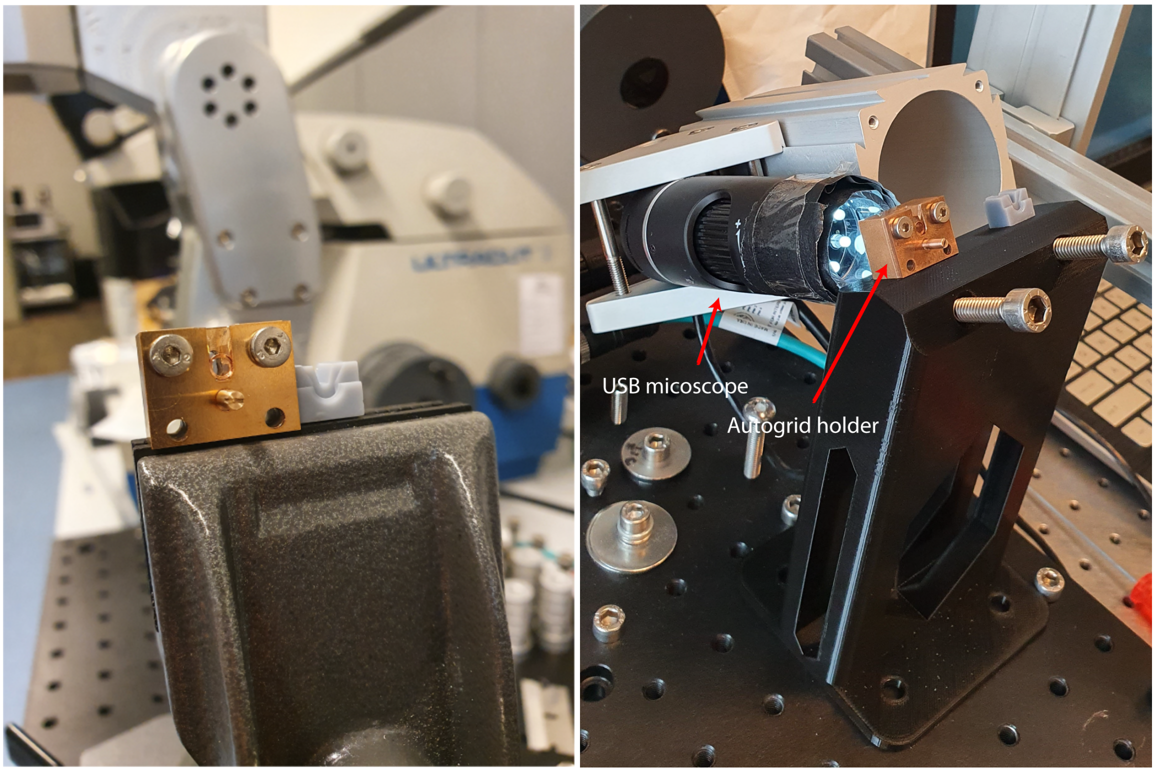

(a) (b)

Figure 4.7: Pictures of (a) the test setup with the Autogrid holder in a bench vise to obtain the required angle of the Autogrid holder with respect to the gravitational force, and (b) the 3D printed interface in which the Autogrid holder is at the obtained required angle with the gravitational force.

The angle obtained from these preliminary tests, was used in the design of an interface for mounting the Autogrid holder to an optical breadboard. This interface was printed using a FDM printer and is shown in Figure 4.7b (black part). This figure also shows the USB microscope that was used for observing the markers at the bottom of the Autogrid to identify the orientation of the Autogrid in the Autogrid holder. Preliminary tests were performed where the Autogrid cartridge was manually rotated to the preferred orientation, after which the TEM-grid was placed in the Autogrid cartridge.

4.3.2. Marker identification

To enable automatic adjustment of the orientation of the Autogrid cartridge and Autogrid in the Autogrid holder using the approach proposed in this report, the markers on the bottom of the Autogrid have to be detected automatically. Images of the bottom of the Autogrid in multiple orientations were acquired with the USB microscope in the test setup shown in Figure 4.7b. Two approaches were used for detecting the markers on the bottom of the Autogrid namely: 1) a more traditional approach to image recognition where the geometrical properties of the markers are used for detection. Since the markers on the Autogrid cartridge are circular, a Circular Hough Transform (CHT) was used for detecting the markers. 2) The second approach to marker identification was based on a machine learning (ML) principle. The Cascade Object Detector available in MATLAB was trained using images of the Autogrid cartridge taken with the USB microscope. Markers were manually selected on images of the bottom of the Autogrid. These images with selected markers were used to train the algorithm. The MATLAB codes developed for marker detection are given in Appendices D.2, D.3, D.4, and D.5.

4.3.3. Experiment 2: Methods for experimental testing of automatic Autogrid orientation adjustment

Experiment 2A
In experiment 2A, the two approaches to marker detection were compared (ML and CHT). Both algorithms were used to detect the markers on the Autogrid cartridge. The marker detection algorithms were used on the same 164 images of the bottom of the Autogrid cartridge. These 164 images were obtained by automatically rotating the Autogrid and making snapshots using the test-setup described in the next subsection (Figure 4.9b). The obtained results were classified using a confusion matrix (as described by Sokolova and Lapalm in 2009 [47]). A confusion matrix (shown in Table 4.1) contains True positives (TP), False Positives (FP), False Negatives (FN), and True Negatives (TN). For object detection in an image, True Negatives do not exist. After all, the whole area outside of the detected object should be classified as true negative. Therefore, TP, FP, and FN were counted for the 164 images used for testing the algorithms.

Table 4.1: Confusion matrix, this table was adapted from Sokolova and Lapalm, 2009 [47]

Data class:	Classified as positive:	Classified as negative:
Positive	True Positive (TP)	False Negative (FN)
Negative	False Positive (FP)	True Negative (TN)

From these three variables the precision (P) was calculated as:

$$P = \frac{TP}{TP + FP} \tag{4.1}$$

the Recall (R) was calculated as:

$$R = \frac{TP}{TP + FN} \tag{4.2}$$

and a harmonic mean (F1) was calculated as:

$$F1 = 2\frac{P \cdot R}{P + R} \tag{4.3}$$

These variables can be interpreted as follows:

- Precision: The relative amount of true detected markers to the total amount of detected markers, measuring how well the algorithm can detect only relevant objects [47].
- Recall: The relative amount of true detected markers to the total markers that should be detected, measuring how well the algorithm can find all objects it should detect [47].
- F1 score: This score is used to combine the previous two variables [47].

The precision, recall, and F1 score for the two algorithms was compared. Four different approaches were used to detect the markers on the Autogrid cartridge using the two algorithms:

1. CHT: A region of interest (ROI) was manually selected based on one image and applied to all 164 images. Within this region, the CHT marker detection algorithm was used to detect the markers. All detected markers were used to calculate the precision, recall, and F1 score.
2. CHT_{mc}: The same approach as described above in item 1 with one extra step: Based on one image, a mask was created masking the center region of the Autogrid cartridge in which there are no markers. This mask was applied to all images (see Figure 4.8c).

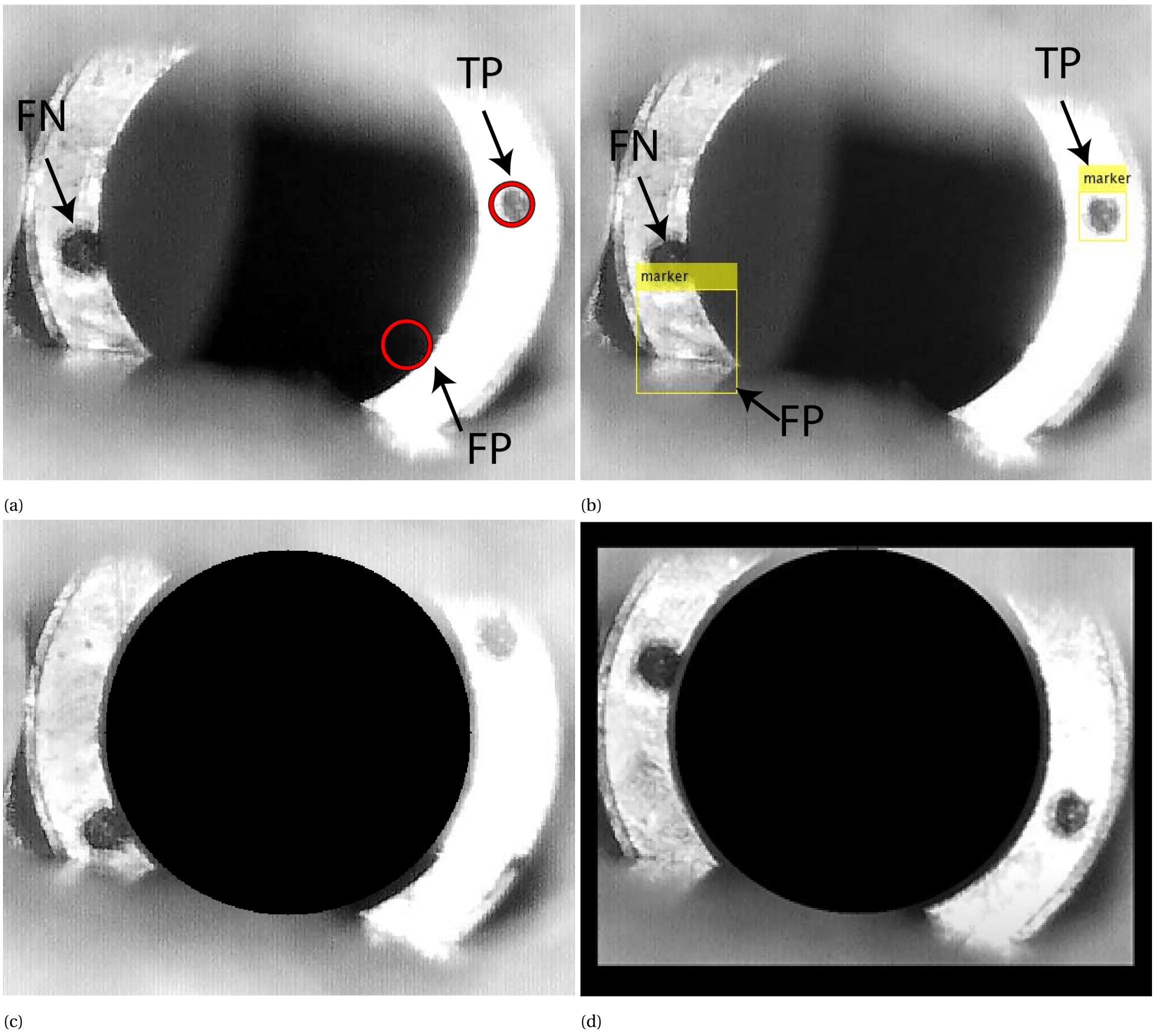

Figure 4.8: (a) Illustration showing TP, FP, and FN, with the CHT approach, (b) illustration showing TP, FP, and FN, with the ML approach, (c) illustration of the mask used with the CHT*mc* approach, and (d) illustration of the mask used with the ML*mc* approach.

3. ML: The ML algorithm was trained and used to automatically detect the ROI in the image. The square box shown in Figure 4.8d represents one of the automatically detected regions of interest. A second ML algorithm was trained (both algorithms were trained using the approach described in 4.3.2) to automatically detect the markers. Thereafter, it was used inside the ROI to detect the markers. All detected markers were used to calculate the precision, recall, and F1 score.

4. ML$_{mc}$: The same approach as described above in item 3 with one extra step: Based on one image, a mask was created masking the center region of the Autogrid cartridge in which there are no markers. This mask was applied to all images (see Figure 4.8d).

Figure 4.8 shows examples of markers identified as TP, FP, and FN for the CHT (Figure 4.8a) and ML (Figure 4.8b) approach. A paired samples t-test (two-tailed) was used to compare the CHT approach to the ML learning approach. A paired samples t-test was also used to evaluate the effect of masking the center region of the Autogrid. The t-value was calculated as [15]:

$$t = \frac{\overline{D}}{S_D/\sqrt{N}} \tag{4.4}$$

Here, $\overline{D}$ is the mean difference between the samples (e.g. TP_{ML}-TP_{CHT}, FP_{ML}-FP_{CHT}, FN_{ML}-FN_{CHT}, P_{ML}-P_{CHT}, R_{ML}-R_{CHT}, or $F_{1,ML}$-$F_{1,CHT}$), S_D is the standard deviation of the differences, and N is the sample size ($N = 164$). From this t-value the effect size was calculated as [15]:

$$r = \sqrt{\frac{t^2}{t^2 + df}} \tag{4.5}$$

with $df = N - 1$. Table 4.2 gives a visual representation of how the t-tests were used for comparing the four different approaches (CHT, CHT$_{mc}$, ML, ML$_{mc}$).

Table 4.2: Visual representation of the comparisons done using a paired samples t-test.

	ML	ML$_{mc}$	CHT	CHT$_{mc}$
ML				
ML$_{mc}$	x			
CHT	x	x		
CHT$_{mc}$	x	x	x	

For a larger sample size normality tests (e.g. Kolmogorov-Smirnoff or Shapiro-Wilk tests) are more likely to show significant differences with a normal distribution, while these differences with a normal distribution are often negligible [15]. Therefore, histograms were used to verify if the differences between the samples were normally distributed.

Experiment 2B
Based on the experimental comparison of the algorithms described above, one of the algorithms was selected for a proof of concept experiment (Experiment 2B). In this proof of concept experiment, an already available stepper motor (Haydon Kerk Nema 8 stepper motor [20]) was attached to the rotating part of the Autogrid holder using 3D printed interfaces. Figure 4.9a shows the CAD model of the experimental setup with the stepper motor. Figure 4.9b shows the 3D printed parts interfacing with the stepper motor and Autogrid holder in the real test set-up. Parts were printed using a FDM printer (red parts) and a SLA printer (orange parts). The stepper motor was controlled using an in-house available Trinamic TMCM-6110 [53] and MATLAB. The selected marker detection algorithm was used to automatically change the orientation of the Autogrid to the orientation where two markers are on the left (see Figure 5.5 in the chapter with results in Section 5.2.2) seven consecutive times. This experiment was performed at room temperature. The results of these two experiments (experiment 2A and experiment 2B) are given in Section 5.2. The MATLAB code used for this experiment is given in Appendix D.5.

4.4. Automatic handling of Autogrids and Autogrid cartridges

The first and last step of the new clipping procedure consist of handling the Autogrid (C_6) and Autogrid cartridge (C_1). Although no failure is expected in these steps (see Section 3.1), automation of the full clipping procedure is desired. To automatically handle Autogrids the choice was made for the already available Mecademic Meca500 six-axis industrial robot arm with the MEGP 25 parallel gripper shown in Figure 4.10. Technical drawings of the MEGP 25 can be found in Appendix C.1.

The MEGP 25 gripper requires custom gripper fingers to enable handling the Autogrid cartridge. In Figure 4.11a the geometry and dimensions with tolerances of the Autogrid cartridge are specified. When using gripper fingers with two parallel surfaces, the Autogrid can be gripped on the sides or on the top side (illustrated in Figure 4.11b).

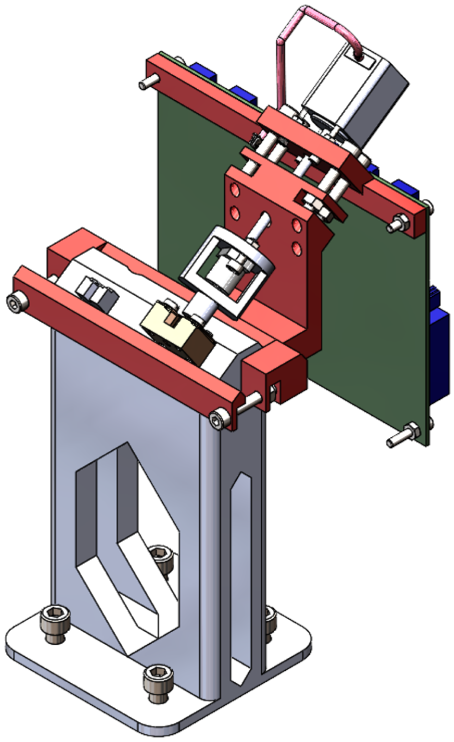

(a)

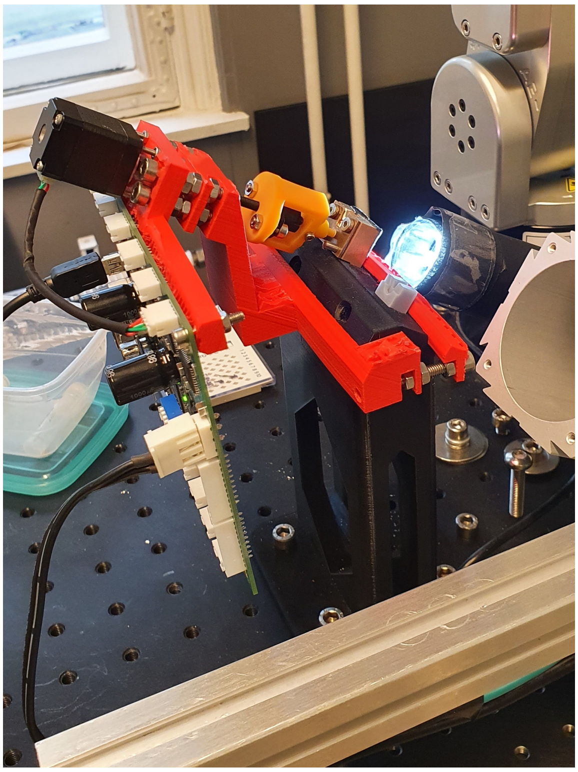

(b)

Figure 4.9: (a) CAD model of the parts designed for attaching an already available stepper motor to the rotating part of the Autogrid holder. (b) Test setup where 3D printed parts are used to attach an already available stepper motor to the rotating part of the Autogrid holder.

When choosing on which side of the Autogrid the gripper finger will act (top or side), the next clipping step has to be considered (C_2). In the next step, the Autogrid cartridge will be rotated to a preferred orientation. In this case, the design choice was made to rotate the Autogrid cartridge by a mechanism that acts on the side of the Autogrid cartridge. Design choices for rotating the Autogrid cartridge were described in Section 4.3. Because this mechanism acts on the side of the Autogrid cartridge, the gripper fingers were designed to act on the top of the Autogrid cartridge. Preliminary testing was performed using multiple 3D printed gripper fingers (g_1, g_2, g_3, and g_4). The designs and results of preliminary testing of these gripper fingers are described in the following subsections.

Preliminary observations of the MEGP 25 gripper revealed that the two planes that interface with the gripper fingers were not parallel (observed by eye). This was taken into consideration when designing the gripper fingers.

4.4.1. Design of gripper fingers for automatic handling of Autogrids

g_1: Tweezer tips and an interface printed in resin

Figure 4.12 shows the first gripper fingers (g_1) designed for handling the Autogrid cartridge. Figure 4.12a shows the computer-aided design (CAD) model, and Figure 4.12b shows the gripper fingers attached to the MEGP 25 gripper, while holding an Autogrid cartridge.

For this design, the tweezer tips of the Ideal-tek 5CFR.SA.1 [19] tweezers were attached to the MEGP 25. An interface between the tweezer tips and the MEGP 25 was printed in resin using the Prusa SL1 Stereolithography (SLA) printer. The surface of the 3D printed part at which the tweezer tips interface, was designed to be under a slight angle to ensure closing of the tweezer tips.

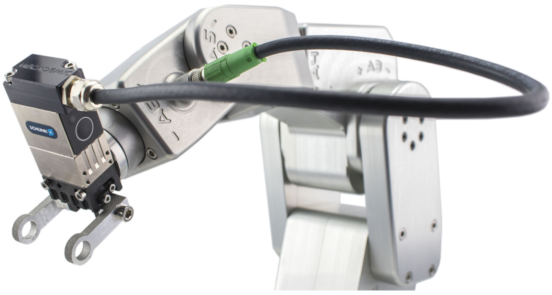

Figure 4.10: Mecademic Meca 500 and MEGP-25 grippers, image from [33]

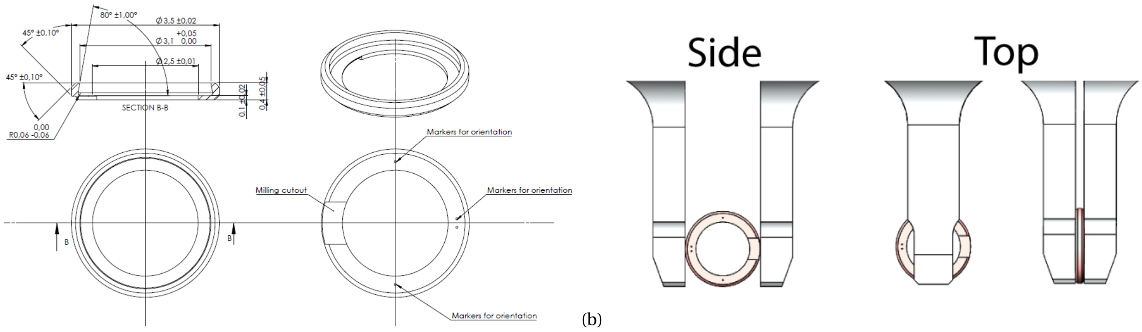

(a) (b)

Figure 4.11: (a) Technical drawing of the Autogrid cartridge (b) two different methods for gripping the Autogrid using parallel gripper fingers.

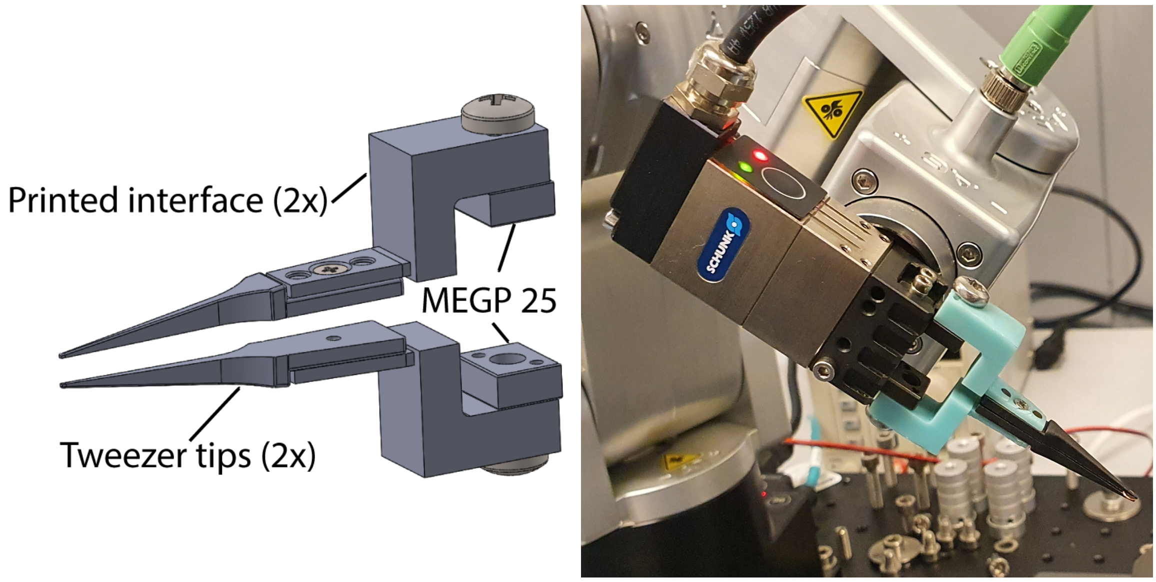

(a) (b)

Figure 4.12: (a) CAD model of the first gripper fingers (g_1) that were designed for picking up Autogrid cartridges, and (b) an image of the gripper fingers attached to the MEGP 25 gripper while holding an Autogrid cartridge

g_2: Additional spring for a force-controlled-adjustable open gripper finger distance

The second gripper finger design (g_2) is very similar to the first design (g_1). An interface between the tweezer tips of the Ideal-tek 5CFR.SA.1 was printed in resin. Here, more material is added to increase the stiffness of the interface between the MEGP 25 and the tweezer tips. Furthermore, a spring is included between the two gripper fingers. The MEGP 25 gripper can either be in open or closed configuration. The amount of force that is used to close the MEGP 25 gripper can be controlled. By including a spring between the gripper fingers, the gripper can be partially closed. Being able to partially close the gripper fingers can help with alignment of the gripper fingers with the Autogrid cartridge. In this case a spring with a stiffness of 1.21 N/mm was used. The force for closing the MEGP 25 gripper can be set from 0.4 N to 40 N with steps of 0.4 N. When neglecting other forces present between the gripper fingers and gripper (e.g. frictional forces), this should enable partially closing the grippers with incremental steps of 0.33 mm. In reality, frictional forces will have a large influence on the incremental closing steps of these gripper fingers. To allow for attaching the tweezer tips, the gripper fingers have a hole through which a screw driver fits. Similar to the previous gripper finger design (g_1), the surfaces of the 3D printed part of this gripper finger design (g_2) that interface with the tweezer tips were under an angle. Multiple angles were printed and tested in preliminary testing.

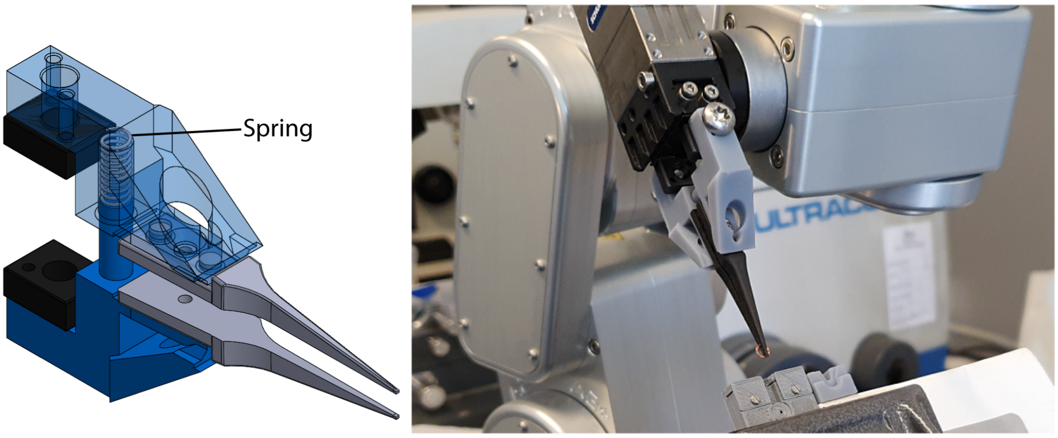

(a) (b)

Figure 4.13: (a) CAD model of the second gripper fingers used for preliminary testing (g_2), and (b) 3D printed version of the second gripper fingers (g_2) holding an Autogrid cartridge.

g_3: Full tweezers gripper design

Figure 4.14 shows the third gripper finger design (g_3) that was tested in preliminary testing. Here, instead of attaching the tweezer tips to the MEGP 25, the entire tweezers are attached to the gripper. The adaptor plate (see Appendix C.1 Figure C.3) that is used to interface between the MEGP-25 and the flange on the Meca500, is replaced by a 3d printed interface used to attach tweezers to the Meca500. The side of tweezers is aligned to the printed interface. The tweezers are attached by screwing a holding plate to the printed interface. Two gripper fingers are used for closing the tweezers by simple contact with the tweezers. A spring is included between the gripper fingers similar to the spring between the previously designed gripper fingers (g_2). A screw and nut between the gripper fingers are used to adjust the distance between the gripper fingers when the gripper is opened. Tightening this "adjustment screw" decreases the distance between the gripper fingers when the gripper is in open configuration.

The two gripper fingers were printed using fused deposition modeling (FDM) printing (red parts in Figure 4.14b). The interface between the Meca500 and the MEGP-25, and between the Meca500 and the tweezers, was printed in resin using a SLA printer. The holding plate was printed in resin using a SLA printer. The holes in replacement part of the adapter plate were manually tapped to create the required thread. The holes for the screws holding the adapter plate were manually tapped, and nuts on the other side of the holes were used to ensure a tight connection between the holding plate and the tweezers. Figure 4.14b shows how the previously mentioned Ideal-tek 5CFR.SA.1 tweezers are used with the third gripper finger (g_3) to hold an Autogrid cartridge.

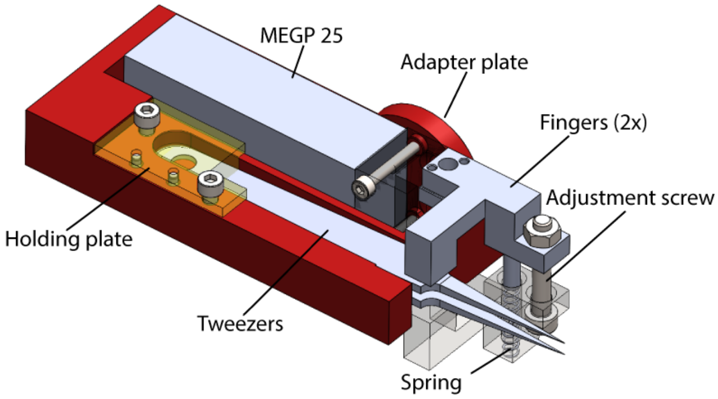

(a)

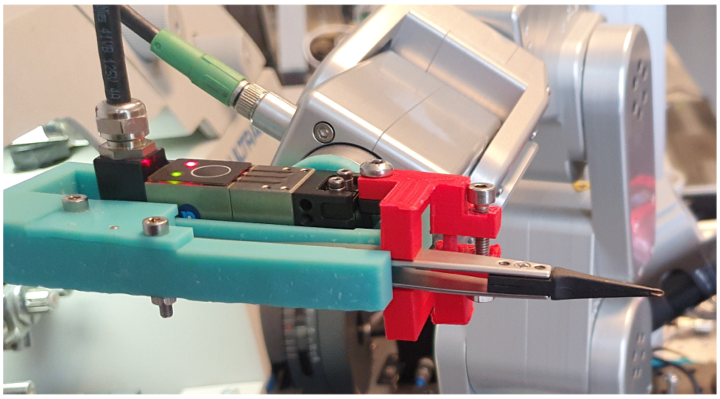

(b)

Figure 4.14: (a) CAD model of the third gripper fingers (g_3), and (b) 3D printed version of the third gripper fingers (g_3) holding an Autogrid cartridge.

g_4: Two fold gripper fingers

The last designed gripper fingers that were used for preliminary testing are shown in Figure 4.15. These gripper fingers (g_4) were designed to have two surfaces for gripping. One of these surfaces was designed for picking up Autogrid cartridges, and one of these surfaces was designed for picking up TEM-grids.

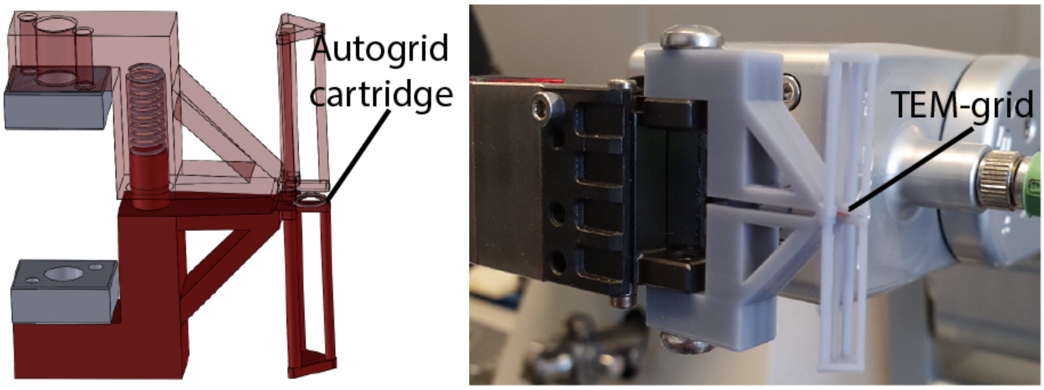

(a) (b)

Figure 4.15: (a) CAD model of the fourth gripper fingers (g_4), and (b) 3D printed version of the fourth gripper fingers (g_4) holding a TEM-grid.

The difference in thickness between the TEM-grids (25 µm) and Autogrid cartridges (0.4 mm) is used to ensure different parts of the gripper fingers are in contact with an Autogrid cartridge than with a TEM-grid (see Figure 4.16) when closing the grippers. These gripper fingers were printed using a SLA printer. The three beams on the two gripper fingers shown in Figure 4.15 were used for support while printing and were meant to be removed for further testing.

Using such a gripper for TEM-grids would require the use of a special holder for TEM-grids (e.g. the one partially shown in Figure 4.16) to allow for picking up TEM-grids. Using gripper fingers to enable handling of TEM-grids with the MEGP-25 and Meca500 will be described in Section 4.5.

4.4.2. Gripper fingers selection

All four gripper fingers (g_1, g_2, g_3, and g_4) described above, were used for preliminary testing: The Meca500 was aligned to automatically retrieve an Autogrid cartridge from a holder. After automatically retrieving the Autogrid cartridge, it was automatically placed back in the holder. The same test was performed using a clipped Autogrid (this is required for the final clipping step: C_6).

Both the Autogrid and Autogrid cartridge were successfully retrieved automatically from a holder designed for the storage of the Autogrid using the first three gripper fingers (g_1, g_2, and g_3). Similarly, automatically placing the Autogrid and Autogrid cartridge back in the same holder, was successful with the first three gripper fingers. The fourth gripper fingers (g_4) were not used successfully for automatic handling of Autogrid cartridges and clipped Autogrids because they were incompatible with the Autogrid holder used in these preliminary tests (prototypes used for Autogrid holders are elaborated on in Section 4.3). Preliminary tests in which the Autogrid cartridge was manually placed between the gripper fingers before closing the gripper fingers suggested that these gripper fingers (g_4) would also be capable of automatic handling of Autogrids and Autogrid cartridges.

Based on the above-mentioned preliminary tests, the third gripper fingers (g_3) were selected for further experimental tests. Although all gripper fingers could be used for automatic handling of Autogrids, these gripper fingers were selected for the following reasons: 1) The adjustment screw allows for a small opening between the tweezers when the gripper is in open configuration, this helps with aligning the gripper fingers with the Autogrid. 2) The fact that the interface planes of the MEGP-25 are not parallel, does not effect the surfaces in contact with the Autogrid. 3) The tweezers can be replaced by a different set of tweezers if this is necessary in a later stage. Some features such as partial opening of gripper fingers might also be included by requesting a software update from the manufacturer (Mecademic) in a later stage.

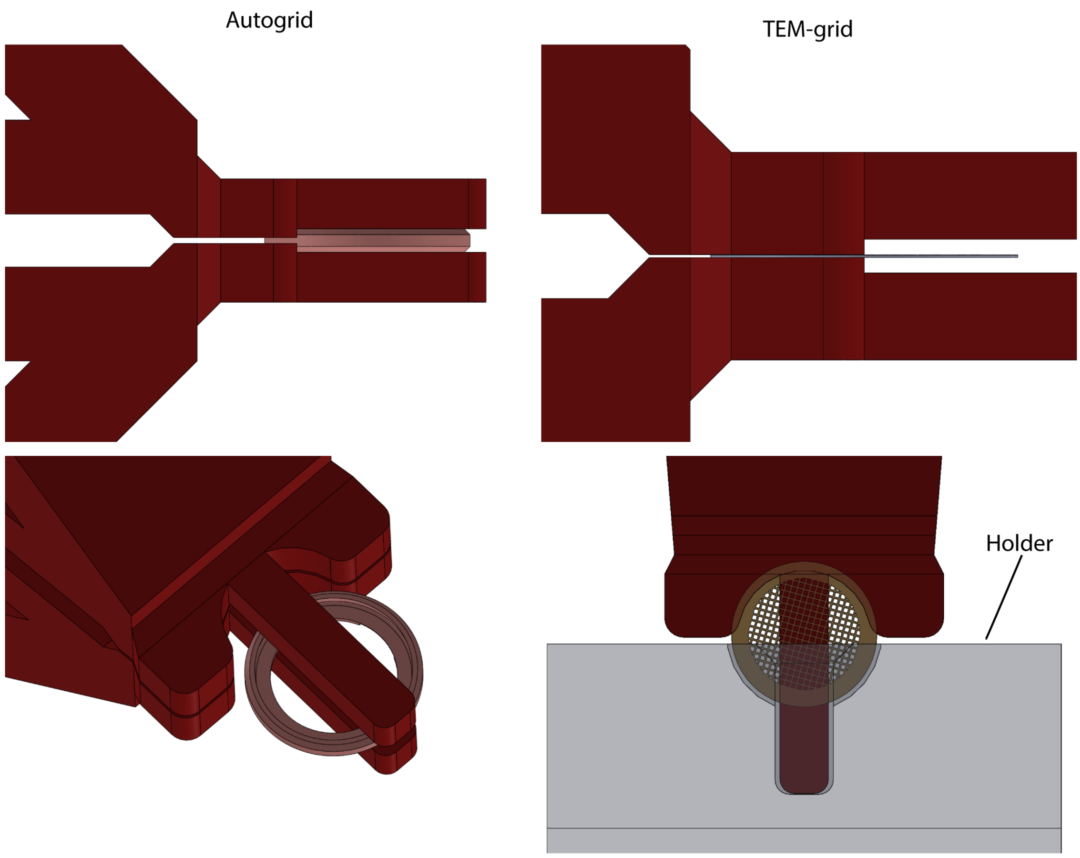

Figure 4.16: Illustration of how the difference in thickness between the Autogrid and TEM-grid is used in the design of the fourth gripper fingers (g_4).

4.4.3. Experiment 3: Methods for testing automatic Autogrid handling

For final testing of the selected gripper fingers (g_3) a clipped Autogrid was used. Since the gripper fingers use the top and bottom side for holding the Autogrid cartridge, no differences were expected between handling clipped Autogrids and Autogrid cartridges. This was confirmed by preliminary testing in which no differences were noticed in handling Autogrids and Autogrid cartridges. A clipped Autogrid was retrieved from an Autogrid holder seven times. An USB microscope (see Figure 4.7b) was used to study the orientation of the Autogrid before retrieval. After retrieval, the Autogrid was automatically transported to the microscope of an ultramicrotome (Reichert-Jung Ultracut E) to again study the orientation of the Autogrid. This approach was used to investigate if retrieving the Autogrid would change the orientation of the Autogrid in the gripper fingers retrieving it. Retaining the orientation of the Autogrid in the gripper fingers while retrieving the Autogrid is important for the new clipping procedure as described in Section 4.1. Retaining orientation while placing the Autogrid cartridge in the first clipping step of the proposed new procedure (C_1) is less important as the Orientation of the Autogrid cartridge can be adjusted in the following clipping step (C_2). This experiment was performed at room temperature. Results from this experiment are described in Section 5.3. Figure 4.17 shows how the Autogrid is automatically retrieved from the Autogrid holder (Figure 4.17a and 4.17b) and how the Autogrid is inspected under the microscope of the ultramicrotome (Figure 4.17c and 4.17d).

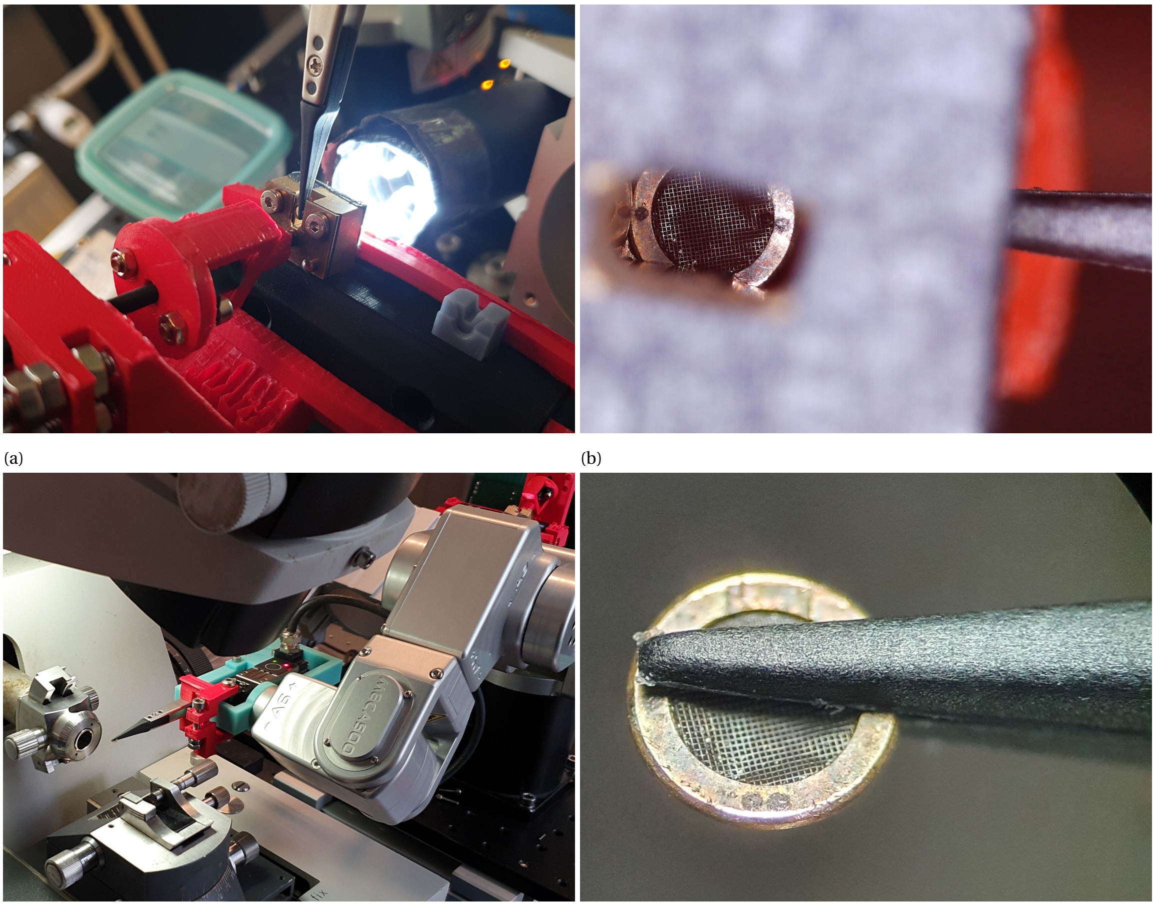

(a) (b) (c) (d)

Figure 4.17: Pictures of the procedure used in experiment 3: (a) the Autogrid is retrieved from the Autogrid holder (b) the orientation of the Autogrid in the selected gripper fingers is checked using an image obtained with the USB-microscope, and (c) and (d) the orientation of the Autogrid in the selected gripper fingers is checked under the microscope of the ultramicrotome.

4.5. Automatic handling of TEM-grids

4.5.1. Gripper finger design for automatic handling of TEM-grids

For automatic handling of TEM-grids the same Meca500 and MEGP-25 that were mentioned before, were used. The grippers fingers that were designed for automatic handling of Autogrids (g_1, g_2, g_3, and g_4) were also used for preliminary testing of automatic handling of TEM-grids (see Appendix B for additional images). To perform preliminary tests with these gripper fingers different TEM-grid holders were printed in resin using a SLA printer. From these holders the TEM-grids could be retrieved. Two of these holders used for preliminary tests are shown in Figure 4.18. Gripper fingers g_1, g_2, and g_3 were tested using the holder (TEM-grid holder 1) in Figure 4.18a and Figure 4.18c. This holder was designed to aid with aligning the gripper fingers with the rim of the TEM-grid. It was also designed to interface with an alternative method for picking up TEM-grids which was not developed further and is described in Appendix A. Gripper fingers g_4 were tested using the holder on the right in Figure 4.18.

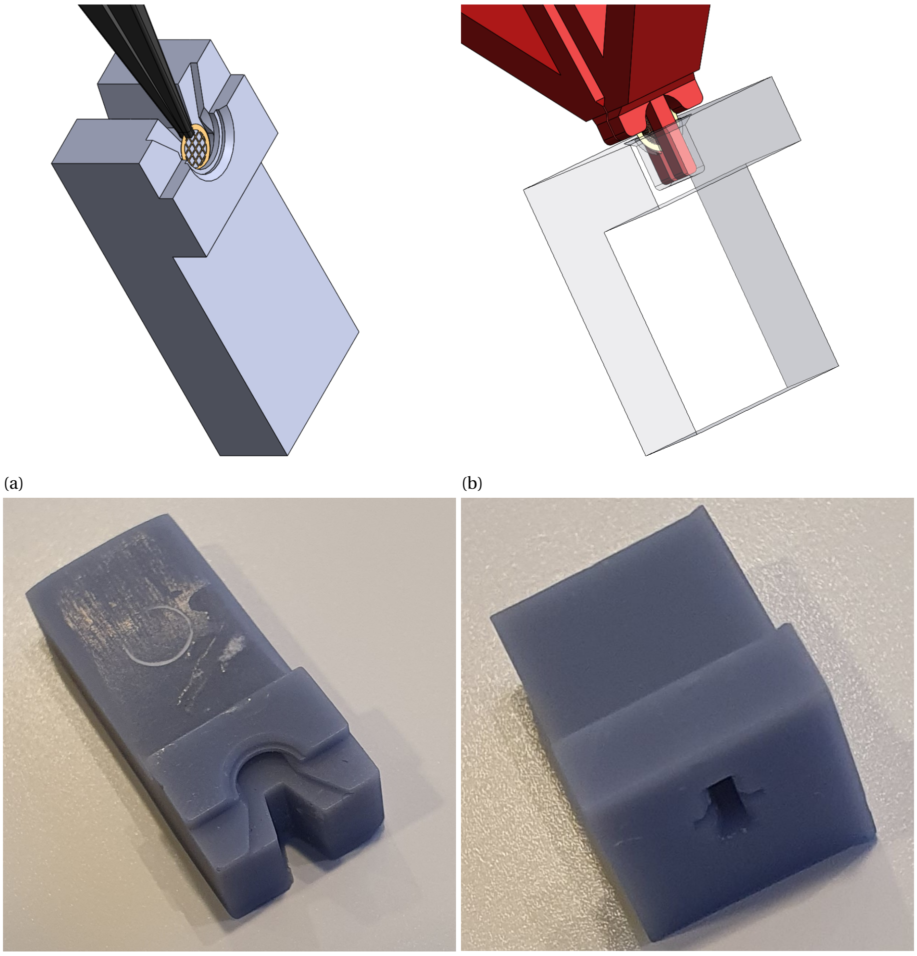

(a) (b) (c) (d)

Figure 4.18: (a) CAD model of TEM-grid holder 1, (b) CAD model of TEM-grid holder 2, (c) TEM-grid holder 1 printed in resin, (d) TEM-grid holder 2 printed in resin.

These preliminary tests consisted of trying to automatically pick up TEM-grids from two TEM-grid holders (TEM-grid holder 1 and TEM-grid holder 2). TEM-grids could successfully be retrieved from these holders automatically using gripper fingers g_2, g_3, and g_4. Gripper fingers g_1 were not used successfully for retrieving TEM-grids. Figure 4.19a shows how tips of the tweezer tips are pushed open. Because the TEM-grids are very thin (25 µm) this opening results in not being able to retrieve TEM-grids with these gripper fingers.

Upon closer inspection of the tips of the tweezer tips irregularities were observed (red arrows in Figure 4.19b). These irregularities were also observed in three pairs of tweezer tips that were completely new. As these irregularities can potentially damage the fragile TEM-grids, gripper fingers g_3 were used with a different set of tweezers. Figure 4.20 shows how the Dumont #5 (AGT5291) tweezers were used to retrieve a TEM-grid in preliminary tests. Using the design for g_3 with the Dumont # 5 tweezers will hereafter be referred to as g_5. Preliminary tests were also done where Autogrids were picked up using these new gripper fingers (g_5). Picking up Autogrids was however not possible without damaging the very fine tips of the Dumont #5 tweezers.

Using these Dumont #5 tweezers however does introduce the possibility of integrating the cryo-ET workflow further. Before clipping, TEM-grids are plunge frozen (see Section 2.2). One of the plunge freezing devices that is currently most widely used uses a modified version of the Dumont #5 tweezers shown in Figure 4.21. These tweezers are used for manually retrieving TEM-grids. Thereafter these tweezers are connected to the plunge freezing device. The main differences between these so-called Vitrobot tweezers and the Dumont # 5 tweezers are: the vitrobot tweezers have a hole that is used for alignment, and the Vitrobot tweezers are over 30 times more expensive. Using gripper fingers g_5 allows for integrating the second clipping step c_2, where the TEM-grid is placed in the Autogrid cartridge, with the step where the TEM-grid is plunge frozen, into one device.

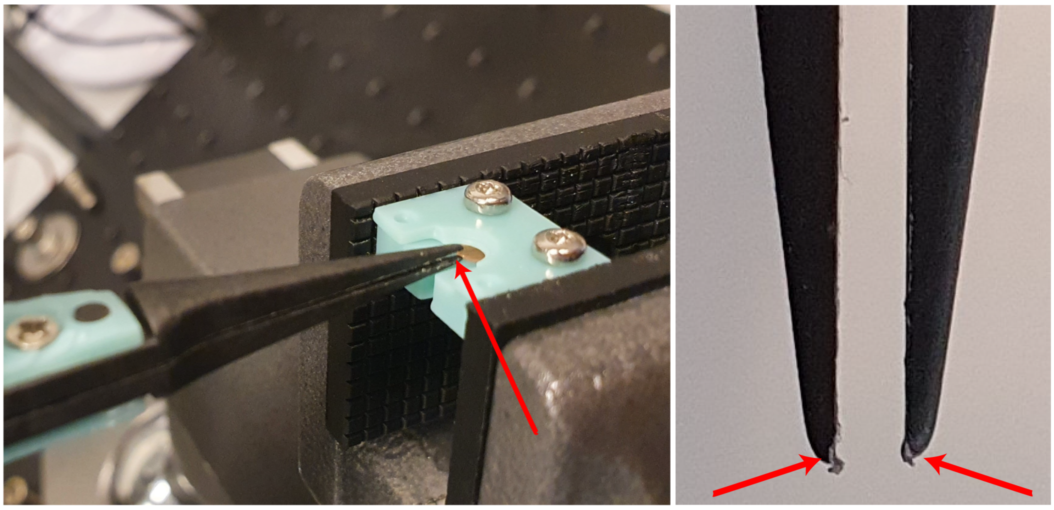

(a) (b)

Figure 4.19: (a) Picture of trying to retrieve a TEM-grid with gripper fingers g_1. The red arrow points at the gap between the tweezer tips that is larger than the thickness of the TEM-grid. (b) The red arrows indicate the irregularities at the tweezer tips

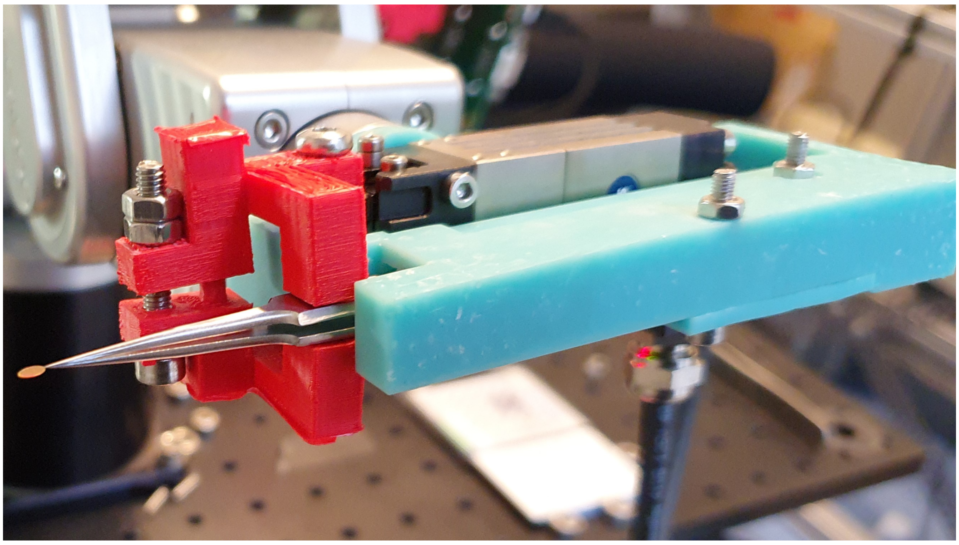

Figure 4.20: Picture of gripper fingers g_5 holding a TEM-grid.

Figure 4.21: Vitrobot tweezers, image obtained from Agar Scientific [46]

4.5.2. Mapping of orientation

The first problem (p_1) described in Section 3.5 concerns the orientation of the TEM-grid with respect to the Autogrid cartridge. To adjust this relative orientation using the Autogrid holder described in 4.3, the orientation of the TEM-grid should be mapped to the Autogrid cartridge. For this purpose a MATLAB code was written which maps the orientation of the TEM-grid to the Autogrid cartridge. The developed MATLAB code is given in Appendix D.7. For now, the choice was made not to automatically detect the orientation of the gripper fingers and the TEM-grid. Preliminary testing using a canny edge filter, suggested such automatic detection should be possible if the light on the gripper fingers with TEM-grid is kept constant. Otherwise, a machine learning algorithm could be used such as the one described in Section 4.3.2 which was used for detecting the region of interest and markers on the bottom of the Autogrid cartridge. Automatic detection of the orientation of the gripper fingers and of the TEM-grid with respect to the gripper fingers was not developed further for this project.

For this project the approach to mapping the orientation of the TEM-grid with respect to the gripper fingers, to the Autogrid cartridge was as follows: The orientation of the gripper fingers was marked by clicking two points on the gripper fingers in an image. Then, in that same image, the center of the TEM-grid and a point on the side of the TEM-grid were selected (an example is given in the chapter with results in Figure 5.17). Subsequently, the center of the Autogrid cartridge was selected, which was used to map the orientation of the TEM-grid with respect to the gripper fingers to the Autogrid cartridge.

4.5.3. Experiment 4: Methods for experimental testing of automated TEM-grid handling

Two experiments were performed with two main goals: experiment 4A) Validating the selected gripper fingers (g_5) for automatic TEM-grid handling and quantifying damage on TEM-grids using these gripper fingers, and experiment 4B) validating the proposed approach for adjusting the relative orientation of the TEM-grid with respect to the Autogrid cartridge. Both experiments (4A and 4B) were performed at room temperature.

Experiment 4A

Two golden TEM-grids and five TEM-grids made of copper were automatically retrieved from a TEM-grid storage box (see Figure 4.22 and Figure 4.23a), using the selected gripper fingers (g_5). The copper and golden TEM-grids both had a holey carbon layer. Subsequently the TEM-grids were imaged using the microscope of an ultramicrotome (Reichert-Jung Ultracut E). The holey carbon layer was inspected (Figure 4.23b). Then, the TEM-grid was placed in the Autogrid cartridge (Figure 4.23c). Thereafter, the Autogrid with TEM-grid inside was manually retrieved from the Autogrid holder with a pair of tweezers, and put on a microscope slide (Figure 4.23d). The holey carbon layer on the TEM-grid was observed under a light microscope and damage was quantified.

Experiment 4B

In experiment 4B the developed MATLAB tool for mapping the relative orientation of the TEM-grid with respect to the gripper fingers to the Autogrid cartridge was tested. For this purpose, five TEM-grids were placed in an Autogrid cartridge using the Meca 500 and the selected gripper fingers. Before placing the TEM-grid in the Autogrid cartridge, an image of the TEM-grid and gripper fingers was obtained using the previously mentioned microscope of an ultramicrotome. Using the developed MATLAB tool, the relative orientation of the TEM-grid with respect to the gripper fingers was mapped to the Autogrid cartridge ten times. This mapped orientation was compared to the orientation of the TEM-grid in the Autogrid cartridge after placement. The orientation of the TEM-grid with respect to the Autogrid cartridge was inspected using the USB-microscope aimed at the bottom of the Autogrid holder. The orientation of the TEM-grid with respect to the Autogrid cartridge after placement was estimated by selecting the center of the TEM-grid and a point on the TEM-grid, similar to the approach described in subsection 4.5.2. The difference between the estimated orientation of the TEM-grid with respect to the Autogrid cartridge after placement and the orientation of the TEM-grid mapped to the Autogrid cartridge, was calculated and reported.

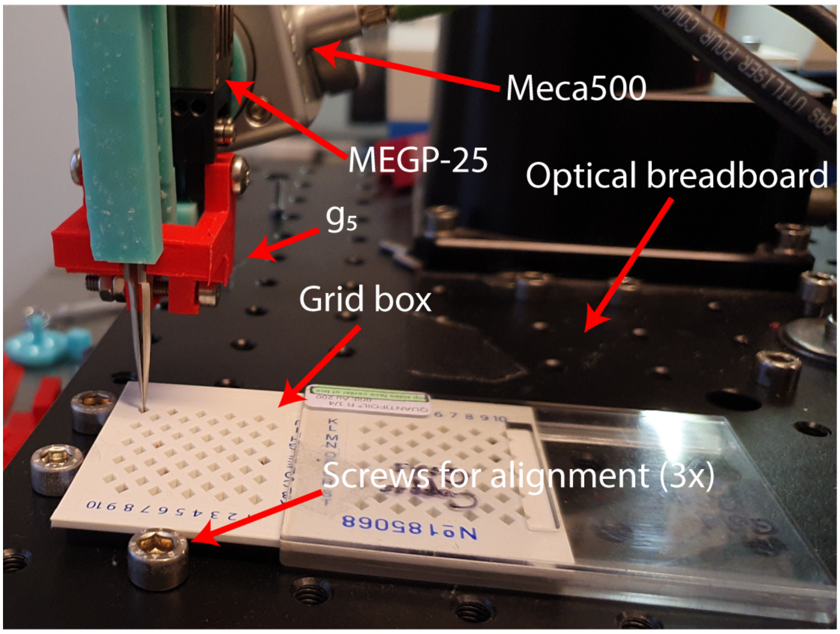

Figure 4.22: Picture of the test setup at the moment a TEM-grid is retrieved from the grid box. Multiple components in the setup are labeled for reference.

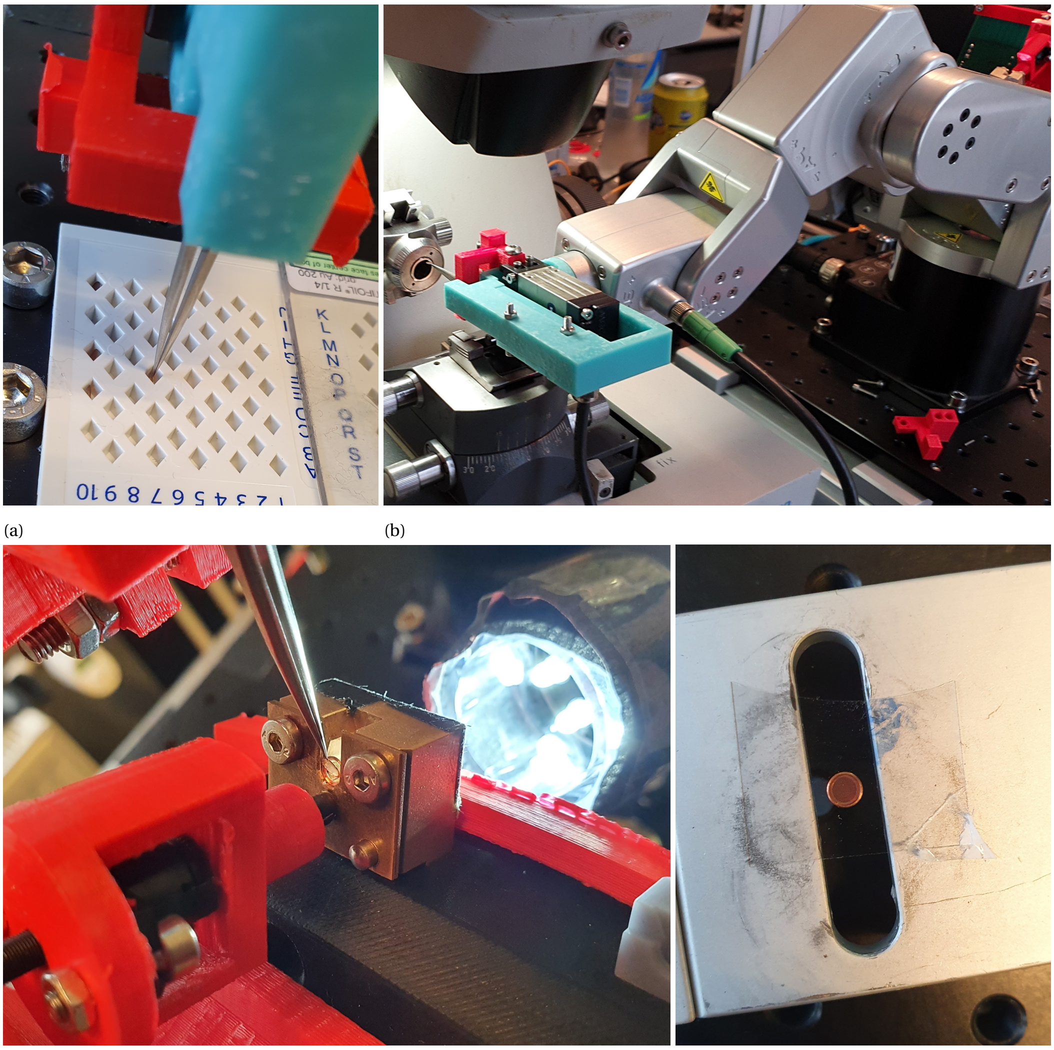

(a) (b) (c) (d)

Figure 4.23: Methods for experimental testing of automated TEM-grid handling: (a) the TEM-grid is retrieved from a TEM-grid storage box, (b) the TEM-grid is inspected under the microscope, (c) the TEM-grid is placed in an Autogrid cartridge, and (d) the TEM-grid and Autogrid cartridge are placed on a microscope slide.

5

Experimental results

5.1. Experiment 1: Comparison of the two clipping pens

Methods for this experiment are described in Subsection 4.2.3. Figure 5.1 shows the manually merged images of the carbon layer on the TEM-grids clipped with the old clipping pen before (5.1a, 5.1c), 5.1e, and 5.1g) and after (5.1b, 5.1d, 5.1f, and 5.1h) c-clip insertion (Methodology for this experiment is given in 4.2.3). Figure 5.2 shows the manually merged images of the carbon layer on the TEM-grids clipped with the new clipping pen before (5.2a, 5.2c, and 5.2e) and after (5.2b, 5.2d, 5.2g, and 5.2f) c-clip insertion. Red arrows are used to indicate holes on the TEM-grids where the carbon layer is damaged. Green arrows are used to indicate holes with an undamaged carbon layer before clipping that had a damaged carbon layer after clipping. For each grid, the following things are reported in Table 5.1: the total number of holes with carbon layer on the TEM-grid that were damaged after clipping (Total Damaged after clipping: TDa), the total number of holes with carbon layer on the TEM-grid that were damaged after clipping but were undamaged before clipping (Damaged after UnDamaged before: DaUDb), the total number of holes with carbon layer on the TEM-grid that were damaged after clipping and were damaged before clipping (Damaged after Damaged before: DaDb), the total number of holes with carbon layer on the TEM-grid that were damaged after clipping and were not visible on the image before clipping (Damaged after Unknown before: DaUb), the total number of holes with carbon layer on the TEM-grid that were not damaged after clipping (UnDamaged after: UDa), and the total number of holes with carbon layer on the TEM-grid that were too contaminated with ice to determine if they were damaged (Con).

Table 5.1: Quantification of the damage observed on the TEM-grids before and after clipping, with the old and new clipping pen. The following are reported: the total number of holes with carbon layer on the TEM-grid that were damaged after clipping (Total Damaged after clipping: TDa), the total number of holes with carbon layer on the TEM-grid that were damaged after clipping but were undamaged before clipping (Damaged after UnDamaged before: DaUDb), the total number of holes with carbon layer on the TEM-grid that were damaged after clipping and were damaged before clipping (Damaged after Damaged before: DaDb), the total number of holes with carbon layer on the TEM-grid that were damaged after clipping and were not visible on the image before clipping (Damaged after Unknown before: DaUb), the total number of holes with carbon layer on the TEM-grid that were not damaged after clipping (Total UnDamaged: TUD), and the total number of holes with carbon layer on the TEM-grid that were too contaminated with ice to determine if they were damaged (Con).

Grids$_c$:	TDa	DaUDb	DaDb	DaUb	TUD	Con	$\frac{DaUDb}{TUD}$	$\frac{TDa}{TUD}$	$\frac{TpDC}{TUD}$
Grid c1	1	1	0	0	234	0	0.4%	0.4%	0.4%
Grid c2	1	1	0	0	262	0	0.4%	0.4%	0.4%
Grid c3	6	1	0	5	221	0	0.5%	2.7%	2.7%
Grid c4	5	4	1	0	253	0	1.6%	2.0%	1.6%
Mean:	3	2	0.3	1	243	0	0.7%	1.4%	1.3%
Grids$_C$:									
Grid C1	4	0	4	0	237	3	0.0%	1.7%	0.0%
Grid C2	6	0	2	4	216	29	0.0%	2.8%	1.9%
Grid C3	NA	NA	NA	NA	NA	NA	NA	NA	NA
Grid C4	3	NA	NA	NA	218	0	NA	1.4%	NA
Mean:	4	0	3	1	224	16	0.0%	1.9%	0.9%

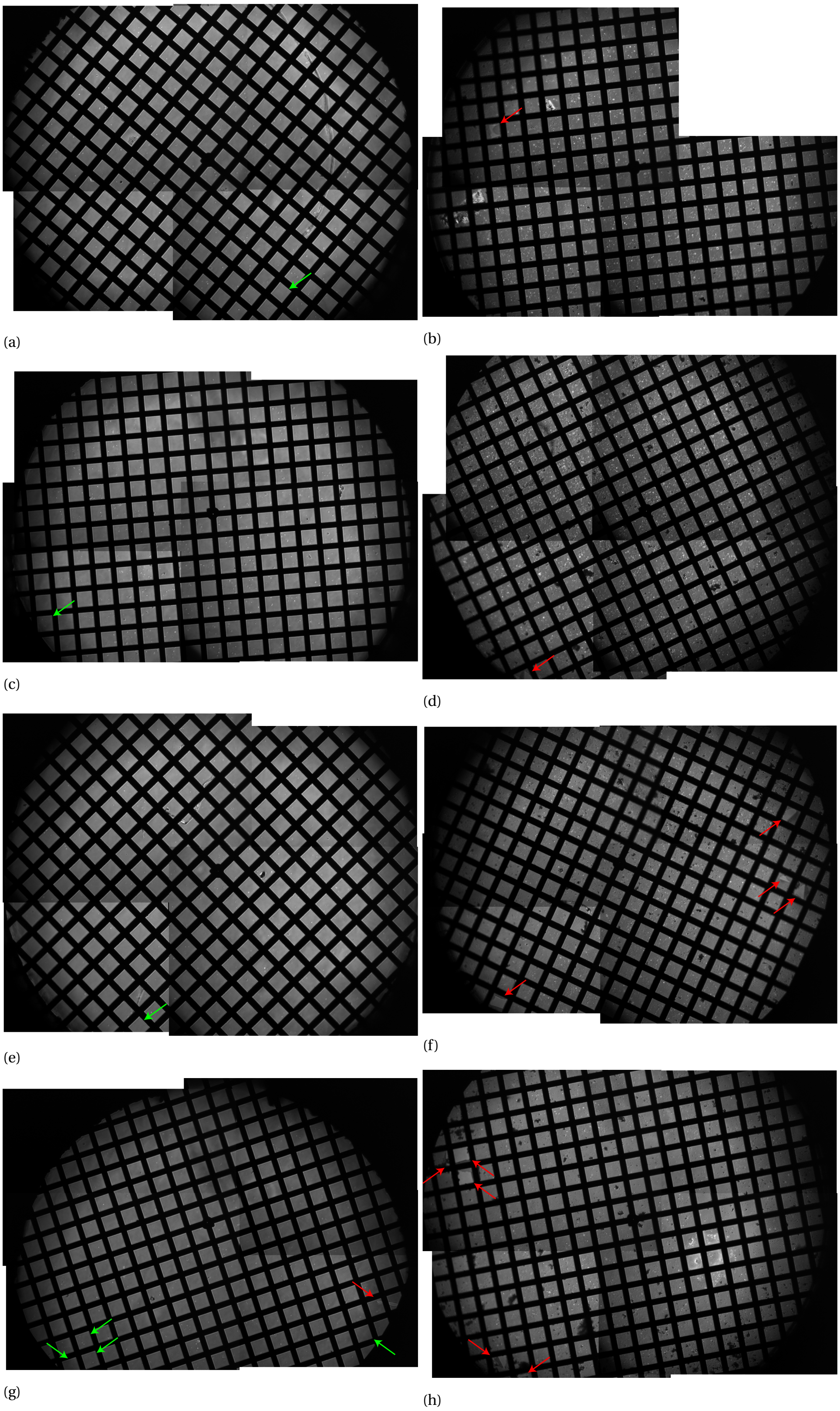

Figure 5.1: Microscope images of the TEM-grids before and after clipping using the old clipping pen, under cryogenic conditions. Red arrows are used to indicate holes on the TEM-grids that have a damaged carbon. Green arrows are used to indicate holes with an undamaged carbon layer before clipping that had a damaged carbon layer after clipping. (a) Grid c1 before clipping, (b) Grid c1 after clipping, (c) Grid c2 before clipping, (d) Grid c2 after clipping, (e) Grid c3 before clipping, (f) Grid c3 after clipping, (g) Grid c4 before clipping, and (h) Grid c4 after clipping.

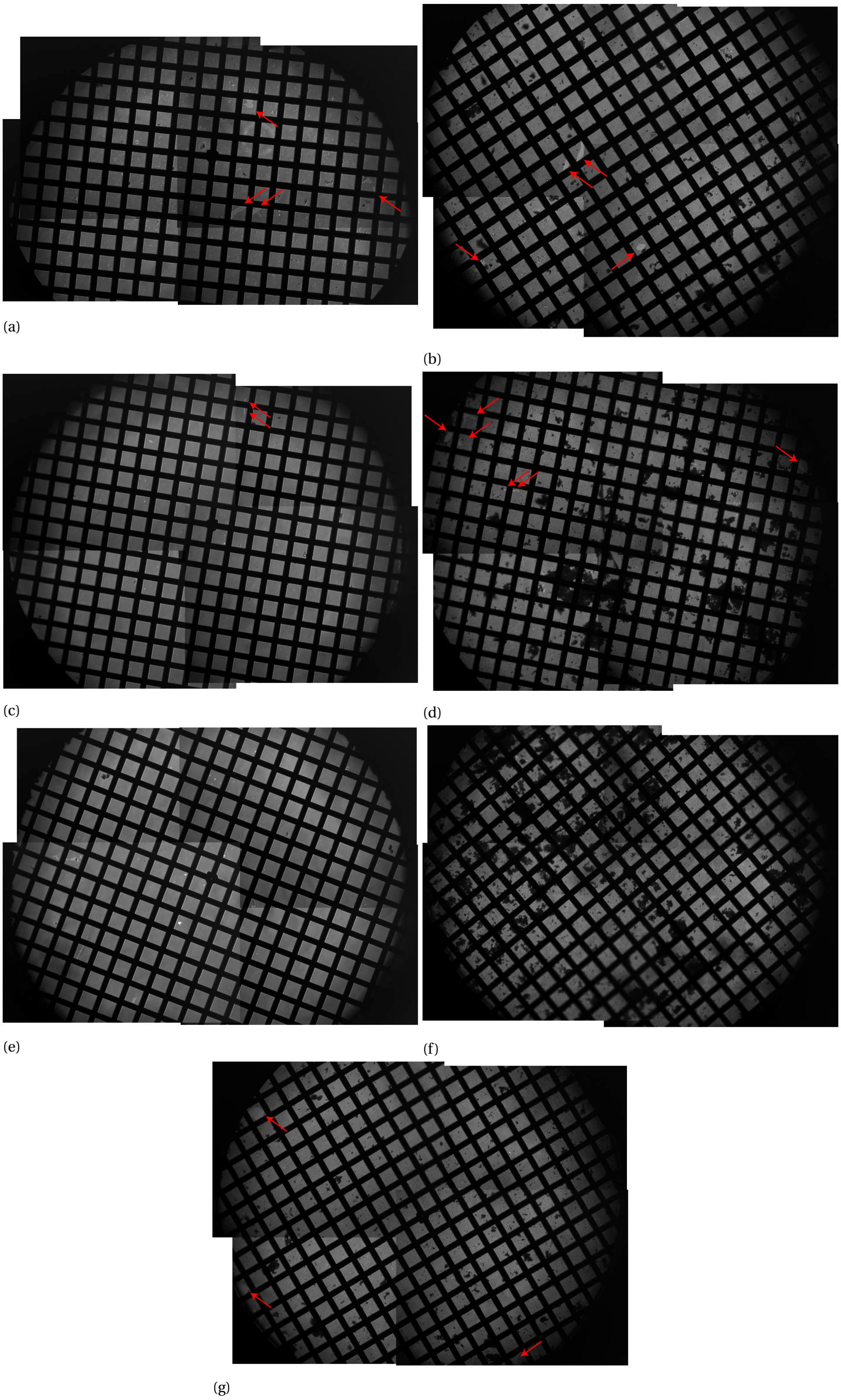

Figure 5.2: Microscope images of the TEM-grids before and after clipping using the new clipping pen, under cryogenic conditions. Red arrows are used to indicate holes on the TEM-grids that have a damaged carbon. (a) Grid C1 before clipping, (b) Grid C1 after clipping, (c) Grid C2 before clipping, (d) Grid C2 after clipping, (e) Grid C3 before clipping, (f) Grid C3 after clipping, and (g) Grid C4 after clipping.

The following relative values were calculated from these numbers: $\frac{DaUDb}{TUD}$, $\frac{TDa}{TUD}$, and $\frac{TpDC}{TUD}$. Here, TpDC stands for Total potentially Damaged by clipping and is defined as: $TpDC = DaUDb + DaUb$. Grid C3 was excluded because of the large amount of ice contamination in the image acquired after clipping. This grid was contaminated most, simply because it was imaged last. Figure 5.2f shows the image of the contaminated grid (Grid C3) after clipping. For Grid C4 the image acquired before clipping was lost, therefore some values were not calculated for this grid. For reference, Figure 5.3a, 5.3b, and 5.3c show closeups of a contaminated, damaged, and undamaged carbon layer, respectively.

For the grids clipped with the old clipping pen the mean relative values for $\frac{DaUDb}{TUD}$, $\frac{TDa}{TUD}$, and $\frac{TpDC}{TUD}$ were: 0.7%, 1.4%, and 1.3%, respectively. For the grids clipped with the new clipping pen the mean relative values for $\frac{DaUDb}{TUD}$, $\frac{TDa}{TUD}$, and $\frac{TpDC}{TUD}$ were: 0.0%, 1.9%, and 0.9%, respectively.

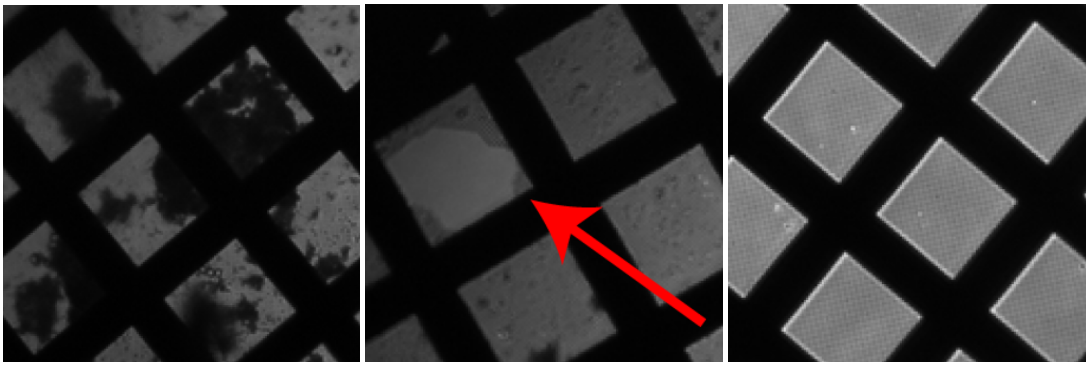

(a) (b) (c)

Figure 5.3: Closeups of a (a) contaminated, (b) damaged, and (c) undamaged carbon layer

5.2. Experiment 2: Automatic Autogrid cartridge orientation adjustment

Methods for experiment 2A and 2B are described in Subsection 4.3.3.

5.2.1. Experiment 2A: Comparison of the two algorithms

The means for all metrics (e.i. TP, FP, FN, P, R, and F1) for the four different approaches (e.i. ML, ML_{mc}, CHT, and CHT_{mc}) are given in Table 5.2.

Table 5.2: Mean values (± SD) for TP, FP, FN, P, R, and F1 for all four marker detection approaches.

	TP	FP	FN	P	R	F1
ML	2.0 (± 0.3)	1.4 (± 1.0)	0.1 (± 0.3)	0.63 (± 0.20)	0.95 (± 0.14)	0.74 (± 0.14)
ML_{mc}	2.0 (± 0.3)	0.7 (± 0.9)	0.1 (± 0.3)	0.81 (± 0.22)	0.96 (± 0.11)	0.86 (± 0.15)
CHT	1.5 (± 0.6)	1.4 (± 1.1)	0.6 (± 0.7)	0.58 (± 0.27)	0.75 (± 0.29)	0.62 (± 0.24)
CHT_{mc}	1.5 (± 0.6)	1.0 (± 1.0)	0.6 (± 0.7)	0.64 (± 0.30)	0.74 (± 0.32)	0.65 (± 0.27)

Histograms of the differences between the metrics were used to study the normality of the distribution of the differences. Distributions were assumed to be normal enough for using a t-test. Figure 5.4 shows two examples: Figure 5.4a shows the difference in F1-score between the CHT_{mc} approach and the ML_{mc} approach, and Figure 5.4b shows the difference in F1-score when the center of the Autogrid is not masked (CHT and ML).

The highest values for Precision, Recal, and F1-score (0.81, 0.96, and 0.86, respectively) were obtained with the ML approach where the center was masked (ML_{mc}). The values for precision (P) with the ML_{mc} approach were significantly ($p < 0.01$) higher with a large effect size ($r > 0.5$) [15] than the values for precision obtained for the ML and CHT approach ($r = 0.64$, $t = 10.59$, $p = 0.00$, and $r = 0.55$, $t = 8.37$, $p = 0.00$, respectively). The values for precision (P) with the ML_{mc} approach were significantly ($p < 0.01$) higher with a medium effect size ($r > 0.3$) [15] than the values for precision obtained with the CHT_{mc} approach ($r = 0.44$, $t = 6.22$, $p = 0.00$). The values for the recall (R) obtained with the ML_{mc} approach were significantly higher ($p < 0.01$), with a large effect size ($r > 0.5$), than the values for the recall obtained with the CHT, and CHT_{mc} approach

($r = 0.60$, $t = 9.52$, $p = 0.00$, and $r = 0.56$, $t = 8.74$, $p = 0.00$, respectively). A similar effect was found for the F1-score, where the F1-score obtained with the ML$_{mc}$ approach was significantly higher, with a large effect size ($r > 0.5$), than the F1-scores obtained with the ML, CHT, and CHT $_{mc}$ approach ($r = 0.66$, $t = 11.07$, $p = 0.00$, and $r = 0.68$, $t = 11.73$, $p = 0.00$, and $r = 0.60$, $t = 9.67$, $p = 0.00$, respectively). All values obtained from the statistical comparison using paired sample t-tests are given in Table 5.3.

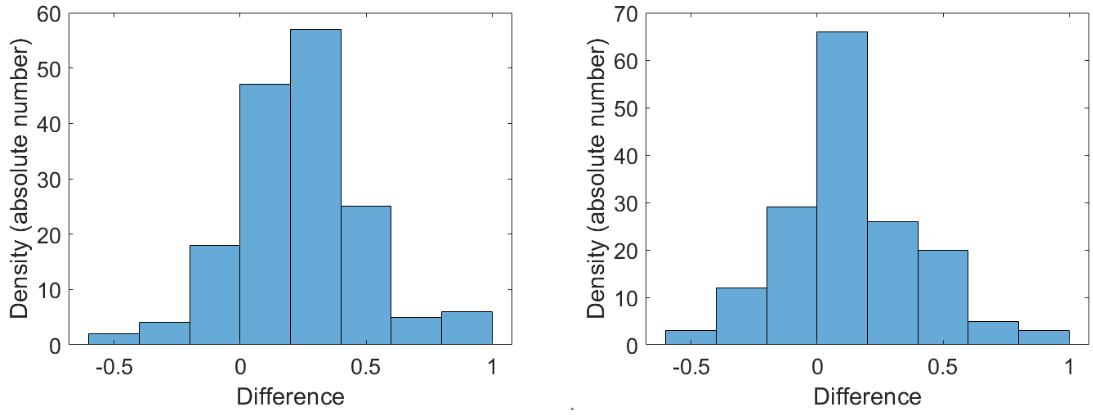

(a) (b)

Figure 5.4: A histogram of the distribution of: (a) the difference in F1-score between the CHT$_{mc}$ approach and the ML$_{mc}$ approach, and (b) the difference in F1-score when the center of the Autogrid is not masked (CHT and ML)

When comparing the precision score of the CHT approach to the precision score of the CHT$_{mc}$ approach, the CHT approach has a significantly higher precision score, but only a small ($r > 0.1$) effect size was found ($r = 0.16$, $t = 2.05$, $p = 0.04$). Masking the center of the Autogrid only affected the precision score, since no significant effects were found between the recall score of the ML and ML$_{mc}$ approach, and between the CHT and CHT$_{mc}$ approach. Without masking the center of the Autogrid, the ML approach, had a significantly higher, with a large ($r > 0.5$) and medium ($r > 0.3$) effect size respectively, ($p < 0.01$) recall ($r = 0.56$, $t = 8.63$, $p = 0.00$) and F1-score ($r = 0.38$, $t = 5.21$, $p = 0.00$) than the CHT approach. Similarly, the precision score for the ML approach was higher than the precision score for the CHT approach, although this effect was not significant ($r = 0.14$, $t = 1.78$, $p = 0.08$).

5.2.2. Experiment 2B: Proof of concept Automatic Autogrid orientation

The ML algorithm was selected for the proof of concept experiment in which the Autogrid was rotated automatically to the position in which the two markers of the Autogrid were on the left of the image. Here, the choice was made not to mask the center of the Autogrid. The rationale behind this choice was twofold: 1) The test-setup (shown in Figure) consisted of many 3D-printed parts. This occasionally caused the Autogrid holder to move it's position slightly. Although the same mask (with a fixed position) for the center of the Autogrid could be used for all 164 images used for comparing the two algorithms, and the test-setup was used to automatically retrieve these images, longer usage of the test-setup led to increased variations in the position of the Autogrid holder. Therefore, to ensure the markers would not be masked, the center was not masked. 2) If orientation of the Autogrid cartridge can be adjusted to the left orientation automatically without masking the center of the Autogrid, this will only improve further if the center of the Autogrid is masked in a more stable test-setup.

Figure 5.5 shows the orientation of the Autogrid with the detected markers at the starting position (Figure 5.5a, 5.5c, 5.5e, and 5.5g), and at the automatically obtained final position (Figure 5.5b, 5.5d, 5.5f, and 5.5h).

In all seven consecutive cases, the Autogrid was successfully rotated to an orientation in which the two markers are on the left side of the image. In four out of the seven cases, the markers were not detected perfectly in the starting position (Figure 5.5c: $TP = 1$, $FN = 1$, $FP = 1$, $P = 0.5$, $R = 0.5$, $F1 = 0.5$, Figure 5.5g: $TP = 1$, $FN = 1$, $FP = 1$, $P = 0.5$, $R = 0.5$, $F1 = 0.5$, Figure 5.6a: $TP = 1$, $FN = 1$, $FP = 1$, $P = 0.5$, $R = 0.5$, $F1 = 0.5$, and Figure 5.6c: $TP = 1$, $FN = 1$, $FP = 0$, $P = 1$, $R = 0.5$, $F1 = 0.67$). In two out of the seven cases, the markers were not detected perfectly in the ending position (Figure 5.5h: $TP = 1$, $FN = 1$, $FP = 1$, $P = 0.5$, $R = 0.5$, $F1 = 0.5$, and Figure 5.6d: $TP = 1$, $FN = 1$, $FP = 1$, $P = 0.5$, $R = 0.5$, $F1 = 0.5$).

5.3. Experiment 3: Automatic Autogrid handling

Methods for experiment 3 are described in 4.4.3. An Autogrid was retrieved from the Autogrid holder seven times. Figure 5.7 and Figure 5.8 show images of the Autogrid before (Figure 5.7a, 5.7c, 5.7e, 5.7g, 5.8a, 5.8c, and 5.8e) and after retrieval (Figure 5.7b, 5.7d, 5.7f, 5.7h, 5.8b, 5.8d, and 5.8f).

In five out of seven tests the orientation of the Autogrid did not change by retrieving the Autogrid. In two out of seven cases the orientation of the Autogrid changed slightly. In Figure 5.7h and Figure 5.8d the orientation of the Autogrid is changed compared to the orientation of the Autogrid in Figure 5.7g and Figure 5.8c, respectively.

Upon closer observations of movies obtained during the two tests, two different moments where the orientation was altered were identified. For test 4 (Figure 5.7g and 5.7h), the Autogrid rotated slightly when the gripper fingers closed around it. This can be observed by comparing the orientation of the Autogrid after the grippers were closed in Figure 5.9a, to the orientation of the Autogrid before closing the grippers in Figure 5.7g. For test 6 (Figure 5.8c and 5.8d) the Autogrid rotated after the grippers were closed, while the Autogrid was retrieved from the Autogrid holder. Figure 5.9b shows the Autogrid after closing the gripper fingers, and Figure 5.9c shows the Autogrid after retrieving it from the Autogrid holder.

Table 5.3: Values obtained from the paired samples t-tests between the four marker detection approaches. In each sub-table values for the effect size (r), t-value, and p-value, for one of the six metrics (e.i. TP, FP, FN, P, R, and F1), are reported

(a) Statistical values obtained when comparing the obtained values for TP, for the four marker detection approaches.

	ML	ML_{mc}	CHT	CHT_{mc}
ML				
ML_{mc}	0.12 ($t = 1.51$, $p = 0.13$)			
CHT	0.56 ($t = 8.65$, $p = 0.00$)	0.61 ($t = 9.84$, $p = 0.00$)		
CHT_{mc}	0.56 ($t = 8.65 =$, $p = 0.00$)	0.61 ($t = 9.79$, $p = 0.00$)	0.03 ($t = 0.43$, $p = 0.67$)	

(b) Statistical values obtained when comparing the obtained values for FP, for the four marker detection approaches.

	ML	ML_{mc}	CHT	CHT_{mc}
ML				
ML_{mc}	0.65 ($t = 10.87$, $p = 0.00$)			
CHT	0.05 ($t = 0.65$, $p = 0.52$)	0.42 ($t = 5.91$, $p = 0.00$)		
CHT_{mc}	0.29 ($t = 3.90$, $p = 0.00$)	0.20 ($t = 2.61$, $p = 0.01$)	0.37 ($t = 5.09$, $p = 0.00$)	

(c) Statistical values obtained when comparing the obtained values for FN, for the four marker detection approaches.

	ML	ML_{mc}	CHT	CHT_{mc}
ML				
ML_{mc}	0.10 ($t = 1.34$, $p = 0.18$)			
CHT	0.55 ($t = 8.43$, $p = 0.00$)	0.58 ($t = 8.99$, $p = 0.00$)		
CHT_{mc}	0.53 ($t = 8.01$, $p = 0.00$)	0.56 ($t = 8.54$, $p = 0.00$)	0.02 ($t = 0.26$, $p = 0.80$)	

(d) Statistical values obtained when comparing the obtained values for P, for the four marker detection approaches.

	ML	ML_{mc}	CHT	CHT_{mc}
ML				
ML_{mc}	0.64 ($t = 10.59$, $p = 0.00$)			
CHT	0.14 ($t = 1.78$, $p = 0.08$)	0.55 ($t = 8.37$, $p = 0.00$)		
CHT_{mc}	0.01 ($t = 0.18$, $p = 0.86$)	0.44 ($t = 6.22$, $p = 0.00$)	0.16 ($t = 2.05$, $p = 0.04$)	

(e) Statistical values obtained when comparing the obtained values for R, for the four marker detection approaches.

	ML	ML_{mc}	CHT	CHT_{mc}
ML				
ML_{mc}	0.13 ($t = 1.63$, $p = 0.10$)			
CHT	0.56 ($t = 8.63$, $p = 0.00$)	0.60 ($t = 9.52$, $p = 0.00$)		
CHT_{mc}	0.53 ($t = 8.01$, $p = 0.00$)	0.56 ($t = 8.74$, $p = 0.00$)	0.02 ($t = 0.29$, $p = 0.77$)	

(f) Statistical values obtained when comparing the obtained values for F1, for the four marker detection approaches.

	ML	ML_{mc}	CHT	CHT_{mc}
ML				
ML_{mc}	0.66 ($t = 11.07$, $p = 0.00$)			
CHT	0.38 ($t = 5.21$, $p = 0.00$)	0.68 ($t = 11.73$, $p = 0.00$)		
CHT_{mc}	0.27 ($t = 3.62$, $p = 0.00$)	0.60 ($t = 9.67$, $p = 0.00$)	0.10 ($t = 1.34$, $p = 0.18$)	

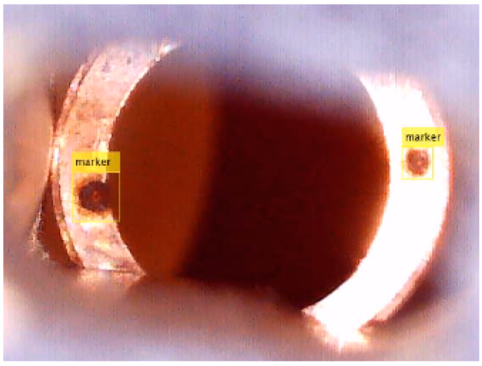

(a)

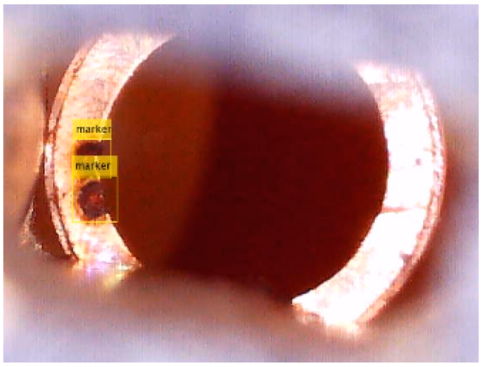

(b)

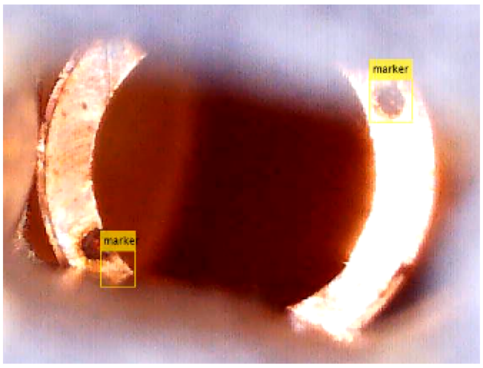

(c)

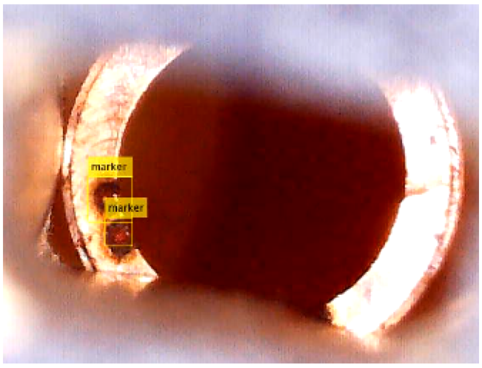

(d)

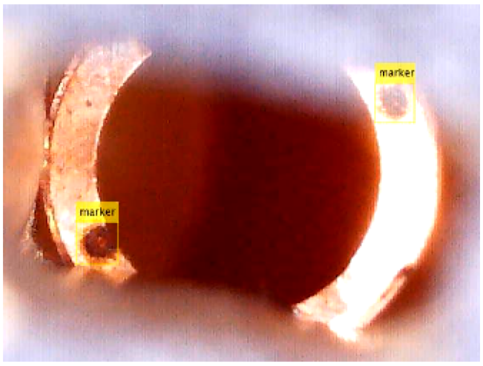

(e)

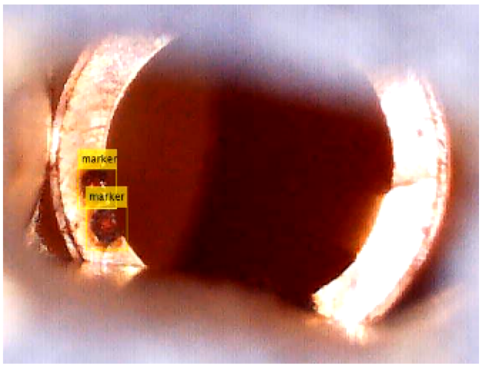

(f)

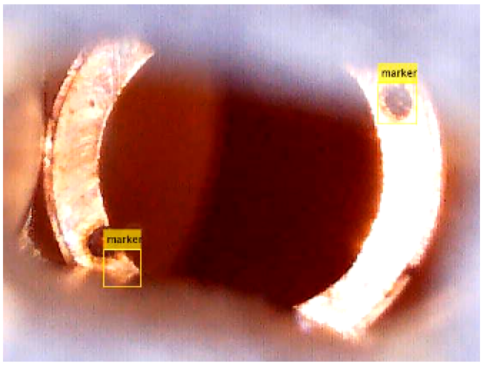

(g)

(h)

Figure 5.5: Seven proof of concept tests were performed where the Autogrid cartridge was automatically rotated to a position where the markers are on the left. Images show the first and final image of these tests with the detected markers indicated with the yellow squares: (a) image at the start of Autogrid orientation test 1, (b) image at the end of Autogrid orientation test 1, (c) image at the start of Autogrid orientation test 2, (d) image at the end of Autogrid orientation test 2, (e) image at the start of Autogrid orientation test 3, (f) image at the end of Autogrid orientation test 3, (g) image at the start of Autogrid orientation test 4, and (h) image at the end of Autogrid orientation test 4

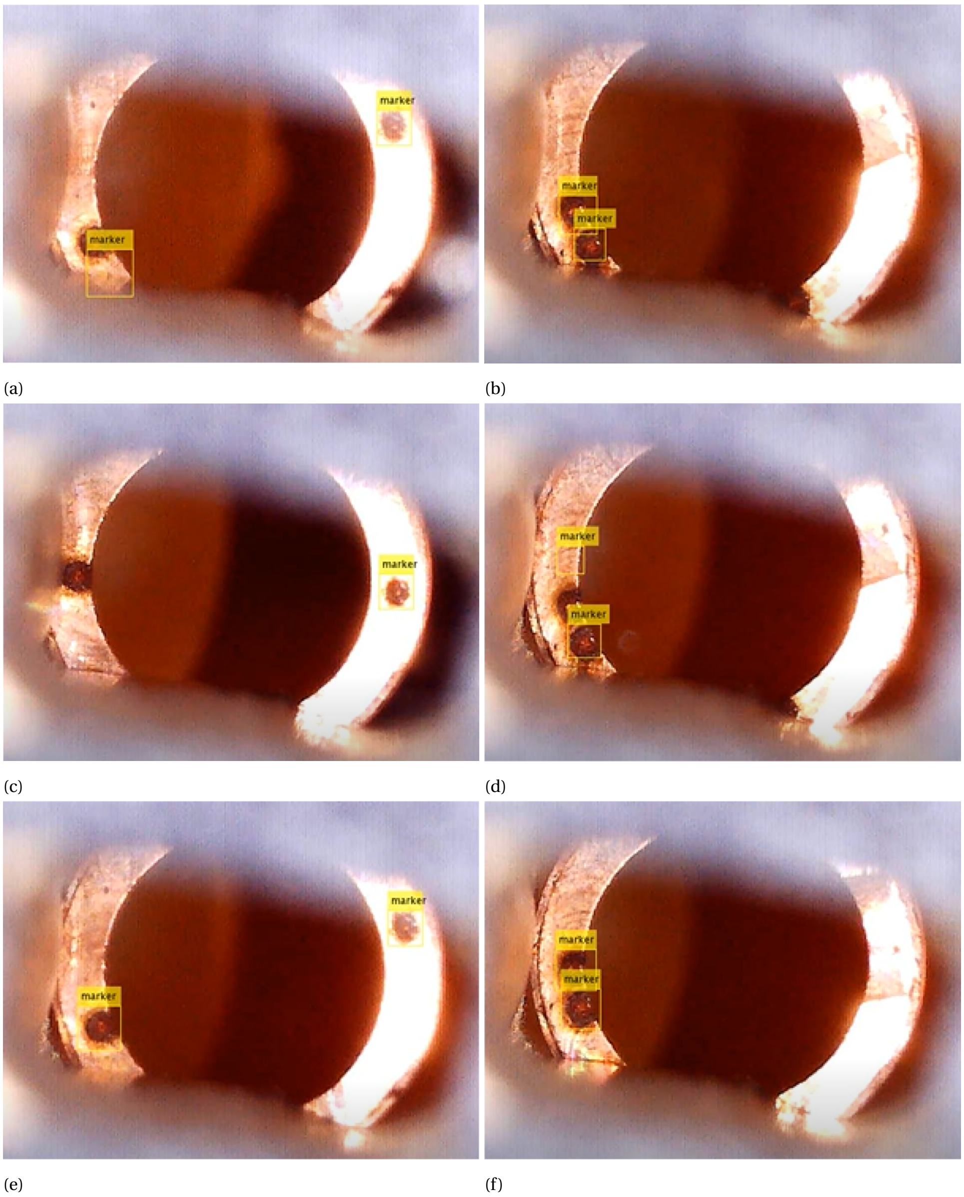

(a) (b) (c) (d) (e) (f)

Figure 5.6: Seven proof of concept tests were performed where the Autogrid cartridge was automatically rotated to a position where the markers are on the left. Images show the first and final image of these tests with the detected markers indicated with the yellow squares: (a) image at the start of Autogrid orientation test 5, (b) image at the end of Autogrid orientation test 5, (c) image at the start of Autogrid orientation test 6, (d) image at the end of Autogrid orientation test 6, (e) image at the start of Autogrid orientation test 7, and (f) image at the end of Autogrid orientation test 7.

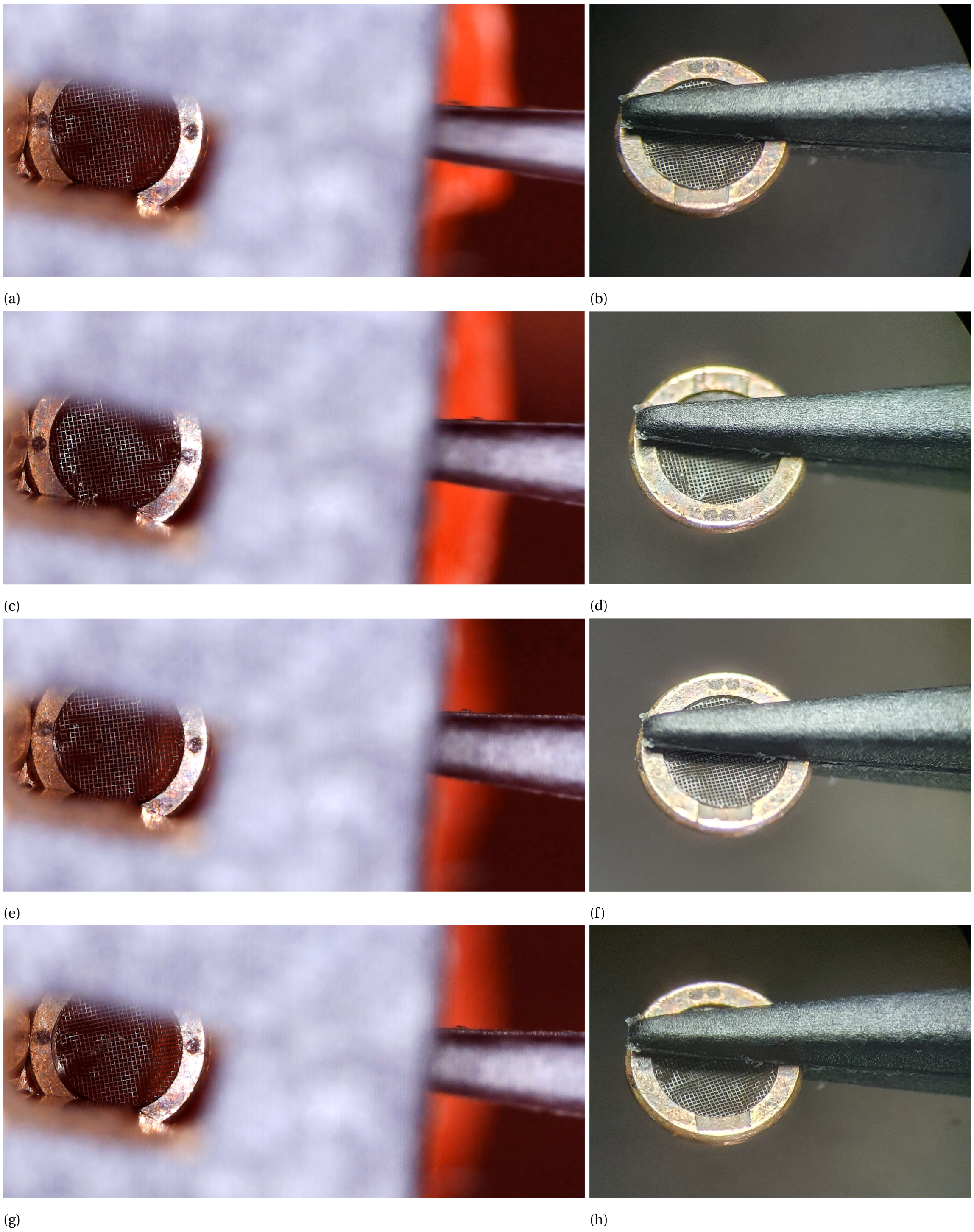

Figure 5.7: Images of the markers on the bottom of the Autogrid before and after retrieval with: (a) Test 1 before retrieval, (b) Test 1 after retrieval, (c) Test 2 before retrieval, (d) Test 2 after retrieval, (e) Test 3 before retrieval, (f) Test 3 after retrieval, (g) Test 4 before retrieval, and (h) Test 4 after retrieval

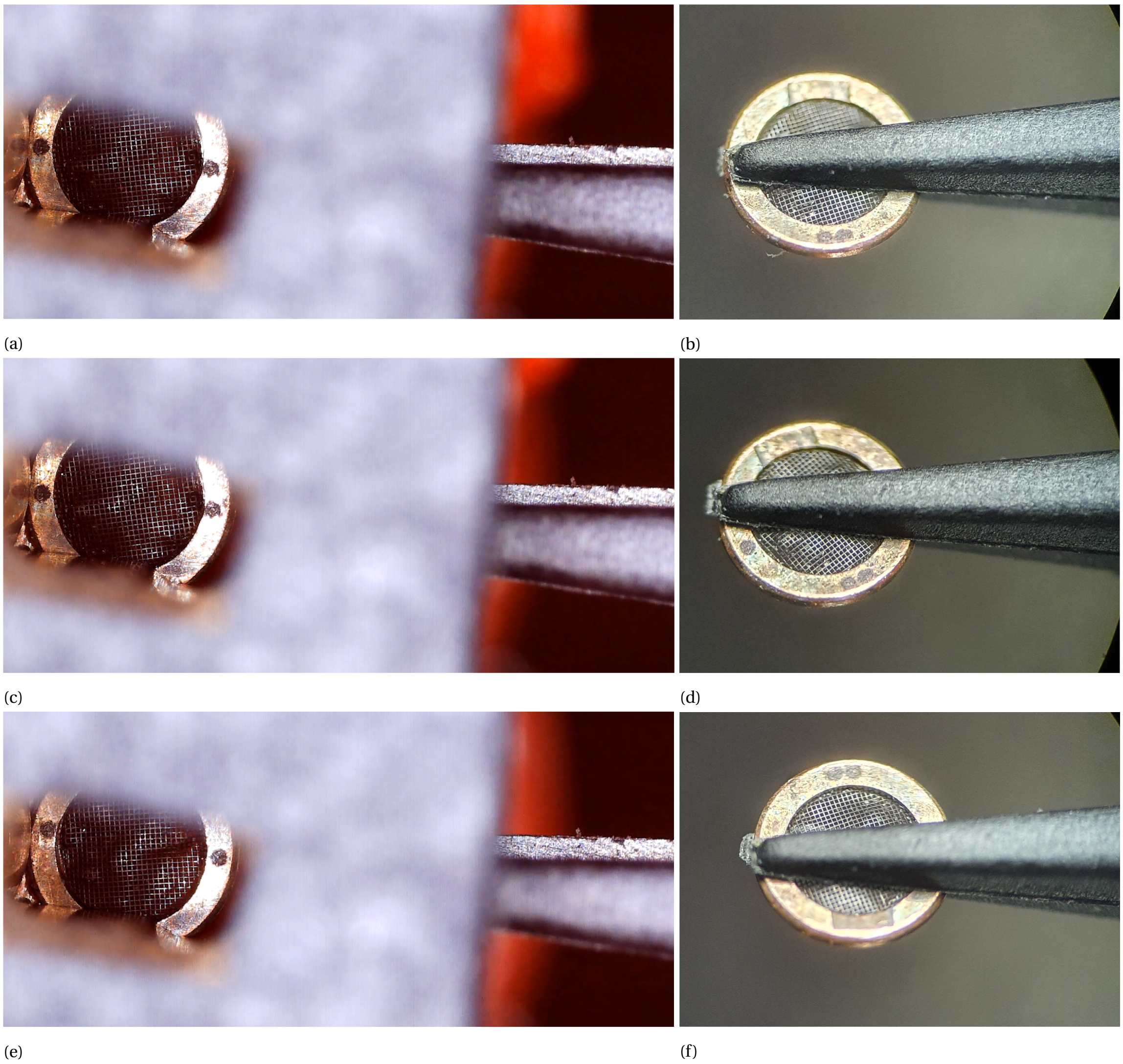

Figure 5.8: Images of the markers on the bottom of the Autogrid before and after retrieval with: (a) Test 5 before retrieval, (b) Test 5 after retrieval, (c) Test 6 before retrieval, (d) Test 6 after retrieval, (e) Test 7 before retrieval, and (f) Test 7 after retrieval

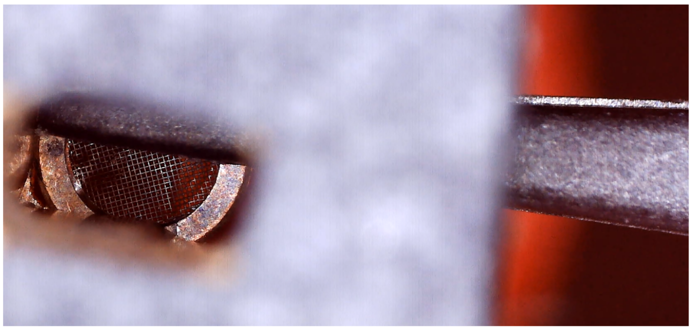

(a)

(b)

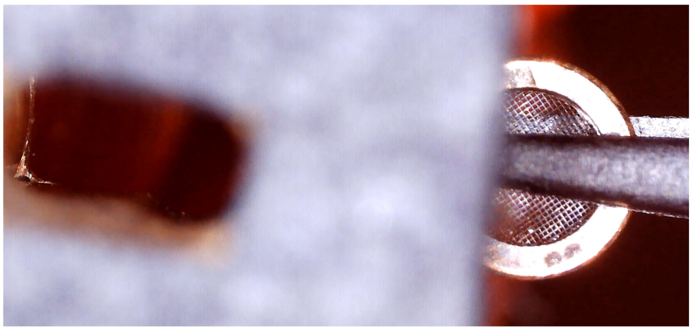

(c)

Figure 5.9: Images of the bottom of the Autogrid (a) after closing the gripper fingers in test 4, (b) after closing the gripper fingers in test 6, and (c) after retrieving the Autogrid from the Autogrid holder in test 6.

5.4. Experiment 4: Automatic TEM-grid handling

Methods for experiment 4A and 4B are described in Subsection 4.5.3.

5.4.1. Experiment 4A: Quantification of damage on TEM-grids while automatically handling TEM-grids

During alignment for testing the Automatic TEM-grid placement, the five copper grids were potentially damaged before placing them in the Autogrid cartridge. An accident happened in which a screw driver was placed on the optical bread board causing the low-mass TEM-grids to jump from the grid box. This could also contaminate the TEM-grids with dust particles clouding the vision on acquired images. Although the TEM-grids showed preliminary damage and dust particles due to this accident, a comparison between the damaged parts before and after placing the TEM-grids could still provide valuable information. The two golden grids were not damaged in this accident and will therefore be described first.

Golden TEM-grids

The first golden TEM-grid (GT1) was automatically retrieved from the grid-box and placed in the Autogrid cartridge successfully. Thereafter the Autogrid cartridge with TEM-grid inside was manually removed from the Autogrid holder and imaged under the light microscope. Figure 5.10a shows the TEM-grid before placing it in the Autogrid cartridge, and Figure 5.10b shows the TEM-grid after placing it in the Autogrid cartridge. Before inserting the TEM-grid in the Autogrid cartridge there was almost no damage present. The red arrow in Figure 5.10a indicates the only position in which the TEM-grid was damaged. After inserting the TEM-grid in the Autogrid cartridge, the TEM-grid was damaged at two locations. One of these locations corresponds to the location that was damaged before inserting the TEM-grid. The other location corresponds to where the gripper fingers were used to hold the TEM-grid (black arrow in Figure 5.10a). Similarly, the second golden grid was successfully retrieved from the grid-box and placed in the Autogrid cartridge. Thereafter, manually retrieving the Autogrid cartridge with TEM-grid inside from the Autogrid holder was not successful. The tweezers used to retrieve the Autogrid cartridge with TEM-grid inside, acted on the TEM-grid and the Autogrid cartridge. By not only acting on the Autogrid cartridge, the TEM-grid was bent.

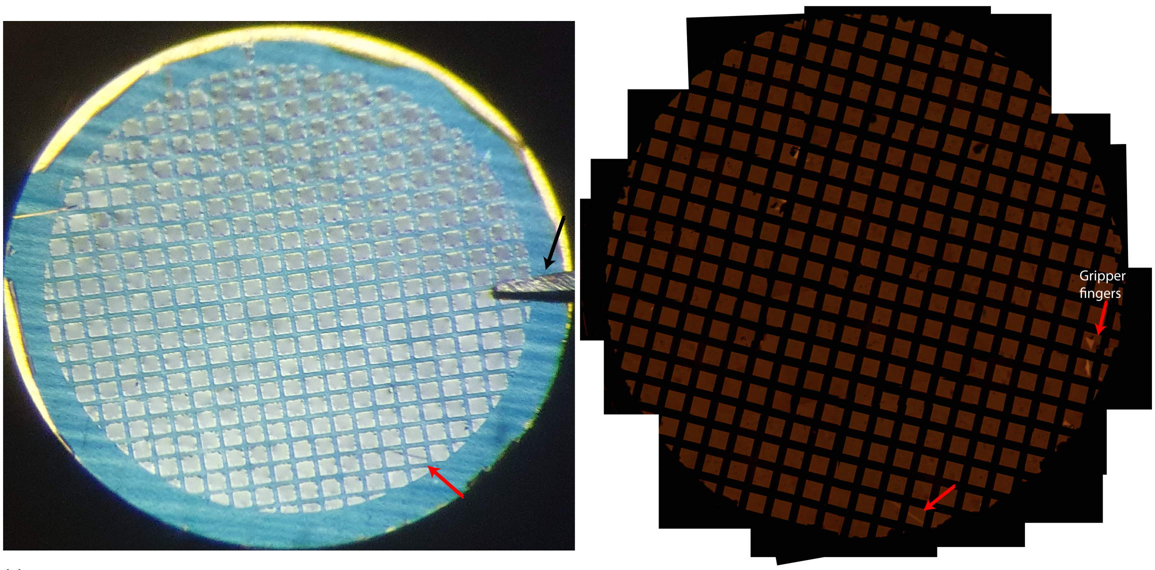

(a) (b)

Figure 5.10: An image of grid GT1 before (a) and after (b) automatically placing it in the Autogrid cartridge. Red arrows indicate identified damage of the carbon layer. The tip of the gripper fingers is indicated with a black arrow. Damage caused by the gripper fingers is indicated with the text: 'Gripper fingers'.

Figure 5.11a shows the TEM-grid before placing it in the Autogrid cartridge with damage at only one location (red arrow). Figure 5.11b shows the TEM-grid after the unsuccessful manual retrieval of the Autogrid cartridge with TEM-grid inside with a red arrow to the bent part of the TEM-grid. Figure 5.12 shows a magnification of the bent part of the TEM-grid.

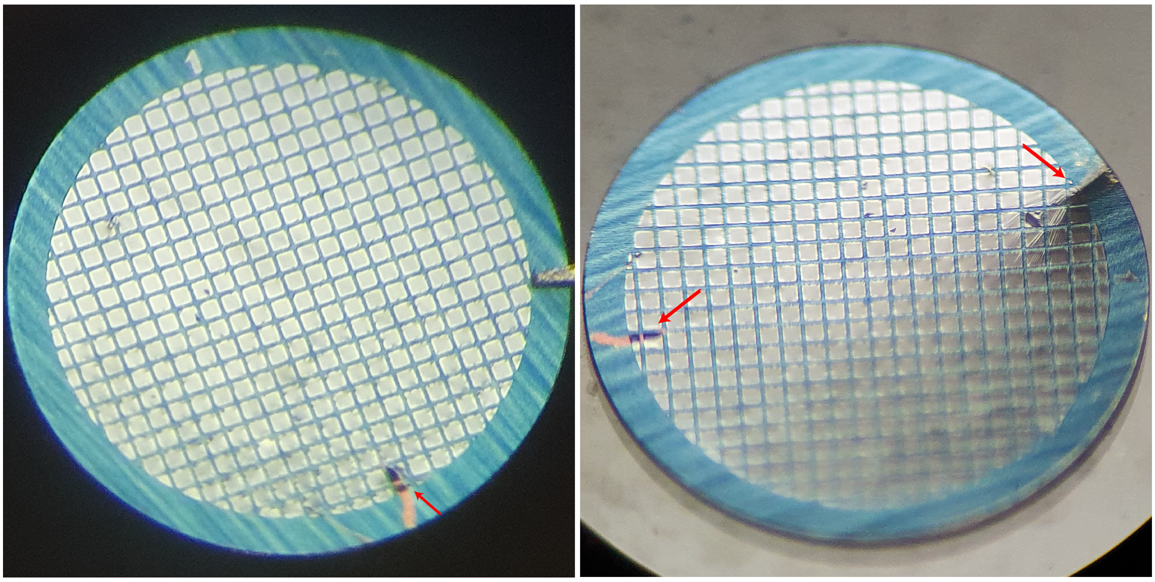

(a) (b)

Figure 5.11: Two images of the golden TEM-grid that was damaged during retrieval of the Autogrid cartridge from the Autogrid holder after automatically placing the TEM-grid in the Autogrid cartridge. Damaged locations are indicated with a red arrow. (a) The golden TEM-grid before placing it in the Autogrid cartridge, and (b) The golden TEM-grid after it was damaged during retrieval.

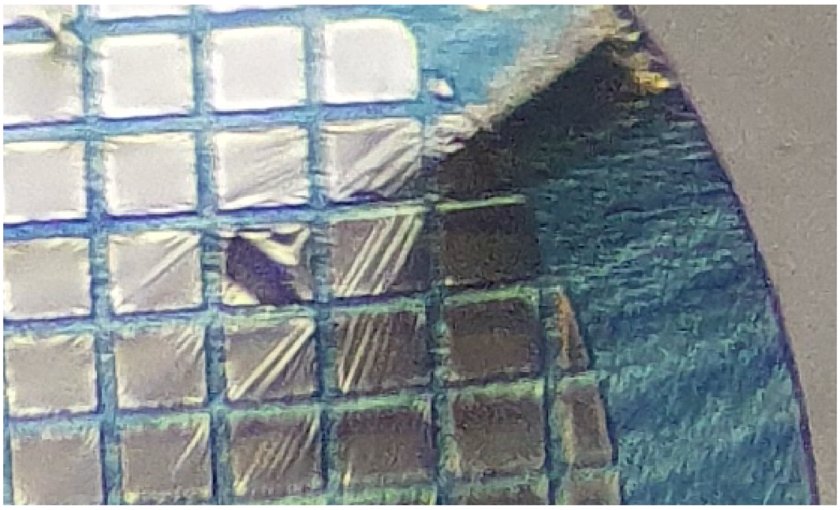

Figure 5.12: Image of the bent part of the golden TEM-grid that was damaged during retrieval after placement in the Autogrid cartridge.

Copper TEM-grids

With two out of five copper TEM-grids, the copper TEM-grid was damaged during manual retrieval of the Autogrid cartridge with the TEM-grid inside. These two cases were therefore excluded from the analysis. Figure 5.13 shows a region where the carbon layer was damaged during manual retrieval of the Autogrid cartridge with the TEM-grid inside. Here, red arrows indicate the damaged parts of the carbon layer.

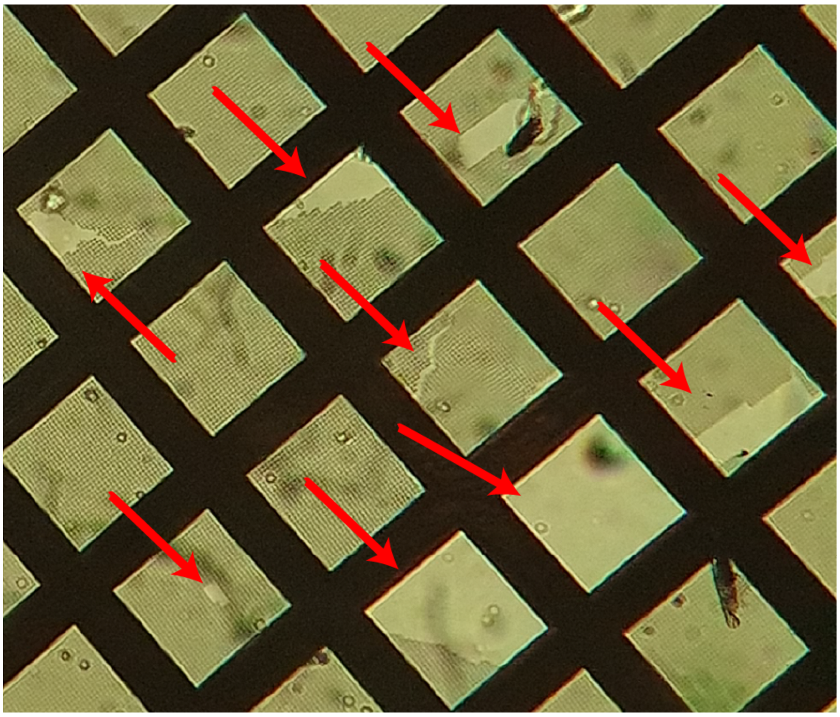

Figure 5.13: Image of a region on a TEM-grid where the carbon layer was damaged during manual retrieval of the Autogrid cartridge with the TEM-grid inside. Red arrows indicate the damaged parts of the carbon layer.

For one of the Copper TEM-grids, the images obtained after retrieving the Autogrid cartridge with TEM-grid inside were of too poor quality to quantify damage of the TEM-grid. This case was therefore excluded.

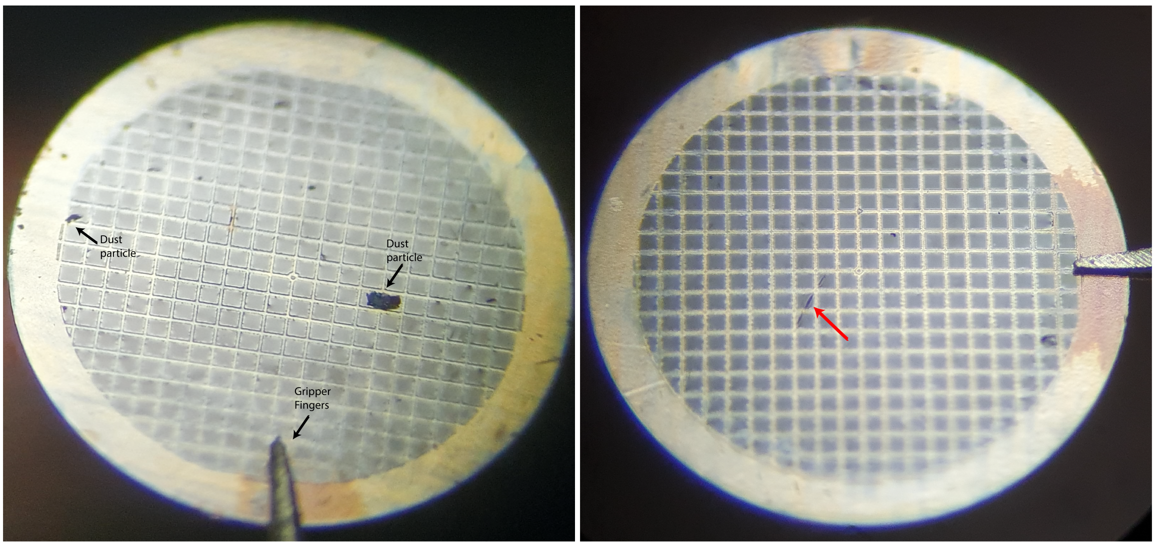

(a) (b)

Figure 5.14: Images of the two TEM-grids made of copper before placing them in the Autogrid cartridge with: (a) TEM-grid CT1, and (b) TEM-grid CT2.

For the two remaining copper TEM-grids, images that were obtained before inserting the TEM-grid in the Autogrid cartridge are given in Figure 5.14. Images of the TEM-grid made of copper labelled as CT1, before and after placement in the Autogrid cartridge are given in Figure 5.14a and Figure 5.15a, respectively. Images of the TEM-grid made of copper labelled as CT2, before and after placement in the Autogrid cartridge are given in Figure 5.14b and Figure 5.15b, respectively.

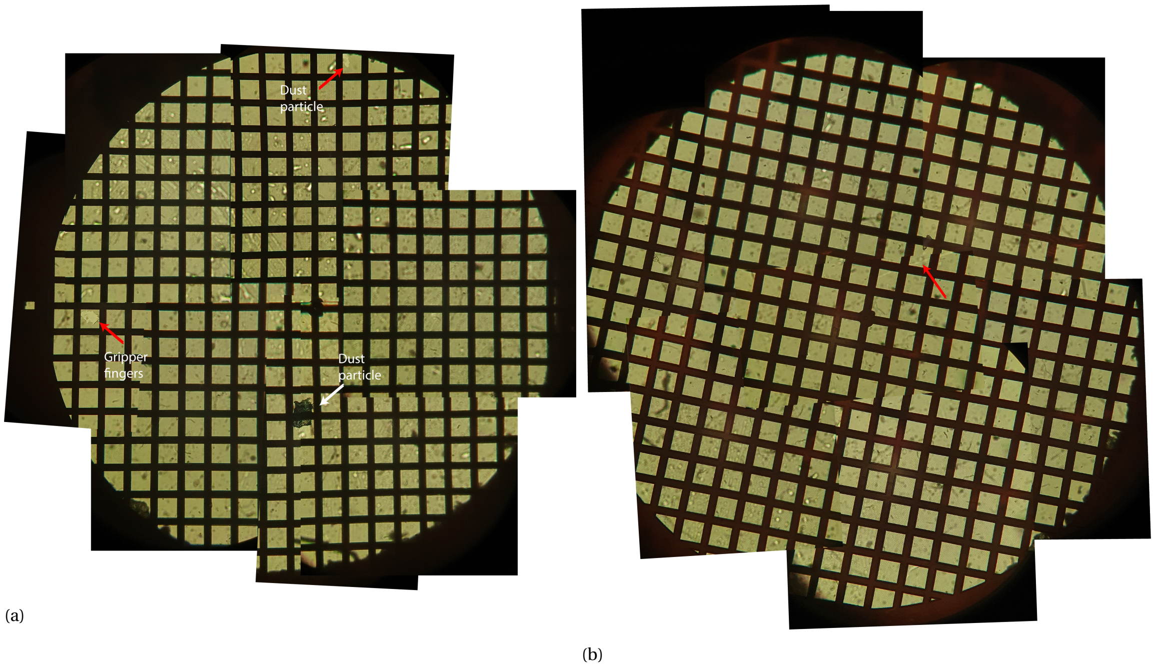

Figure 5.15: Images of the two copper TEM-grids after placing them in the Autogrid cartridge with: (a) TEM-grid CT1, and (b) TEM-grid CT2.

One of the two damaged locations on CT1 (indicated with the red arrow in Figure 5.15a) was at the same location as one of the two dust particles was before placing the TEM-grid. This is indicated with the black arrow in Figure 5.14a. The other damaged location was at the location where the gripper fingers were used to handle the TEM-grid, indicated with the black arrow in Figure 5.15a. Another relatively large dust particle could potentially have damaged the carbon layer, although this was not well visible due to the size of the dust particle. This relatively larger dust particle is indicated with a white arrow in Figure 5.15a, and with a black arrow in Figure 5.14a.

On the other copper TEM-grid (CT2) only one damaged location was identified, which was present before and after placement in the Autogrid cartridge. This location is indicated with the red arrow in Figure 5.14b and in Figure 5.15b.

5.4.2. Experiment 4B: Mapping the orientation of TEM-grids to the Autogrid cartridge

Five TEM-grids were retrieved from the grid-holder, and the orientation of the TEM-grid with respect to the gripper fingers was observed under the microscope. These five tests were numbered as placement test (PT) 1-5. Figures 5.16c, 5.16f, 5.16i, 5.16l, and 5.16o, show the TEM-grid an tweezers before placement (PT1, PT2, PT3, PT4, and PT5, respectively). Figures 5.16a, 5.16d, 5.16g, 5.16j, and 5.16m, show the empty Autogrid cartridge before placing the TEM-grids (PT1, PT2, PT3, PT4, and PT5, respectively). Figures 5.16b, 5.16e, 5.16h, 5.16k, and 5.16n show the Bottom of the Autogrid cartridge with the TEM-grid placed inside (PT1, PT2, PT3, PT4, and PT5, respectively). For each of these five TEM-grids the orientation of the TEM-grid with respect to the gripper fingers was mapped 10 times to the empty Autogrid cartridge. This mapped orientation was compared to the orientation of the TEM-grid with respect to the Autogrid cartridge after placing the TEM-grid.

Table 5.4 shows mean values (± SD) for the angle difference (in degrees) between the mapped orientation of the TEM-grid with respect to the Autogrid cartridge and the obtained orientation of the TEM-grid with respect to the Autogrid cartridge. The mean difference for all tests with mapping the orientation of the TEM-grid with respect to the gripper fingers was 4.9°(± 2.4°). For all placement tests (PT) the SD within one test

(PT) is smaller than the mean SD for all tests. Table 5.5 shows the angle difference between the mapped orientation of the TEM-grid with respect to the Autogrid cartridge when allowing for negative values. When allowing for negative values, the mean difference and standard deviation of the difference over all 50 tests are -1.1 and 5.4, respectively.

Table 5.4: Mean values (± SD) for the absolute angle difference (in degrees) between the mapped orientation of the TEM-grid with respect to the Autogrid cartridge and the obtained orientation of the TEM-grid with respect to the Autogrid cartridge, with PT = placement test.

PT 1	PT 2	PT 3	PT 4	PT 5	Mean
6.4°(± 1.4°)	2.1°(± 1.0°)	7.3°(± 0.7°)	5.9°(± 1.7°)	2.8°(± 0.8°)	4.9°(± 2.4°)

Table 5.5: Mean values (± SD) for the angle difference (in degrees) between the mapped orientation of the TEM-grid with respect to the Autogrid cartridge and the obtained orientation of the TEM-grid with respect to the Autogrid cartridge when allowing for negative differences, with PT = placement test.

PT 1	PT 2	PT 3	PT 4	PT 5	Mean
-6.4°(± 1.4°)	2.1°(± 1.0°)	7.3°(± 0.7°)	-5.9°(± 1.7°)	-2.8°(± 0.8°)	-1.1°(± 5.4°)

Figure 5.17 shows one example where the orientation of the TEM-grid with respect to the gripper fingers is mapped to the Autogrid cartridge and compared to the obtained orientation. For this specific example, the difference between the mapped orientation and the obtained orientation was 2.3°. Figure 5.17a shows the identified orientation of the TEM-grid with respect to the gripper fingers. Figure 5.17b shows how this orientation is mapped to the empty Autogrid cartridge. Figure 5.17c shows the mapped orientation on the Autogrid cartridge after the TEM-grid is placed. Figure 5.17d shows the orientation that was identified based on the TEM-grid and Autogrid cartridge after placement, used for comparison.

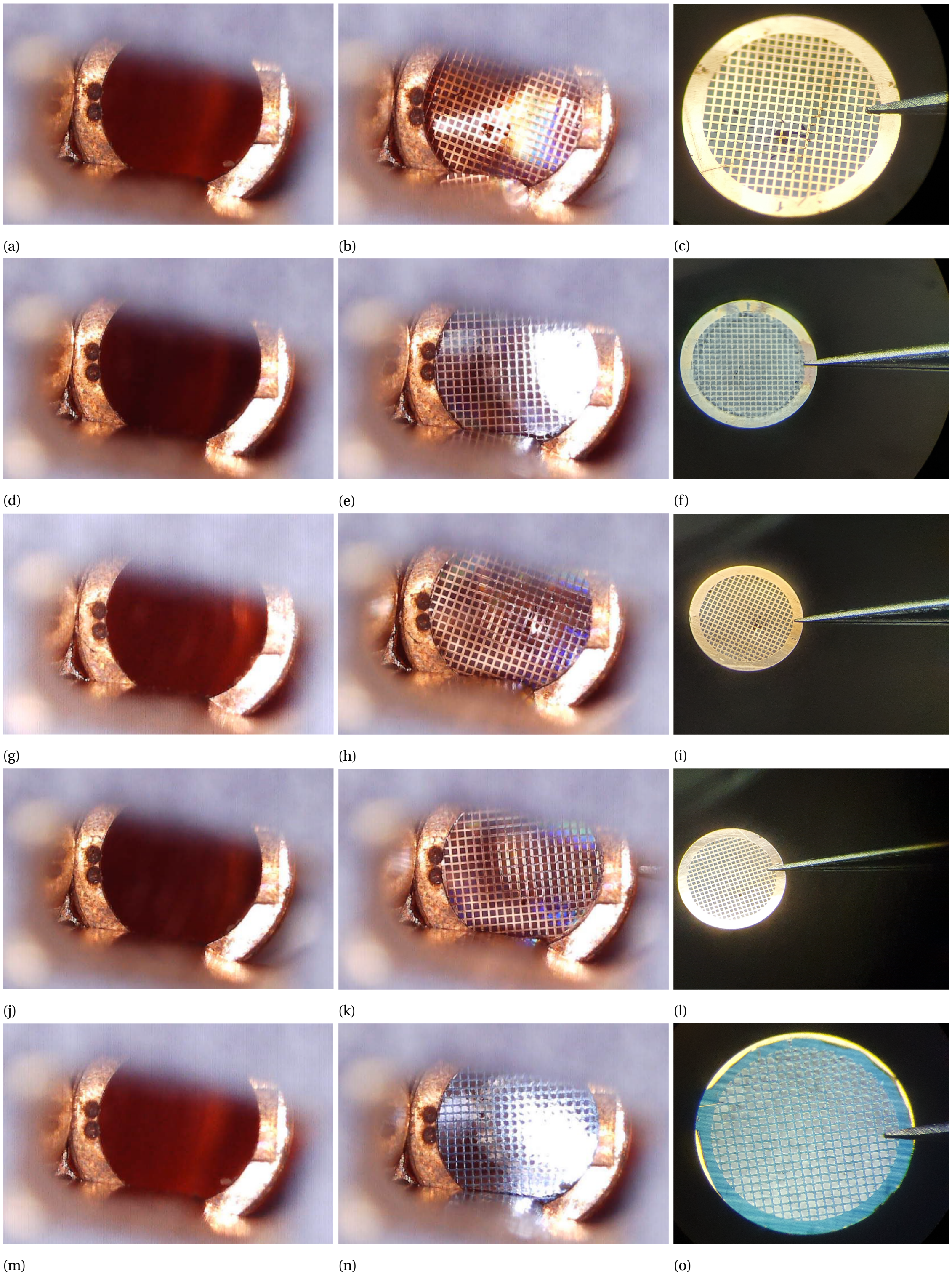

Figure 5.16: The empty Autogrid cartridge before placing the TEM-grid, the Autogrid cartridge with TEM-grid inside after placement, and the gripper fingers and TEM-grid before placement, for PT1, PT2, PT3, PT4, and PT5, with: (a), (b), and (c); PT1, (d), (e), and (f); PT2, (g), (h), and (i); PT3, (j), (k), and (l); PT4, (m), (n), and (o); PT5.

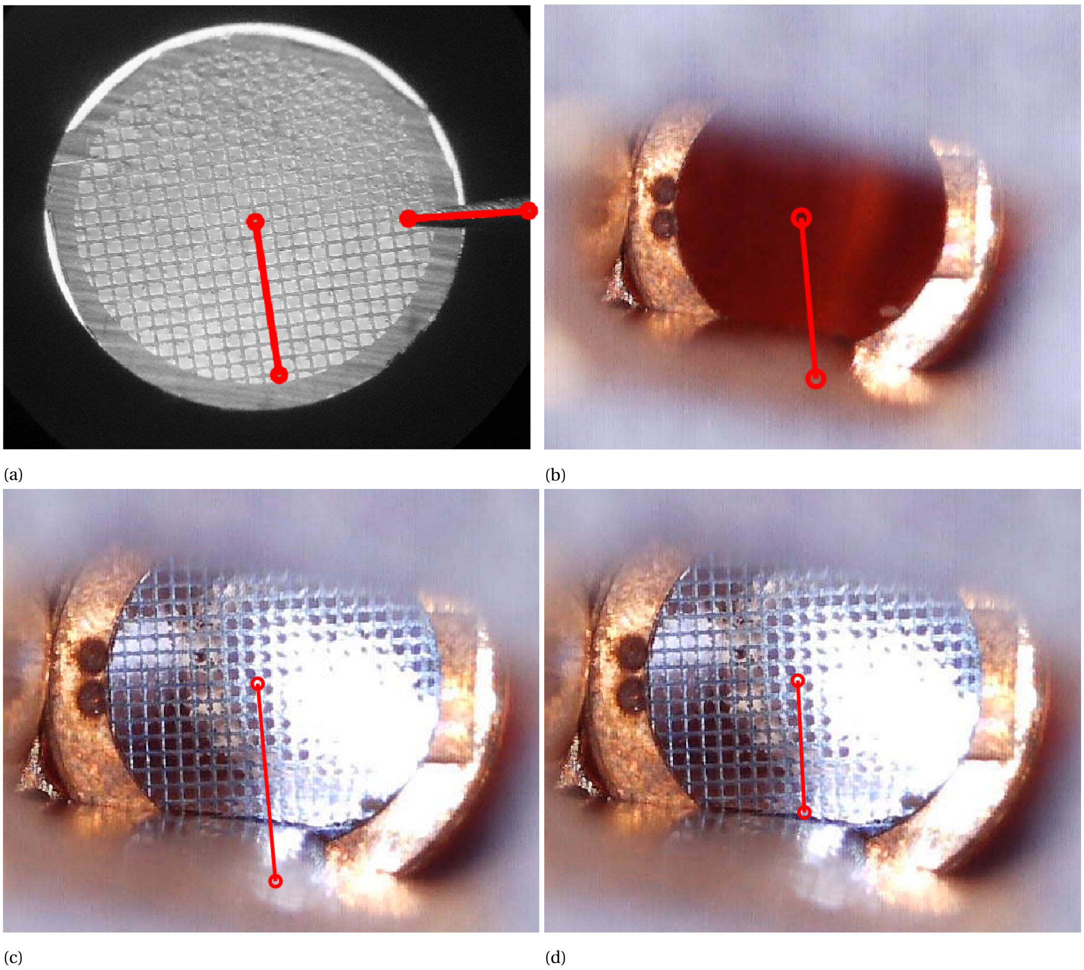

(a) (b) (c) (d)

Figure 5.17: An example where the orientation of the TEM-grid with respect to the gripper fingers is mapped to the Autogrid cartridge and compared to the obtained orientation. For this specific example, the difference between the mapped orientation and the obtained orientation was 2.3°.

6
Discussion

In this chapter, the results of the four experiments will be discussed. Subsequently a general discussion and recommendations for improving the cryo-ET workflow are given.

6.1. Experiment 1: New clipping pen

For this experiment, the damage on the TEM-grids was quantified by calculating the amount of damaged holes with respect to the amount of undamaged holes. The calculated value for $\frac{TpDC}{TUD}$ was used to estimate the amount of grid holes that could potentially be damaged during clipping. Some of the grid holes that were damaged after clipping were not visible on images of the TEM-grids before clipping. It was uncertain if these holes contained damage before clipping. Therefore, these locations could have been damaged during the clipping process. The calculated values for $\frac{DaUDb}{TUD}$ provide information on the amount of grid holes that were definitely damaged during the clipping process, as the damaged grid holes included in this variable were not damaged before clipping. The damage was not necessarily induced during c-clip insertion, but could have been induced in any of the four clipping steps (c_1, c_2, c_3, or c_4). Compared to the the old clipping pen, when comparing the total amount of grid holes damaged during the clipping process and the total amount of grid holes that could have potentially been damaged during the clipping process, the new clipping pen performed slightly better on both metrics ($\frac{DaUDb}{TUD}$ is 0.7% and 0.0%, and $\frac{TpDC}{TUD}$ is 1.3% and 0.9%, for the old and new clipping pen, respectively). The difference between the two clipping pens was however small (<1%). Also, statistical tests were not performed, since the sample size was small.

Overall, the damage on all TEM-grids clipped in experiment 1 was a lot lower than anticipated. One of the reasons for this could be that the experienced user performing the clipping procedure had further mastered clipping of the Autogrid. The time between the first encounter with the experienced user and testing of the new c-clip insertion tool was approximately five months. Although there were some problems still at the first encounter, five extra months of working with handling of TEM-grids could still have caused a slight improvement of the skills required for handling these grids. This slight improvement could have been the difference between some damage on the TEM-grids, and almost no damage on the TEM-grids. Following this line of reasoning, the only cause of damage on TEM-grids during clipping, is human error. If this were to be true, automating the procedure could increase the clipping yield near to 100%. One other explanation for the low amount of damage on the tested TEM-grids is that there were no samples present on the grids. As proposed in subsection 3.3.2 small imperfections on the carbon layer, might cause local stress concentrations, thereby leading to damage of the carbon layer. Following the same line of reasoning, the samples themselves, although they are relatively small, might induce damage on the TEM-grids. In experiment 4A (see subsection 5.4.1) a small dust particle induced damage on the carbon layer. If such damage can be caused by a dust particle, applying samples to be imaged on the TEM-grid could probably also induce damage. Damage induced by samples should however already be visible before clipping the Autogrid, and would therefore not be classified as damage caused by clipping the Autogrid. Microdamage caused by applying samples on the TEM-grid before clipping, might however still induce damaged locations during clipping. Therefore, although the low amount of damage obtained while clipping with both the new and old clipping pen suggests that automation could increase the clipping yield to near 100%, it is yet uncertain if such a high yield could also be obtained when there are samples present on the TEM-grid. Ideally, an automated solution for c-clip insertion would be tested on a large amount of TEM-grids with various samples on them. In practice such a study will be hard to achieve because TEM-grids and samples can be very costly. Also, using golden grids in such an experiment would provide the most valuable information, as golden grids are more fragile than those made of copper. The problem here is that such golden TEM-grids are much more expensive than the TEM-grids made of copper.

A new potential risk is introduced when using the force-limiting mechanism described in this report. If the frictional forces on the part of the pen that presses the c-clip in the Autogrid cartridge are large enough for the part to get stuck, this can cause storage of energy in the spring that is used to limit the force. Once the force exerted by this spring becomes larger than the static friction force acting on the part of the pen that presses the c-clip down, this part will rapidly move downwards (since the kinetic friction coefficient is often smaller than the static friction coefficient). This rapid motion can then cause damage on the TEM-grid.

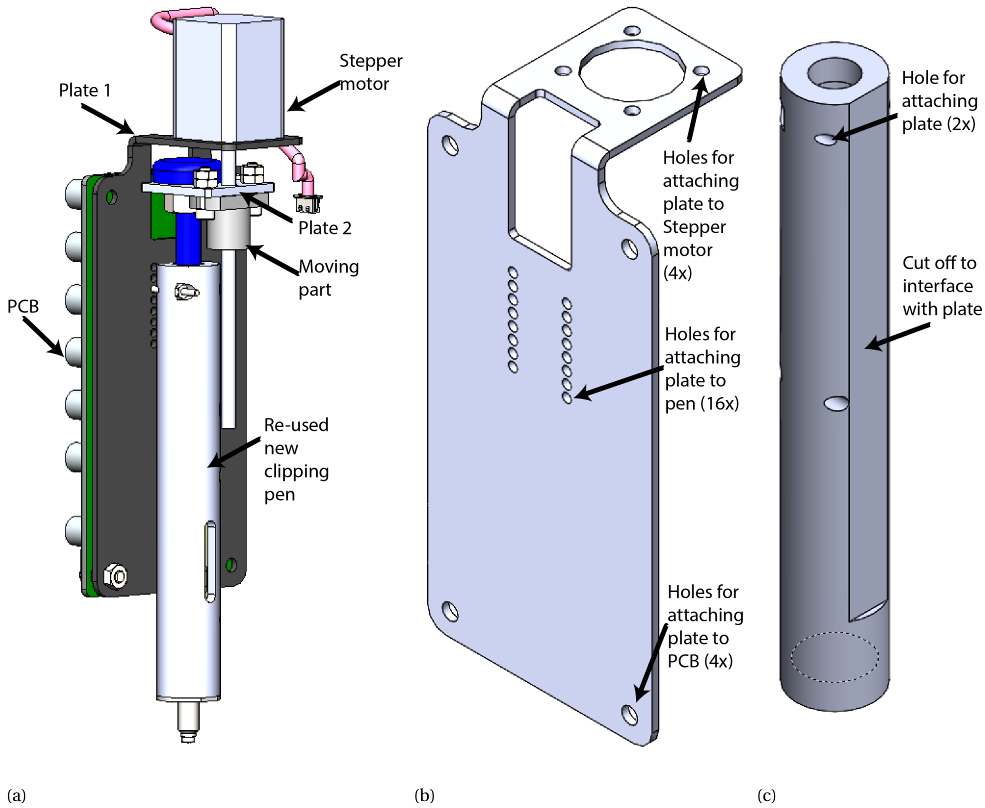

Figure 6.1: CAD model of an example of a design where already available parts are re-used to test automated c-clip insertion. (a) Assembly of the automatic c-clip insertion tool, (b) Features of the plate used to attach the stepper motor and PCB to the clipping pen, and (c) the modified outer part of the new clipping pen.

Recommendations for a final automated solution, are to use the force-limiting mechanism and air gaps that are included in the new clipping pen. Based on the experimental results presented in this report, the new clipping pen performs equally to or better than the old clipping pen. Moreover, including these two features in an automated solution will not require much extra effort. In a final solution a stiffer spring could be used in the force limiting mechanism (or the lid could be tightened accordingly). This would reduce the risk of rapid movement caused by energy storage in the spring, as the spring force is more likely to overcome the frictional forces in the pen. If position control is then used for c-clip insertion, any errors in the position will only cause a small amount of force to be applied on the c-clip. An example of how already available and used components can be re-used for testing the automated c-clip insertion is provided in Figure 6.1 Using such a solution would only require manufacturing two new plates for attaching a stepper motor and a printed circuit board (PCB) to the already existing new clipping pen. The outer part of the new clipping pen would have to be modified slightly by adding two holes and cutting of one side to interface with the plate attached to the PCB. By using the combination of a stepper motor with the force-limiting mechanism, simple feedforward control of the position of the stepper motor can be used. Any imperfections in positioning the cylinder that is moving the c-clip down, will not exert a high amount of force on the c-clip and thereby on the TEM-grid. Redesigning parts would be desirable for implementation into a final commercial product. This final commercial product should also contain multiple pretensioned c-clips to automate the entire process (e.g. a stapler-like mechanism).

6.2. Experiment 2: Automatic Autogrid orientation

6.2.1. Experiment 2A

In experiment 2A, the ML approach performed better than the CHT approach for all three metrics (precision, recall, and F1-score). Masking the center of the Autogrid had a positive effect on the precision score, and not on the recall score. Since the recall score represents how well the algorithm can find all objects it should detect, it should not be affected by masking the Autogrid center. Masking the Autogrid center will make it less likely that the algorithm detects markers in the masked region. This explains the increase of the precision score by masking the center of the Autogrid. The found positive effect of masking the Autogrid center on the F1-score was mainly due to the positive effect on the precision score. Based on the obtained results, the best approach for detecting the markers on the bottom of the Autogrid was to use a ML approach while masking the center of the Autogrid. With this approach a precision, recall, and F1-score of 0.81, 0.96, and 0.86 were respectively obtained.

Although the obtained precision and recall was high enough to perform the proof of concept experiment (experiment 2B), marker detection was not yet perfect. The machine learning algorithm that was used for detecting the region of interest in the images successfully detected the region of interest in all images (corresponding to $P = 1$, $R = 1$, and $F1 = 1$). There are multiple possible explanations why such high precision and recall values were not obtained for the machine learning algorithm detecting the markers on the bottom of the Autogrid.

The region of interest has many distinct features that can be used by the machine learning algorithm for detection. Figure 6.2 shows one example of an image where the region of interest was detected. Outside of this region of interest there are no parts of the image that are similar to the region of interest. When using the machine learning algorithm to detect the markers on the bottom of the Autogrid, the features that are to be detected are less distinct. Many sections of the image might resemble a black marker in one way or another.

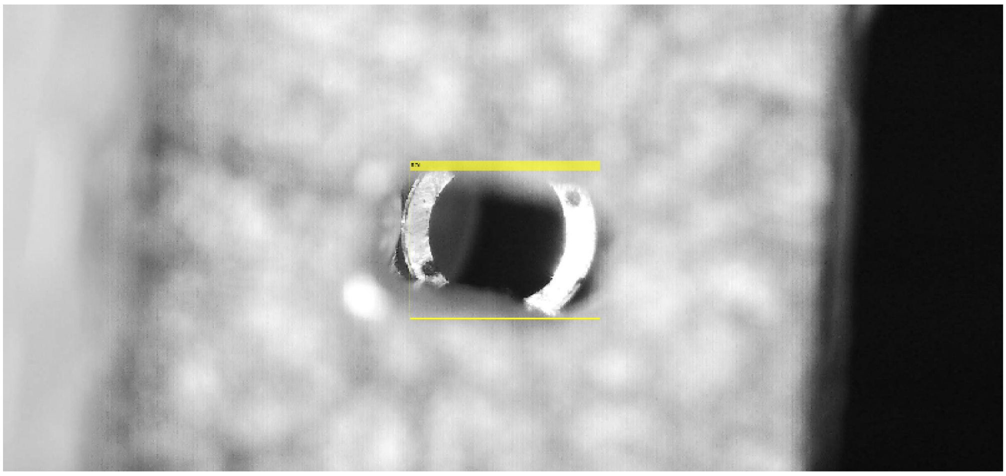

Figure 6.2: Image of the detected region of interest. Here, the region of interest is indicated with the yellow square.

One other possible explanation to why marker detection was not perfect is related to the way markers were selected to train the algorithm. Because of the shape of the hole at the bottom of the Autogrid, not the entire Autogrid cartridge is visible while rotating it. Therefore, in some orientations the markers at the bottom of the Autogrid cartridge were only half visible. For this project, the choice was made to include markers that were half visible in the training data. Using this approach led to being able to detect markers that were only half visible such as the detected markers in Figure 6.3b. The disadvantage of using this approach is that the marker detection algorithm was trained to detect certain features present in the edge of the hole in the Autogrid holder. Figure 6.3a shows an example where the algorithm wrongly detects a marker at the edge of the hole in the Autogrid holder.

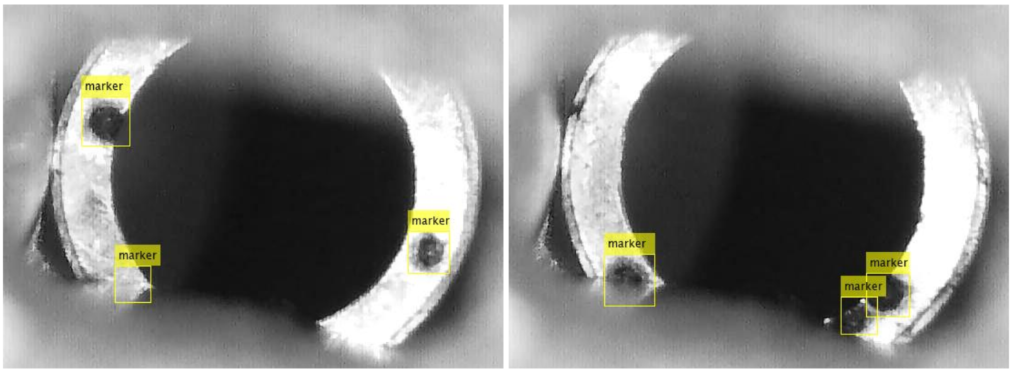

(a) (b)

Figure 6.3: (a) Example where a marker is mistakenly detected at the edge of the hole through the Autogrid holder. (b) Example where a marker that is only half visible, is detected by the machine learning algorithm.

Using the approach where half visible markers were included therefore therefore led to a larger amount of false positively detected markers. For future use of the approach for marker detection as proposed in this project, recommendations are to not include markers that are only half visible. This will probably lead to markers not being detected when they are half visible. It will however also decrease the number of false positively detected markers. Depending on the definition that is used for false negatives, this does not necessarily increase the number of false negatives. For the current project, markers that were half visible but were not detected, were classified as false negative. When choosing to not include markers that are half visible as markers that should be detected, the total amount of false negatives could stay the same or could even improve.

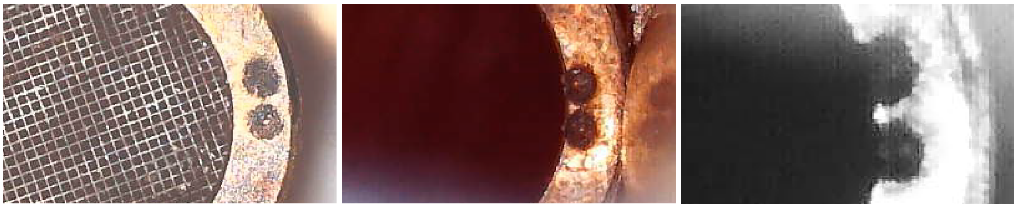

(a) (b) (c)

Figure 6.4: The bottom of three different Autogrid cartridges. This figure is used to illustrate the different sizes and shapes of markers at the bottom of different Autogrid cartridges.

Another thing to consider is the amount of different Autogrid cartridges that were used to train the algorithm. Figure 6.4 shows the bottom side of three of the Autogrid cartridges that were used to train the machine learning algorithm (in total four Autogrid cartridges were used to train the machine learning algorithm). On all three images the shape of the markers is slightly different. Providing as many shapes as possible to train the machine learning algorithm will help with improving training of the algorithm for detecting markers. The problem here, is that Autogrid cartridges that have markers at the bottom are expensive and not easy to come by. Such cartridges can only be purchased by research institutions that are in possession of a TEM with an autoloader system that is capable of handling these Autogrids. For future implementation, recommendations are to use as many different Autogrid cartridges as possible for training the machine learning algorithm.

Lastly, the images of the bottom of the Autogrid cartridge were obtained in a test setup next to a window. Therefore, the lighting conditions on the bottom of the Autogrid cartridge varied on different images. Using constant lighting conditions for training the algorithm and detecting the markers could further improve detection of the markers on the bottom of the Autogrid cartridge.

6.2.2. Experiment 2B

Although the marker detection algorithm was not yet perfect, in a proof of concept experiment, the Autogrid cartridge was successfully rotated to a specified orientation seven consecutive times. That this succeeded seven consecutive times could have been pure chance was not deemed very likely. With the current approach markers could wrongly be detected on the edge of the hole through the Autogrid holder (as described above in subsection 6.2.1). This was also the case at the end of one of the seven proof of concept experiments (see

Image 5.5h). For this specific case, this did not result in unsuccessful automatic orientation adjustment.

After proof of concept experiment 2B, some of the parts used to interface between the rotating part of the Autogrid holder and the stepper motor began to wear. This caused the Autogrid holder to move when rotating the stepper motor. Although the current setup was sufficient for this proof of concept experiment, in future experiments the Autogrid holder should be adjusted to integrate the stepper motor. A more stable test setup together with the improvements to the machine learning algorithm mentioned above can further improve the results. The algorithm could also be adjusted to include other orientations than the orientation where two markers are on the left, or the orientation of the Autogrid could be set in degrees instead of specifying a specific orientation.

6.3. Experiment 3: Automatic Autogrid retrieval

That the Autogrid orientation was retained in five out of seven tests in experiment 3 is a promising results. Some improvements could however be made.

In one of the cases where the orientation of the Autogrid was not retained after retrieval, the Autogrid orientation changed while closing the gripper fingers. The orientation of the Autogrid probably changed because the ends of the gripper fingers that were in contact with the Autogrid were not parallel. In future experiments, this can be prevented by using a different type of tweezers in combination with the currently selected gripper fingers. Special types of tweezers exist for handling Autogrids that are shaped differently than regular tweezers. An example of such tweezers is shown in the first clipping step in Figure 2.6. Using these specific tweezers would however require redesigning the Autogrid holder to allow for retrieving the Autogrid. Another possibility is to use a different kind of gripper fingers that do have a parallel surface interfacing with the Autogrid. This would either require using a different gripper, as the surfaces of the MEGP 25 are not parallel, or a smart design of gripper fingers. One could for example design gripper fingers with an internal spring mechanism that ensures a certain amount of force always acts on two sides of the Autogrid. Alternatively, seesaw-like gripper fingers could be designed such that they apply the same amount of force on both sides of the Autogrid cartridge.

In the other case where the orientation of the Autogrid cartridge was not retained, the change in orientation was probably caused by misalignment while retrieving the Autogrid. The setup that was used for the seven experiments mainly consisted of 3D printed parts. After longer testing, certain 3D printed parts began to wear. This probably contributed to a slight misalignment during retrieval of the Autogrid. Moreover, alignment of the Meca500 was done by eye and was therefore not as good as it could be. For future use in a commercial product, recommendations are to perform all clipping steps in a stable environment and to use a microscope for alignment. For example, microscopes such as the one present on the ultramicrotome for experiments 3 and 4, can be moved and used over a large surface. Such a microscope could be used for the alignment that is required when setting up all equipment that is used in the new proposed (automated) clipping procedure.

6.4. Experiment 4: Automatic TEM-grid placement

6.4.1. Experiment 4A

In experiment 4A, TEM-grids were successfully placed in the Autogrid cartridge using the selected gripper fingers. After placing the TEM-grids in the Autogrid cartridge, they were manually retrieved using a pair of tweezers. This manual handling step after TEM-grid placement, proved to be more difficult than anticipated. In this manual retrieval step, one golden TEM-grid and two TEM-grids made of copper were damaged and were therefore excluded. Although exclusion of these TEM-grids led to acquiring less information in this experiment, it is a good example showing that TEM-grids will easily get damaged if they are handled by less experienced users.

One of the three TEM-grids that were not damaged during manual retrieval was not damaged at all when placing it in the Autogrid cartridge. The other two grids, were damaged only at the location where the tips of the gripper fingers interacted with the TEM-grid. For these two grids, the gripper fingers were placed too far over the rim of the TEM-grid (see Figure 5.14a and Figure 5.10a). With the TEM-grid that was not damaged, gripper fingers were placed only on the rim of the TEM-grid (see Figure 5.14b). Although this is only a case study, these results suggest that when the gripper fingers only act on the rim of the TEM-grid, the TEM-grids can be placed in an Autogrid cartridge without inducing damage.

To retrieve the TEM-grids, the gripper fingers were aligned by eye. As the rim of the TEM-grids that were used is very small (<0.4 mm [50]) aligning the tips of the gripper fingers with the rim of the TEM-grid is difficult. Alignment is even more difficult when TEM-grids are retrieved from a grid-box as it was done in experiment 4A. In such a grid box the TEM-grid is completely inside the box. Therefore, it was not visible if the gripper fingers were aligned well before gripping. Even if it were possible to observe the TEM-grid and gripper fingers within the grid box, the TEM-grid has a lot of space inside grid box. This allows the TEM-grid to be in multiple positions inside the grid box, making it hard to predict where the tips of the gripper fingers would end up on the TEM-grid after closing them. This problem could for example be solved by using a TEM-grid holder such as the one previously shown in Figure 4.18a and 4.18c. Using such a grid holder simplifies the alignment of the gripper fingers with the TEM-grid rim. For this project however, the choice was made to automatically retrieve the TEM-grids from the grid-box instead of retrieving them from one of the previously mentioned TEM-grid holders. The reasoning here was simple: The TEM-grids were delivered in the grid box. Manually retrieving them from the grid box to place them in a designed TEM-grid holder was more likely to damage the TEM-grids than directly retrieving them from the grid box with the selected gripper fingers and Meca500. In a final automated workflow, storage boxes for TEM-grids should be adjusted to allow for alignment of the used gripper fingers with the rims of the TEM-grids. Another possible solution for the problem that the TEM-grids can be in multiple positions inside the grid box, could be to place the grid box under an angle with the gravitational force. Gravitational forces will then cause the TEM-grid to be on one side of the hole in the grid box. To further improve the alignment, a microscope such as the one mentioned in Section 6.3 could be used. Such a microscope could also be used to obtain the image of the orientation of the TEM-grid that is required for mapping the orientation of the TEM-grid to the Autogrid cartridge.

6.4.2. Experiment 4B

Since the orientation of the TEM-grid with respect to the Autogrid cartridge could not be adjusted in the current clipping process, the mean difference of 5 degrees between the mapped orientation and the orientation obtained after placing the TEM-grid in the Autogrid cartridge was already a major improvement compared to the current clipping process. The procedure of mapping the orientation of the TEM-grid to the Autogrid cartridge can however be improved further.

Figure 6.5: Picture of the bottom of the Autogrid cartridge and of the TEM-grid just before the gripper fingers release the TEM-grid in the Autogrid cartridge, showing that the gripper fingers were under a slight angle.

One thing that was not accounted for in the current approach, was the angle of the gripper fingers with respect to the Autogrid cartridge. Figure 6.5 shows the bottom of the Autogrid cartridge just before the gripper fingers released the TEM-grid. This picture already shows that the gripper fingers were under a slight angle with the Autogrid cartridge. Taking into account the angle between the gripper fingers and the Autogrid cartridge could further improve the predictions of the orientation of the TEM-grid in the Autogrid cartridge after placement.

Also, in the current approach to mapping the orientation of the TEM-grid to the Autogrid cartridge, points on the TEM-grid and gripper fingers were manually selected to obtain the orientation. In a final automated solution for clipping the Autogrid, these points are preferably detected automatically. As the TEM-grids and gripper fingers have quite some distinct features, a machine learning algorithm such as the one that was used to detect the ROI and markers for experiment 2, could easily be trained to identify the position of the TEM-grid and gripper fingers. Using the automatic detection of these positions, could further decrease the difference between the mapped orientation of the TEM-grid in the Autogrid cartridge and the obtained orientation of the TEM-grid in the Autogrid cartridge after placement.

The difference between the mapped orientation and the obtained orientation after placement was probably not only caused by the angle between the gripper fingers, or by the human factor in the mapping algorithm. The orientation of each of the five placed TEM-grids, was mapped to the Autogrid cartridge ten times. The obtained standard deviation within one placement test (PT1, PT2, PT3, PT4, or PT5) provides information on the variance caused by the chosen approach to mapping the orientation. That the standard deviation within one placement test is smaller than the standard deviation over all 50 tests (ten times mapping the orientation for five TEM-grids), and that the standard deviation within one test is smaller than the difference between the obtained values for each test, suggests that the difference between the mapped orientation and the obtained orientation after TEM-grid placement was not only caused by the human factor in the mapping approach. When allowing for negative values, the mean difference and standard deviation of the difference over all 50 tests were -1.1 and 5.4, respectively. If the difference between the mapped orientation and the orientation obtained after placing the TEM-grid was caused by not taking into account the angle between the gripper fingers and the Autogrid, this would cause either a positive or a negative offset in the difference for all five cases. After all, the pathway followed by the Meca500, grippers, gripper fingers, and TEM-grid, during placement, was similar for all five cases. The difference between the mapped orientation of the TEM-grid and the orientation of the TEM-grid in the Autogrid cartridge after placement, was probably caused by a moment of contact between the gripper fingers and the Autogrid cartridge. After opening the gripper fingers, the gripper fingers were retrieved using the same pathway that was used to position the closed gripper fingers with TEM-grid to the correct position for placing the TEM-grid. During retrieval of the open gripper fingers, the gripper fingers slightly tapped the Autogrid cartridge. This slight tap might have caused the TEM-grid to rotate slightly in the Autogrid cartridge since there was no c-clip present holding the TEM-grid in place. A better alignment procedure could help avoid touching the Autogrid cartridge with the gripper fingers after placing the TEM-grid. A test setup that includes a microscope such as the one proposed in Section 6.3 and Subsection 6.4.1 could help with improving the alignment of the gripper fingers before, during, and after placing the TEM-grid.

6.5. General discussion

Of the four experiments (experiment 1, 2, 3, and 4), only one was performed in cryogenic conditions (experiment 1). If the other experiments were performed under cryogenic conditions, this might have had an effect on the results. The low temperature might have an effect on the friction between the rotating part of the Autogrid holder and the Autogrid cartridge in experiment 2. This might cause the mechanism to fail. A follow-up experiment under cryogenic conditions is required to ensure rotating the Autogrid cartridge using the Autogrid holder is still possible under cryogenic conditions. The low temperature might also have an effect on the amount of damage on the TEM-grids in experiment 4. Under cryogenic conditions the mechanical properties of the carbon layer are likely to differ slightly. The carbon layer could for example be more brittle under cryogenic conditions. Recommendations for future work are therefore to perform similar experiments with improved methods (e.i. the improvements mentioned in the preceding sections) in cryogenic conditions.

When using the approach for automatic handling of TEM-grids and Autogrids as proposed in this report, two different gripper fingers are required. This would require either two robot arms with grippers (such as the MEGP25 and Meca500), or some smart design that allows for changing gripper fingers on the same grippers (e.g. similar to tool changing mechanisms used in CNC applications). One of the benefits of using the two different gripper fingers, is that the clipping procedure can be integrated with the plunge freezing step that precedes the clipping procedure (see Section 4.5). To the author's opinion this advantage outweighs the disadvantage of having to use two different gripper fingers. Even if this would require using two robot arms such as the Meca500, this would still be a relatively cheap option. The current price for the Meca500 is €15.000 while the price for a plunge freezing device is €80.000. Integrating plunge freezing and clipping into one automatic procedure, also allows for automatic handling before plunge freezing. Before plunge freezing, in the current cryo-ET workflow, TEM-grids are manually handled using tweezers with a risk of damaging them on beforehand (see Section 2.2.5). Using this approach will not only increase the yield during clipping, but could also increase the yield of the steps preceding clipping of the Autogrid. At the start of the cryo-ET workflow cells are cultured on a petridish. Connecting the workflow steps before clipping was not within the scope of the current project. Nonetheless, one possible solution for connecting all the steps from cell culture to clipping is given in Appendix A.

Integrating clipping of the Autogrid with plunge freezing would require a stable environment in which optimal conditions for the cells can be maintained. As described above, such a stable environment would also have improved the results for many of the experiments described above. Using such a stable environment for clipping and plunge freezing could also help to decrease the amount of contamination of the sample after plunge freezing. Because features of the TEM-grids are hard to observe by eye, this stable environment should include a microscope with alignment of all steps. This microscope could then also be used for inspecting the sample before and after plunge freezing, and for checking the quality of ice after plunge freezing.

7 Conclusion

In general, experimental results suggested that the different developed solutions for all clipping steps have a great potential of being implemented into a final automated solution. Results from experiment 1 can be used to design and test a final automated solution for c-clip insertion. Although not yet perfect, results from experiment 2 and experiment 4B show that the proposed solutions can be used to solve the two problems (p_1 and p_2) concerning the orientation of the TEM-grid and the orientation of the Autogrid cartridge (described in Section 3.5). The two different designed and tested gripper fingers (experiments 3 and 4) can be used for automatic handling of Autogrids and TEM-grids. The gripper fingers used to handle Autogrids could be improved slightly by ensuring a more equal force distribution over the contact points on the Autogrid cartridge. Using the proposed techniques for automatic handling of Autogrids and TEM-grids is likely to increase the sample yield, even more so for novice users. Further research in which the current methods are investigated under cryogenic conditions in a stable environment is required. Also, the effect of samples being present on a TEM-grid on the amount of damage on a TEM-grid should be investigated. Although with the current approach, different gripper fingers are required for handling Autogrids and TEM-grids, the gripper fingers used for handling TEM-grids can be used for plunge freezing as well. Therefore, the current approach can potentially be used to integrate plunge freezing and clipping into one automated procedure. Final recommendations are to use the proposed methods and designs in a stable environment. This stable environment should include a microscope that can be used to perform all required alignment steps. This microscope can then also be used to obtain the orientation of the TEM-grid for mapping, to inspect the sample before and after plunge freezing, and to check the quality of ice after plunge freezing. In this stable environment two robot arms could be used: one dedicated to plunge freezing and TEM-grid placement, the other dedicated to automatic handling of Autogrids. Finally, the Autogrid holder should be redesigned slightly to incorporate a stepper motor in the design for a more stable performance.

Bibliography

[1] A. Al-Amoudi, L. P. O. Norlen, and J. Dubochet. Cryo-electron microscopy of vitreous sections of native biological cells and tissues. *Journal of structural biology*, 148(1):131–135, 2004.

[2] L. A. Arsenault, P. F. Ottensmeyer, and B.I. Heath. An electron microscopic and spectroscopic study of murine epiphyseal cartilage: analysis of fine structure and matrix vesicles preserved by slam freezing and freeze substitution. *Journal of ultrastructure and molecular structure research*, 98(1):32–47, 1988.

[3] W. B. Bald. *Quantitative cryofixation*. Hilger, 1987.

[4] M. Bárcena, G.T. Oostergetel, W. Bartelink, F.G.A. Faas, A. Verkleij, P.J.M. Rottier, A.J. Koster, and B.J. Bosch. Cryo-electron tomography of mouse hepatitis virus: insights into the structure of the coronavirion. *Proceedings of the National Academy of Sciences*, 106(2):582–587, 2009.

[5] T.A.M. Bharat, T. Noda, J.D. Riches, V. Kraehling, L. Kolesnikova, S. Becker, Y. Kawaoka, and J.A.G. Briggs. Structural dissection of ebola virus and its assembly determinants using cryo-electron tomography. *Proceedings of the National Academy of Sciences*, 109(11):4275–4280, 2012.

[6] B. Bikker. Measurement of cooling rate during plunge freezing of sample preparation in cryo electron microscopy. Master's thesis, TU Delft, 08 2019.

[7] K. Bobik, J. R. Dunlap, and T. M. Burch-Smith. Tandem high-pressure freezing and quick freeze substitution of plant tissues for transmission electron microscopy. *JoVE (Journal of Visualized Experiments)*, (92):e51844, 2014.

[8] P. Brüggeller and E. Mayer. Complete vitrification in pure liquid water and dilute aqueous solutions. *Nature*, 288(5791):569, 1980.

[9] G. Cardone, D. C. Winkler, B. L. Trus, N. Cheng, J. E. Heuser, W.W. Newcomb, J.C. Brown, and A.C. Steven. Visualization of the herpes simplex virus portal in situ by cryo-electron tomography. *Virology*, 361(2): 426–434, 2007.

[10] J. Coetzee and C.F. Van der Merwe. Extraction of substances during glutaraldehyde fixation of plant cells. *Journal of Microscopy*, 135(2):147–158, 1984.

[11] M. Cyrklaff, C. Risco, J.J. Fernández, M. V. Jiménez, M. Estéban, W. Baumeister, and J. L. Carrascosa. Cryo-electron tomography of vaccinia virus. *Proceedings of the National Academy of Sciences*, 102(8): 2772–2777, 2005.

[12] R. de Borst and L.J. Sluys. *Computational methods in non-linear solid mechanics*. 2015.

[13] Delmic. Survey among customers on sample preparation, technical report, 2018.

[14] R. Fernández-Busnadiego. Protein aggregation up-close. `https://www.youtube.com/watch?v=r_mVjaM_cyw&feature=youtu.be`, 2020. Accessed: 2020-10-28.

[15] A. Field. *Discovering statistics using IBM SPSS statistics*. sage, 2013.

[16] S. Gorelick, G. Buckley, G. Gervinskas, T.K. Johnson, A. Handley, M.P. Caggiano, J.C. Whisstock, R. Pocock, and A. de Marco. Pie-scope, integrated cryo-correlative light and fib/sem microscopy. *eLife*, 8, 2019.

[17] K. Grünewald, P. Desai, D.C. Winkler, J.B. Heymann, D.M. Belnap, W. Baumeister, and A.C. Steven. Three-dimensional structure of herpes simplex virus from cryo-electron tomography. *Science*, 302(5649):1396–1398, 2003.

[18] A. Harris, G. Cardone, D.C. Winkler, J.B. Heymann, M. Brecher, J.M. White, and A.C. Steven. Influenza virus pleiomorphy characterized by cryoelectron tomography. *Proceedings of the National Academy of Sciences*, 103(50):19123–19127, 2006.

[19] Ideal-tek. Plastic replaceable tip tweezers. `https://www.ideal-tek.com/scheda.php?m=search&f=8&c=Plastic%20Tweezer%20Tips&l=3&idp=1115`, 2020. Accessed: 2020-11-01.

[20] Haydon Kerk. Size 08 stepper linear actuators. `https://www.haydonkerkpittman.com/products/linear-actuators/hybrid-stepper/size-8`, 2020. Accessed: 2020-11-07.

[21] T. Klein, E. Buhr, and C. G. Frase. Tsem: A review of scanning electron microscopy in transmission mode and its applications. In *Advances in imaging and electron physics*, volume 171, pages 297–356. Elsevier, 2012.

[22] A. Leforestier and F. Livolant. Distortion of dna cholesteric liquid crystal quenched at low temperature: geometrical analysis and models. *Journal de Physique II*, 2(10):1853–1880, 1992.

[23] A. Leforestier, K. Richter, F. Livolant, and J. Dubochet. Comparison of slam-freezing and high-pressure freezing effects on the dna cholesteric liquid crystalline structure. *Journal of microscopy*, 184(1):4–13, 1996.

[24] D.R. Lide. *CRC handbook of chemistry and physics*, volume 85. CRC press, 2004.

[25] J. Liu. Meteor launch. `https://blog.delmic.com/news/dive-in-meteor-launch-demonstration-in-october hsCtaTracking=8427134a-92e3-4538-9337-961d824b25c6%7Ce1f3e10b-d409-4327-b043-0b4bfbe31da3`, 2020. Accessed: 2020-10-22.

[26] M.P. Manoharan, H. Lee, R. Rajagopalan, H.C. Foley, and A. Haque. Elastic properties of 4–6 nm-thick glassy carbon thin films. *Nanoscale research letters*, 5(1):14, 2010.

[27] Azo Materials. Carbon - graphite materials. `https://www.azom.com/properties.aspx?ArticleID=516`, 2001. Accessed: 2020-05-06.

[28] K. McDonald, H. Schwarz, T. Müller-Reichert, R. Webb, C. Buser, and M. Morphew. “tips and tricks” for high-pressure freezing of model systems. In *Methods in cell biology*, volume 96, pages 671–693. Elsevier, 2010.

[29] K. L. McDonald. A review of high-pressure freezing preparation techniques for correlative light and electron microscopy of the same cells and tissues. *Journal of microscopy*, 235(3):273–281, 2009.

[30] K. L. McDonald and M. Auer. High-pressure freezing, cellular tomography, and structural cell biology. *Biotechniques*, 41(2):137–143, 2006.

[31] K. L. McDonald, M. Morphew, P. Verkade, and T. Müller-Reichert. Recent advances in high-pressure freezing. In *Electron Microscopy*, pages 143–173. Springer, 2007.

[32] Mecademic. Megp 25 electric gripper (for meca500), user manual, 2018. Document version: 1.1.

[33] Mecademic. Megp 25 - miniature electric parallel gripper. `https://www.mecademic.com/products/gripper`, 2020. Accessed: 2020-10-30.

[34] J. M. Medeiros, D. Böck, G. L. Weiss, R. Kooger, R. A. Wepf, and M. Pilhofer. Robust workflow and instrumentation for cryo-focused ion beam milling of samples for electron cryotomography. *Ultramicroscopy*, 190:1–11, 2018.

[35] A. J. Morgan. Preparation of specimens. changes in chemical integrity. inx-ray microanalysis in biology (edited by hayat, ma), 1980.

[36] K. Murata and M. Wolf. Cryo-electron microscopy for structural analysis of dynamic biological macromolecules. *Biochimica et Biophysica Acta - General Subjects*, 1862(2):324–334, 2018.

[37] H. Park, D. Woo, J. M. Lee, S. J. Park, S. Lee, H. J. Kim, E. Yoon, and G. Lee. First principles investigation on energetics, structure, and mechanical properties of amorphous carbon films doped with b, n, and cl. *Scientific Reports*, 9(1):1–10, 2019.

[38] D. Parlitz, T. Peschel, and E. Altenmüller. Assessment of dynamic finger forces in pianists: effects of training and expertise. *Journal of biomechanics*, 31(11):1063–1067, 1998.

[39] L. A. Passmore and C. J. Russo. Specimen preparation for high-resolution cryo-em. In *Methods in enzymology*, volume 579, pages 51–86. Elsevier, 2016.

[40] J. Plitzko and W.P. Baumeister. Cryo-electron tomography. *Springer Handbooks*, pages 189–228, 2019.

[41] Quuantifoil. Holey carbon films. `https://www.quantifoil.com/index.php?name=quantifoil`, 2019. Accessed: 2020-01-06.

[42] R. B. G. Ravelli, F. J. T. Nijpels, R. J. M. Henderikx, G. Weissenberger, S. Thewessem, A. Gijsbers, B. W. A. M. M. Beulen, C. Lopez-Iglesias, and P. Peters. Automated cryo-em sample preparation by pin-printing and jet vitrification. *bioRxiv*, page 651208, 2019.

[43] A. Rigort, F. J. B. Bäuerlein, A. Leis, M. Gruska, C. Hoffmann, T. Laugks, U. Böhm, M. Eibauer, H. Gnaegi, and W. Baumeister. Micromachining tools and correlative approaches for cellular cryo-electron tomography. *Journal of structural biology*, 172(2):169–179, 2010.

[44] A. Rigort, G. Qiang, F. J.B. Bäuerlein, and Fernández-Busnadiego R. The combination of cryo-fib and in situ cryo-electron tomography enables ultrastructural analysis of disease-related protein aggregates. `https://analyticalscience.wiley.com/do/10.1002/micro.2737`, 2018. Accessed: 2020-10-21.

[45] K. P. Ryan. Rapid cryogenic fixation of biological specimens for electron microscopy. 1991.

[46] Agar Scientific. Tweezers assembly for vitrobot mark iv, iii, ii & i. `https://www.agarscientific.com/fr/replacement-tweezers-assembly-for-fei-vitrobot-mark-iv-i?___store=france&___from_store=default`, 2020. Accessed: 2020-11-20.

[47] M. Sokolova and G. Lapalme. A systematic analysis of performance measures for classification tasks. *Information processing & management*, 45(4):427–437, 2009.

[48] Peterson spring. Retaining rings technical manual. `https://www.pspring.com/wp-content/uploads/2016/03/Retaining-Rings-Training-Manual-FINAL-press.pdf`, 2019. Accessed: 2019-11-20.

[49] S. Subramaniam. The cryo-em revolution: fueling the next phase. *IUCrJ*, 6(Pt 1):1, 2019.

[50] Tedpella. Pelco grids for transmission electron microscopy packed in anti-static vials. `https://www.tedpella.com/grids_html/Pelco-TEM-Grids.htm#anchor35256`, 2019. Accessed: 2019-11-21.

[51] Engineering toolbox. Metals and alloys - densities. `https://www.engineeringtoolbox.com/metal-alloys-densities-d_50.html`, 2019. Accessed: 2019-11-20.

[52] Engineering toolbox. Young's modulus - tensile and yield strength for common materials. `https://www.engineeringtoolbox.com/young-modulus-d_417.html`, 2019. Accessed: 2019-11-20.

[53] Trinamic. Tmcm-6110. `https://www.trinamic.com/products/modules/details/tmcm-6110/`, 2020. Accessed: 2020-11-07.

[54] R.D. van den Berg. Automation of the clipping process in cryogenic electron microscopy, literature report, 02 2020.

[55] D. Vanhecke, G. Herrmann, W. Graber, T. Hillmann-Marti, C. Mühlfeld, D. Studer, and M. Ochs. Lamellar body ultrastructure revisited: high-pressure freezing and cryo-electron microscopy of vitreous sections. *Histochemistry and cell biology*, 134(4):319–326, 2010.

[56] J.M. Walker, B. Marzec, N. Ozaki, D. Clare, and F. Nudelman. Morphological development of pleurochrysis carterae coccoliths examined by cryo-electron tomography. *Journal of Structural Biology*, page 107476, 2020.

[57] P. Walther and A. Ziegler. Freeze substitution of high-pressure frozen samples: the visibility of biological membranes is improved when the substitution medium contains water. *Journal of microscopy*, 208(1): 3–10, 2002.

[58] G. Wolff, C. Hagen, K. Grünewald, and R. Kaufmann. Towards correlative super-resolution fluorescence and electron cryo-microscopy. *Biology of the Cell*, 108(9):245–258, 2016.

[59] G. Wolff, R.W.A.L. Limpens, J. C. Zevenhoven-Dobbe, U. Laugks, S. Zheng, A.W.M. de Jong, R. I. Koning, D.A. Agard, K. Grünewald, A.J. Koster, et al. A molecular pore spans the double membrane of the coronavirus replication organelle. *Science*, 369(6509):1395–1398, 2020.

[60] CryoSol World. Vitrojet. `https://www.cryosol-world.com/vitrojet/`, 2019. Accessed: 2019-12-12.

[61] P. Zhang. Correlative cryo-electron tomography and optical microscopy of cells. *Current Opinion in Structural Biology*, 23(5):763–770, 2013.

A

VacuTEMgripper

In this appendix, an alternative to TEM-grid gripping that was investigated during preliminary testing is described. The reason this alternative is described here, is that it was not necessarily used for automating any of the clipping steps. As it shows promise of being used in a different part of the cryo-ET workflow it is still mentioned here. Figure A.1 shows an illustration of the proposed mechanism for picking up TEM-grids. Here, the black arrows indicate a vacuum that is applied on the rim of the TEM-grid. The center of the TEM-grid is in contact with air to avoid damaging the fragile carbon layer over the grid holes. Using such a mechanism, a TEM-grid can be picked up when in horizontal position. This "gripper" is hereafter referred to as VacuTEMgripper.

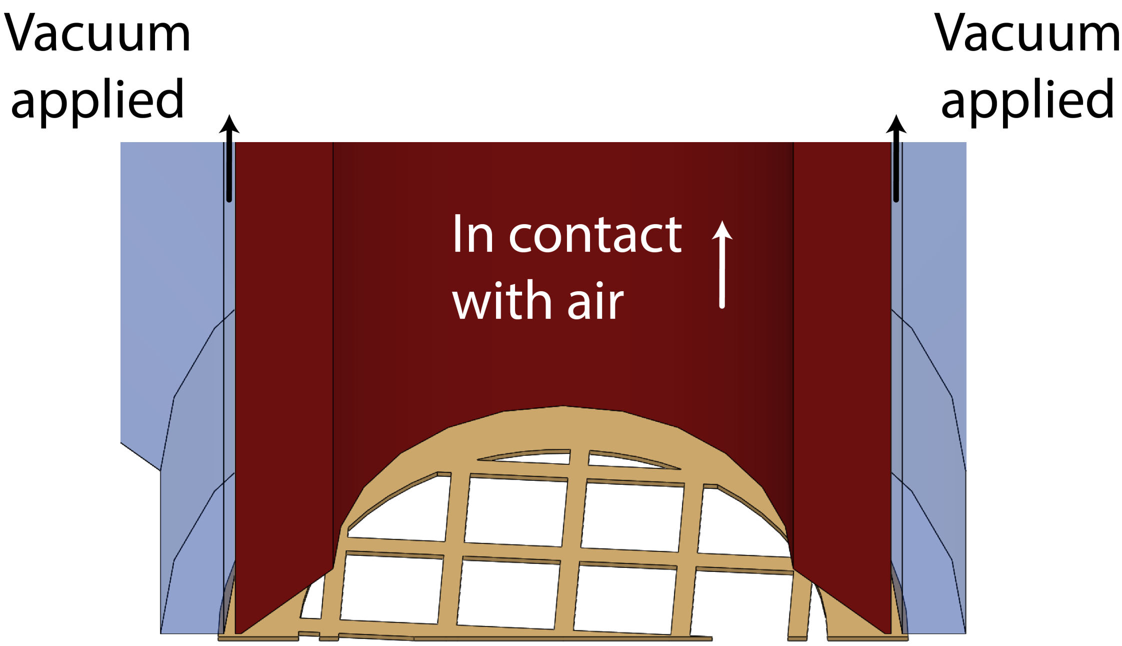

Figure A.1: Mechanism for using a vacuum on the rim of a TEM-grid to pick it up from a horizontal orientation.

Picking up TEM-grids from a horizontal position can be used in a different step in the cryo-ET workflow. At the start of the cryo-ET workflow, cells are cultured on TEM-grids in a petri dish. For the cells to grow on the TEM-grids, the TEM-grids have to be in horizontal position. The VacuTEMgripper could then be used to obtain the TEM-grid from the petri dish. Figure A.2 shows an example of an automated workflow using the designs proposed earlier with the VacuTEMgripper. First, cells are cultured on TEM-grids in a petri dish. Then, the VacuTEMgripper is used to retrieve a TEM-grid in horizontal position. A dedicated TEM-grid holder is used in which the VacuTEMgripper can release the TEM-grid. A cutout in the TEM-grid holder allows for aligning gripper fingers such as the ones used for automatic TEM-grid handling in experiment 4.

The TEM-grid is plunge frozen using these same gripper fingers. Thereafter, the 6 clipping steps as proposed in this report are performed and the Autogrid is inserted in the cassette in the correct orientation. Lastly, the cassette is transferred to a transfer unit.

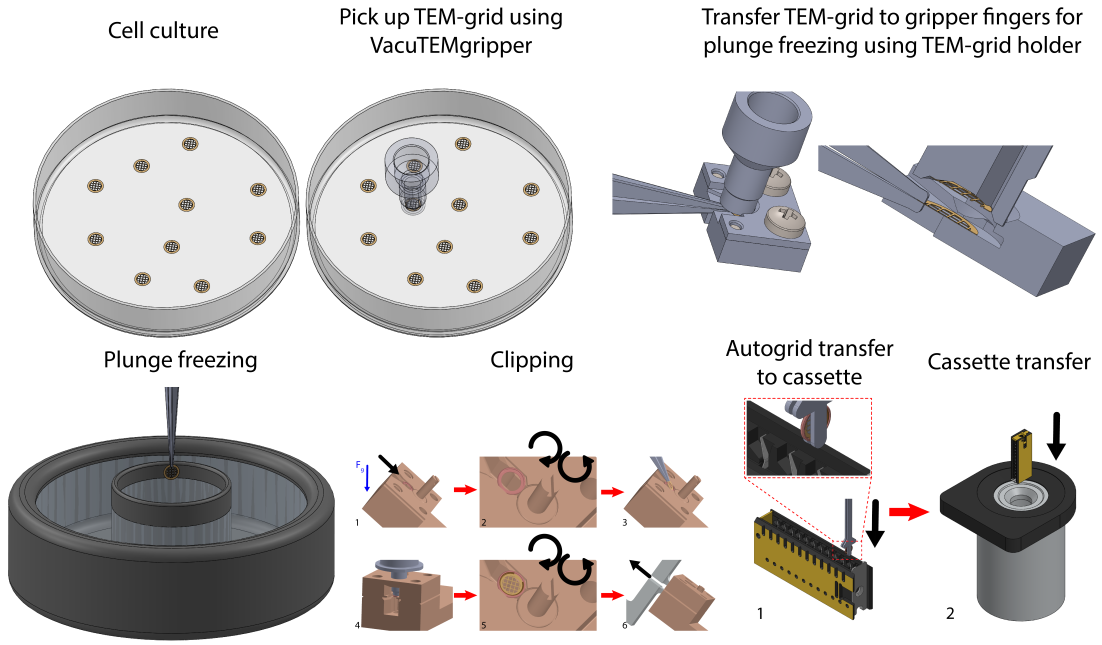

Figure A.2: Illustration of how the VacuTEMgripper could be used for further automation and integration of the cryo-ET workflow.

Such an approach can be used as a solution for an integrated automated workflow for cryo-ET. Preliminary tests with 3D printed parts suggested that picking up TEM-grids with such a mechanism is possible. A few points should be considered in future designs and research: There should be certain constraints to the flatness of the part of the VacuTEMgripper that is in contact with the rim of the TEM-grid to ensure a good seal. Cells in a petri dish are often cultured in an aqueous medium. The design for the VacuTEMgripper should account for such a liquid substance.

B

Additional images

Figure B.1: The assembled new clipping pen.

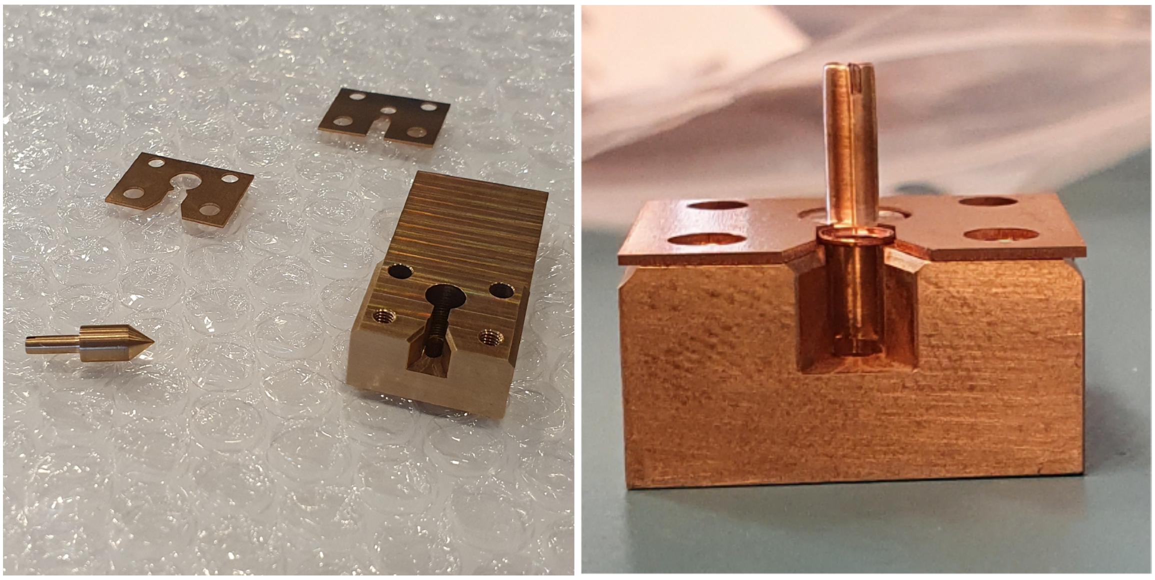

(a) (b)

Figure B.2: (a) The manufactured parts for the Autogrid holder (b) An Autogrid on two parts of the Autogrid holder.

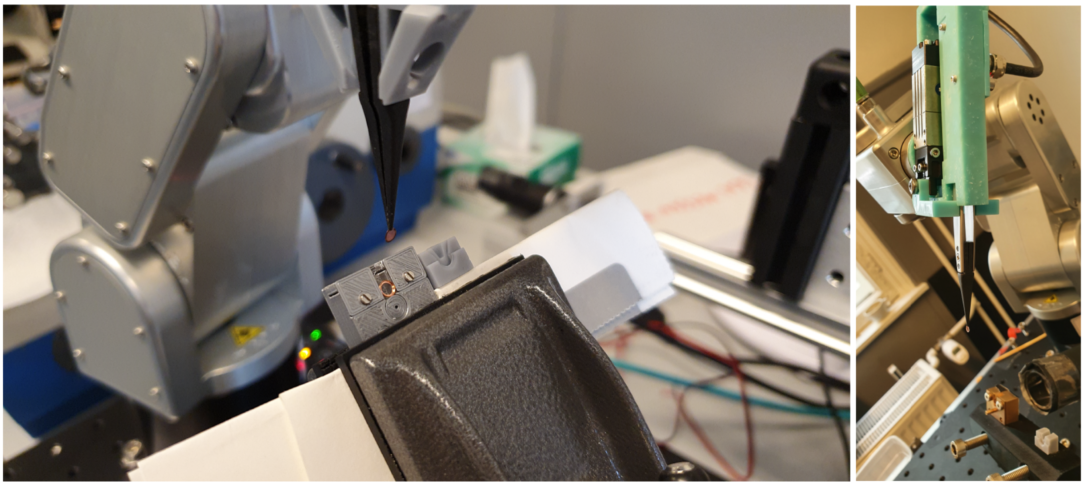

(a) (b)

Figure B.3: (a) The second gripper fingers (g_2) while placing a TEM-grid in an Autogrid cartridge during preliminary testing. (b) The third gripper fingers (g_3) holding a TEM-grid in preliminary testing.

C
Technical drawings

C.1. Technical drawings MEGP-25

Figure C.1 shows the technical drawings of the MEGP-25 grippers.

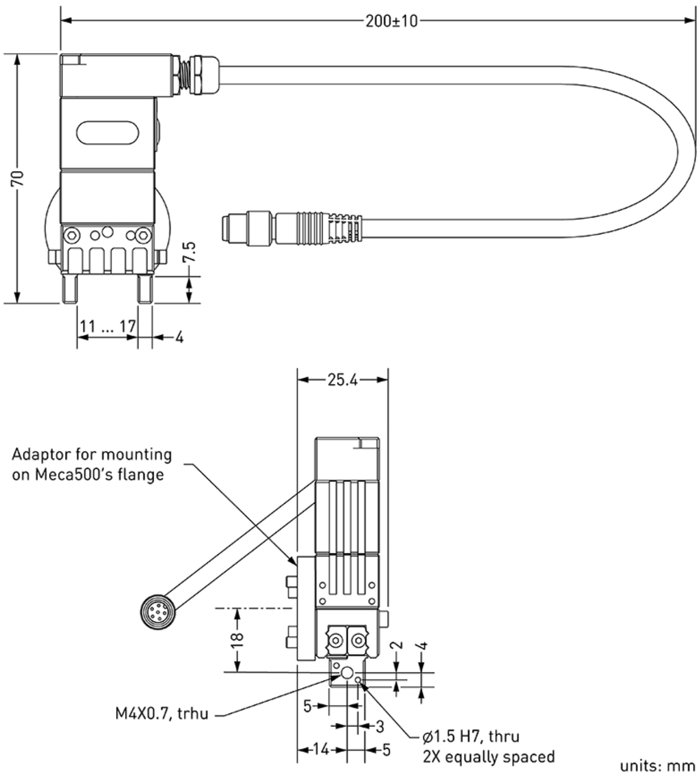

Figure C.1: Technical drawings of the MEGP-25 grippers, image from user manual [32]

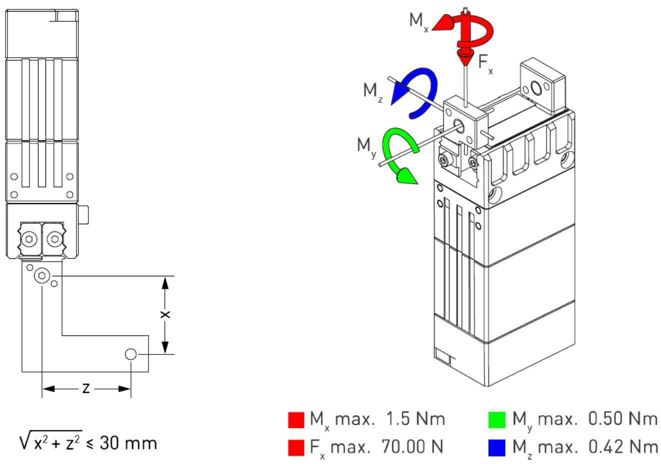

Figure C.2: Technical drawings of the MEGP-25 grippers showing the allowed force and dimensions for the gripper fingers, image from user manual [32]

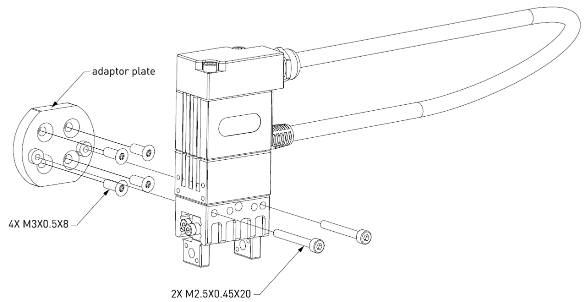

Figure C.3: Technical drawings of the MEGP-25 grippers showing the attachment to the adaptor plate between the MEGP-25 and the flange on the Meca500, image from user manual [32]

D

MATLAB code

D.1. Matlab code for analytical calculations

```
clear
close all
clc

figure;hold on
i=1;
for F=0.1*10^-3:0.3*10^-3:1.6*10^-3
F_vv(i)=F;
E=110*10^9;
d=0.2*10^-3;
D=3.1*10^-3+F;
r=d/2;
A=pi*r^2;
P=pi*d;
V_clip=2.4*10^-10;

rho_clip=8900; % kg/m^3
M_clip=rho_clip*V_clip;
Fg_clip=9.8*M_clip;


Pg=(E*(d^4)*F)/(4*D^3);
Fe=Pg;


theta=10;

mu=[0:0.01:1.2];
FN=cosd(theta)*Fe;
Fef=sind(theta)*Fe;
Ff=mu.*FN;

F_req=((-sind(theta)*Fe)+(mu.*cosd(theta)*Fe))/cosd(theta);

plot(mu,F_req,'LineWidth',2)

i=i+1;
end
```

```
hold off

xlabel('\mu')
ylabel('F_{req} (in N)')
set(gca,'FontSize',16)
for iii=1:length(F_vv)
AA(iii,:)='u = ';
CC(iii,:)=' mm';
end
B=num2str(F_vv'.*1000);
LEGEND=[AA B CC];
legend(LEGEND)
```

D.2. MATLAB code for training the machine learning algorithm

For training the algorithm to detect the region of interest and to detect the markers on the bottom of the Autogrid, a similar code was used which is given below.

```
clear
clc
close all

%% Un comment this section to label images
% imds = imageDatastore('TestOri8Frames')
%
%
%
% trainingImageLabeler


%% Using labeled images to train algorithm
% load('LabelsFromImages3.mat')
% load('LabelsFromImages4__twofold.mat')
load('RegionOfInterest3Labels.mat')
trainingData = objectDetectorTrainingData(gTruth);



% negativeFolder = fullfile(matlabroot,'toolbox','vision','visiondata',...
%     'nonStopSigns');

negativeFolder = 'NegativeForRegionOfINterest';

negativeImages = imageDatastore(negativeFolder);

%% Multiple options for the ML algorithm
% trainCascadeObjectDetector('MarkerDetector4.xml',trainingData, ...
%     negativeFolder,'FalseAlarmRate',0.1,'NumCascadeStages',5);
% trainCascadeObjectDetector('MarkerDetector6.xml',trainingData, ...
%     negativeFolder,'FalseAlarmRate',0.1);
trainCascadeObjectDetector('RegionOfInterestDetector3_moreNegatives.xml',
    trainingData, ...
    negativeFolder);


%% Create the marker detector
detector = vision.CascadeObjectDetector('RegionOfInterestDetector3_moreNegatives.xml
    ');
```

```
%% Test one image
% img = imread('FramesFolder2\Autogrid_10.png');
% img = imread('FramesFolder1\AutogridRim_14.png');
% bbox = step(detector,img);
% detectedImg = insertObjectAnnotation(img,'rectangle',bbox,'marker');
% figure; imshow(detectedImg);




%% Test multiple images
close all
for k=30:4:190
    str1='TestOri8Frames\Autogrid_';
%     str1='FramesFolder2\Autogrid_';
    str2=num2str(k);
    str3='.png';
    str=[str1 str2 str3];

    imgk = imread(str);
    bbox = step(detector,imgk);
    detectedImg = insertObjectAnnotation(imgk,'rectangle',bbox,'marker');
    figure; imshow(detectedImg);
end
```

D.3. MATLAB code for testing the two algorithms in Experiment 2A

D.3.1. MATLAB code for testing the ML approach

```
clear
close all
clc

detector = vision.CascadeObjectDetector('MarkerDetector15.xml');
detectorROI = vision.CascadeObjectDetector('RegionOfInterestDetector3_moreNegatives.
    xml');

VideoName = 'TestingWithMicroscope5_MarkingAllObjects';
VideoFormat = '.avi';
VideoFileName=[VideoName VideoFormat];
vidWriter = VideoWriter(VideoFileName);
open(vidWriter);

VideoFileNameROI=[VideoName 'ROI' VideoFormat];
vidWriter2 = VideoWriter(VideoFileNameROI);
open(vidWriter2);



for i=1:112
    if i>30
    BWROI_n=zeros(1944,2592);
    Folder = 'TestingWithMicroscope5';
    string1='\Autogrid_';
    string2=num2str(i);
```

```
    string3='.png';
    string=[Folder string1 string2 string3];
    img=imread(string);
    ImGrInt=im2double(img);

    bboxROI = step(detectorROI,img);
    detectedImgROI = insertObjectAnnotation(img,'rectangle',bboxROI,'marker');

    [A]=find(bboxROI(:,3)==max(bboxROI(:,3)));
    [B]=find(bboxROI(:,4)==max(bboxROI(:,4)));
    if isempty(A)==1
            bboxROI=bboxROI_N;
    elseif bboxROI(A,3)>300 && bboxROI(B,3)>250
            BWROI_n(bboxROI(A,2):bboxROI(A,2)+round(bboxROI(A,4)),bboxROI(A,1):
                bboxROI(A,1)+round(bboxROI(A,3)))=1;
    end

    bboxROI_N=bboxROI;

    ImgROI=(BWROI_n).*ImGrInt;

    bbox = step(detector,ImgROI);
    [M,N]=size(bbox);


    detectedImg = insertObjectAnnotation(img,'rectangle',bbox,'marker');

    writeVideo(vidWriter, im2uint8(ImgROI));
    writeVideo(vidWriter2, detectedImg);

    end
end

close(vidWriter);
close(vidWriter2);
```

D.3.2. MATLAB code for testing the ML_{mc} approach

```
clear
close all
clc

detector = vision.CascadeObjectDetector('MarkerDetector15.xml');
detectorROI = vision.CascadeObjectDetector('RegionOfInterestDetector3_moreNegatives.
    xml');

VideoName = 'TestingWithMicroscope5_MarkingAllObjects_maskedCenter';
VideoFormat = '.avi';
VideoFileName=[VideoName VideoFormat];
vidWriter = VideoWriter(VideoFileName);
open(vidWriter);

VideoFileNameROI=[VideoName 'ROI' VideoFormat];
vidWriter2 = VideoWriter(VideoFileNameROI);
open(vidWriter2);

Center=[1365 1070];
```

```
CenterR=160;
mask=createCirclesMask([1944,2592],[Center(1),Center(2)],CenterR);


for i=1:112
    if i>30
    BWROI_n=zeros(1944,2592);
    Folder = 'TestingWithMicroscope5';
    string1='\Autogrid_';
    string2=num2str(i);
    string3='.png';
    string=[Folder string1 string2 string3];
    img=imread(string);
    ImGrInt=im2double(img);

    bboxROI = step(detectorROI,img);
    detectedImgROI = insertObjectAnnotation(img,'rectangle',bboxROI,'marker');

    [A]=find(bboxROI(:,3)==max(bboxROI(:,3)));
    [B]=find(bboxROI(:,4)==max(bboxROI(:,4)));
    if isempty(A)==1
            bboxROI=bboxROI_N;
    elseif bboxROI(A,3)>300 && bboxROI(B,3)>250
            BWROI_n(bboxROI(A,2):bboxROI(A,2)+round(bboxROI(A,4)),bboxROI(A,1):
                bboxROI(A,1)+round(bboxROI(A,3)))=1;
    end

    bboxROI_N=bboxROI;

    ImgROI=imcomplement(mask).*(BWROI_n).*ImGrInt;

%     img=im2uint8(imcomplement(mask).*im2double(img));

    bbox = step(detector,ImgROI);
    [M,N]=size(bbox);


    detectedImg = insertObjectAnnotation(img,'rectangle',bbox,'marker');

    writeVideo(vidWriter, im2uint8(detectedImg));
    writeVideo(vidWriter2,ImgROI);

    end
end

close(vidWriter);
close(vidWriter2);
```

D.3.3. MATLAB code for testing the CHT approach

```
clear
close all
clc

Folder2 = 'TestingWithMicroscope5_CHT';
Folder = 'TestingWithMicroscope5';
string1='\Autogrid_';
```

```
string3='.png';

for i=1:112
    if i>30

    string2=num2str(i);
    string2w=num2str(i-30);

    string=[Folder string1 string2 string3];
    img=imread(string);

    ImGrCrop=img(880:1300,1100:1630);
    ImGrCrop2=imadjust(ImGrCrop);

    figure(1);imshow(ImGrCrop2)
    hold on

    Sens=0.95;
    EdgeTre=0.1;
    Obj='dark';

    [centers1, radii1, metric1] = imfindcircles(ImGrCrop2,[16 30],'ObjectPolarity',
        Obj,'Sensitivity',Sens,'EdgeThreshold',EdgeTre);

    viscircles(centers1(:,:), radii1(:),'EdgeColor','r');

    filenamesavefigure=[Folder2 string1 string2w string3];
    saveas(figure(1),filenamesavefigure)
    close(1)
    end
end
```

D.3.4. MATLAB code for testing the CHT$_{mc}$ approach

```
clear
close all
clc

Folder2 = 'TestingWithMicroscope5_CHT_MaskedCenter';
Folder = 'TestingWithMicroscope5';
string1='\Autogrid_';
string3='.png';

Center=[1365 1070];
CenterR=160;
mask=createCirclesMask([1944,2592],[Center(1),Center(2)],CenterR);
% figure(2);imshow(imcomplement(mask).*im2double(rgb2gray(img)))


for i=1:112
    if i>30

    string2=num2str(i);
    string2w=num2str(i-30);

    string=[Folder string1 string2 string3];
    img=imread(string);
```

```
    img=rgb2gray(img);
    img=imadjust(img);
    img=im2uint8(imcomplement(mask).*im2double(img));




    ImGrCrop=img(880:1300,1100:1630);
%    ImGrCrop2=imadjust(ImGrCrop);



    figure(1);imshow(ImGrCrop)
    hold on

    Sens=0.95;
    EdgeTre=0.1;
    Obj='dark';

    [centers1, radii1, metric1] = imfindcircles(ImGrCrop,[16 30],'ObjectPolarity',
        Obj,'Sensitivity',Sens,'EdgeThreshold',EdgeTre);

    viscircles(centers1(:,:), radii1(:),'EdgeColor','r');

    filenamesavefigure=[Folder2 string1 string2w string3];
    saveas(figure(1),filenamesavefigure)
    close(1)
    end
end
```

D.4. MATLAB code for obtaining images while automatically rotating the Autogrid

Below one of the codes that was written for automatically obtaining images while using the stepper motor to rotate the Autogrid is given. The function: "move.m", was used to control the stepper motor and is also given below.

```
clear
close all
clc


VideoName = 'TestOriNega2';
VideoNameMarked = [VideoName 'Marked'];
detector = vision.CascadeObjectDetector('MarkerDetector15.xml');
detectorROI = vision.CascadeObjectDetector('RegionOfInterestDetector3_moreNegatives.
    xml');


cam = webcam(1);
cam


VideoFormat = '.avi';
VideoFileName=[VideoName VideoFormat];
VideoFileNameMarked=[VideoNameMarked VideoFormat];

```

```
vidWriter = VideoWriter(VideoFileName);
open(vidWriter);
vidWriter2 = VideoWriter(VideoFileNameMarked);
open(vidWriter2);


Center=[1305;1095];

si=[1944;2592];

MaskSizein=160;
MaskSizeout=240;



Sens=0.92;
EdgeTre=0.1;
Obj='dark';


mask=createCirclesMask(si,[Center(1),Center(2)],MaskSizein);
mask2=createCirclesMask(si,[Center(1),Center(2)],MaskSizeout);

maskD=double(mask);
mask2D=double(mask2);
maskDR=imcomplement(maskD);

for index = 1:400
%     tic
    % Acquire frame for processing
    img = snapshot(cam);

    ImGr=rgb2gray(img);


    ImGrCrop2Int=im2double(ImGr);


    AutogridRim=mask2.*maskDR.*ImGrCrop2Int;

    AutogridRimIm=im2uint8(AutogridRim);


    writeVideo(vidWriter, ImGr);



if index>25
%     figure;imshow(ImGr)
%     figure;imshow(AutogridRimIm)
    bbox = step(detector,AutogridRimIm);
    detectedImg = insertObjectAnnotation(img,'rectangle',bbox,'marker');
%     figure;imshow(detectedImg)
    move(-6000)
    writeVideo(vidWriter2, detectedImg);
%     a=1;
```

```
end


%       toc
end

close(vidWriter);
close(vidWriter2);
clear cam


save(['workspaces/' VideoName '.mat'])
```

The function move:

```
function move(nin)
n = int32(nin);


byte(1:4) = uint8([1,4,1,0]);
byte(5)= uint8(bitand(bitshift(n,-24),255) );
byte(6)= uint8(bitand(bitshift(n,-16),255) );
byte(7)= uint8(bitand(bitshift(n,-8),255) );
byte(8)= uint8(bitand(n,255) );
byte(9)=uint8(bitand(sum(byte(1:8)),255) );,


fid = serial('COM4','BaudRate',9600, 'DataBits', 8, 'Parity', 'none','StopBits', 1, 'FlowControl', 'none');
fopen (fid);


fwrite(fid,byte);
pause(1);


a = fread(fid, 9, 'uint8');


fclose(fid);
```

D.5. MATLAB code for Experiment 2B

Below, the MATLAB code used for experiment 2B (Section 4.3.3) is given.

```
clear
close all
clc

VideoName = 'TestingWithOldImages3';
VideoNameMarked = [VideoName 'Marked'];
detector = vision.CascadeObjectDetector('MarkerDetector15.xml');
detectorROI = vision.CascadeObjectDetector('RegionOfInterestDetector3_moreNegatives.xml');


%%%cam = webcam(1);

```

```
%%%cam



VideoFormat = '.avi';
VideoFileName=[VideoName VideoFormat];
VideoFileNameMarked=[VideoNameMarked VideoFormat];

vidWriter = VideoWriter(VideoFileName);
open(vidWriter);
vidWriter2 = VideoWriter(VideoFileNameMarked);
open(vidWriter2);



BWROI_n=zeros(1944,2592);
dil_fac=1;
i=1;
OriLeft=0;
Ori=0;

%%

%%% for index = 1:400
%       tic
%%%%
%% Test with Image
% for i=30:4:394
while OriLeft==0
    i=i+1;
Folder = 'TestOri8Frames_all';
    string1='\Autogrid_';
    string2=num2str(30+i);
    string3='.png';
    string=[Folder string1 string2 string3];
img=imread(string);
index=30+i;

%%
%%%%
    % Acquire frame for processing
%%%     img = snapshot(cam);

    ImGr=rgb2gray(img);



    ImGrInt=im2double(ImGr);



    % Write frame to video

%%%       writeVideo(vidWriter, ImGr);

```

```
if index>30

    bboxROI = step(detectorROI,ImGr);
    detectedImgROI = insertObjectAnnotation(img,'rectangle',bboxROI,'marker');

%     figure;imshow(detectedImgROI)

    %Create masks from detected ROI
%     BWROI_n(bboxROI(1,1):bboxROI(1,1)+bboxROI(1,3),bboxROI(1,2):bboxROI(1,2)+bboxROI(1,4))=1;
    if bboxROI(1,2)>300 && bboxROI(1,4)>250
        BWROI_n(bboxROI(1,2):bboxROI(1,2)+round(dil_fac*bboxROI(1,4)),bboxROI(1,1):bboxROI(1,1)+round(dil_fac*bboxROI(1,3)))=1;
        CenterROI=[bboxROI(1,1)+round(0.5*bboxROI(1,3)),bboxROI(1,2)+round(0.5*bboxROI(1,4))];
        BW_Center=createCirclesMask([1944,2592],CenterROI,50);
    elseif bboxROI(2,2)>300 && bboxROI(2,4)>250
        BWROI_n(bboxROI(2,2):bboxROI(2,2)+round(dil_fac*bboxROI(2,4)),bboxROI(2,1):bboxROI(2,1)+round(dil_fac*bboxROI(2,3)))=1;
        CenterROI=[bboxROI(2,1)+round(0.5*bboxROI(2,3)),bboxROI(2,2)+round(0.5*bboxROI(2,4))];
        BW_Center=createCirclesMask([1944,2592],CenterROI,50);
    elseif bboxROI(3,2)>300 && bboxROI(3,4)>250
        BWROI_n(bboxROI(3,2):bboxROI(3,2)+round(dil_fac*bboxROI(3,4)),bboxROI(3,1):bboxROI(3,1)+round(dil_fac*bboxROI(3,3)))=1;
        CenterROI=[bboxROI(3,1)+round(0.5*bboxROI(3,3)),bboxROI(3,2)+round(0.5*bboxROI(3,4))];
        BW_Center=createCirclesMask([1944,2592],CenterROI,50);
    else
        disp('ROI error at index:')
        disp(index)
    end

    ImgROI=(BWROI_n-BW_Center).*ImGrInt;

    bbox = step(detector,ImgROI);
    [M,N]=size(bbox);

    if M>=2
        detectedImg = insertObjectAnnotation(img,'rectangle',bbox(1:2,:),'marker');
    elseif M<2
        detectedImg = insertObjectAnnotation(img,'rectangle',bbox,'marker');
    else
        detectedImg = img;
        disp('No markers found for index:')
        disp(index)
    end

%     figure;imshow(detectedImg)


%%%     move(-6000)
    writeVideo(vidWriter, im2uint8(ImgROI));
    writeVideo(vidWriter2, detectedImg);
```

```
%       a=1;


if M>=2
    for kk=1:2
%       for kk=1:M
    Center(kk,1)=round(bbox(kk,1)+0.5*bbox(kk,3));
    Center(kk,2)=round(bbox(kk,2)+0.5*bbox(kk,4));
    end
    MarkersVec(1,1)=(Center(1,1)-Center(2,1));
    MarkersVec(1,2)=(Center(1,2)-Center(2,2));
    D_Markers=sqrt(MarkersVec(1,1)^2+MarkersVec(1,2)^2);
    CenterBetweenMarkers(1,1)=round(Center(2,1)+0.5*MarkersVec(1,1));
    CenterBetweenMarkers(1,2)=round(Center(2,2)+0.5*MarkersVec(1,2));
%       sqrt((Center(2,1)-Center(1,1))^2+(Center(2,2)-Center(1,2))^2)
    if D_Markers<60

        if CenterBetweenMarkers(1,1)<CenterROI(1,1)
            Y_dif=sqrt((CenterBetweenMarkers(1,2)-CenterROI(1,2))^2);
            if Y_dif<50
                OriLeft=1;
                disp('Index for left orientation is:')
                disp(30+i)
                figure;imshow(detectedImg)
                A=1;
            end
        end

    end
end

if Ori>65 && Ori<115
    OriLeft=1;
    disp('Index for left orientation is:')
    disp(30+i)
end

end


%       toc
%%% end


end

close(vidWriter);
close(vidWriter2);
%%% clear cam




%% SAVE WORKSPACE
% save(['workspaces/' VideoName '.mat'])
```

D.6. MATLAB code for investigating the normal distribution

```
clear
close all
clc

filename='AutogridMarkersConfusion4.xlsx';

addpath('swtest')

T = readtable(filename);


ML_vs_CHT_masked__TP=table2array(T(1:164,73));
ML_vs_CHT_masked__FP=table2array(T(1:164,74));
ML_vs_CHT_masked__FN=table2array(T(1:164,75));
ML_vs_CHT_masked__P=table2array(T(1:164,76));
ML_vs_CHT_masked__R=table2array(T(1:164,77));
ML_vs_CHT_masked__F1=table2array(T(1:164,78));

CHT_vs_ML_Masked__TP=table2array(T(1:164,66));
CHT_vs_ML_Masked__FP=table2array(T(1:164,67));
CHT_vs_ML_Masked__FN=table2array(T(1:164,68));
CHT_vs_ML_Masked__P=table2array(T(1:164,69));
CHT_vs_ML_Masked__R=table2array(T(1:164,70));
CHT_vs_ML_Masked__F1=table2array(T(1:164,71));

CHT_vs_ML_Masked__TP=table2array(T(1:164,59));
CHT_vs_ML_Masked__FP=table2array(T(1:164,60));
CHT_vs_ML_Masked__FN=table2array(T(1:164,61));
CHT_vs_ML_Masked__P=table2array(T(1:164,62));
CHT_vs_ML_Masked__R=table2array(T(1:164,63));
CHT_vs_ML_Masked__F1=table2array(T(1:164,64));

CHT_vs_CHT_masked__TP=table2array(T(1:164,52));
CHT_vs_CHT_masked__FP=table2array(T(1:164,53));
CHT_vs_CHT_masked__FN=table2array(T(1:164,54));
CHT_vs_CHT_masked__P=table2array(T(1:164,55));
CHT_vs_CHT_masked__R=table2array(T(1:164,56));
CHT_vs_CHT_masked__F1=table2array(T(1:164,57));

CHT_masked_vs_ML_Masked_Center__TP=table2array(T(1:164,45));
CHT_masked_vs_ML_Masked_Center__FP=table2array(T(1:164,46));
CHT_masked_vs_ML_Masked_Center__FN=table2array(T(1:164,47));
CHT_masked_vs_ML_Masked_Center__P=table2array(T(1:164,48));
CHT_masked_vs_ML_Masked_Center__R=table2array(T(1:164,49));
CHT_masked_vs_ML_Masked_Center__F1=table2array(T(1:164,50));

CHT_vs_ML__TP=table2array(T(1:164,37));
CHT_vs_ML__FP=table2array(T(1:164,38));
CHT_vs_ML__FN=table2array(T(1:164,39));
CHT_vs_ML__P=table2array(T(1:164,40));
CHT_vs_ML__R=table2array(T(1:164,41));
CHT_vs_ML__F1=table2array(T(1:164,42));
```

```
figure;histogram(ML_vs_CHT_masked__TP)
figure;histogram(ML_vs_CHT_masked__FP)
figure;histogram(ML_vs_CHT_masked__FN)
figure;histogram(ML_vs_CHT_masked__P)
figure;histogram(ML_vs_CHT_masked__R)
figure;histogram(ML_vs_CHT_masked__F1);hold on;
xlabel('Difference')
ylabel('Density (absolute number)')
set(gca,'FontSize',16)
hold off

figure;histogram(CHT_vs_ML_Masked__TP)
figure;histogram(CHT_vs_ML_Masked__FP)
figure;histogram(CHT_vs_ML_Masked__FN)
figure;histogram(CHT_vs_ML_Masked__P)
figure;histogram(CHT_vs_ML_Masked__R)
figure;histogram(CHT_vs_ML_Masked__F1)

figure;histogram(CHT_vs_ML_Masked__TP)
figure;histogram(CHT_vs_ML_Masked__FP)
figure;histogram(CHT_vs_ML_Masked__FN)
figure;histogram(CHT_vs_ML_Masked__P)
figure;histogram(CHT_vs_ML_Masked__R)
figure;histogram(CHT_vs_ML_Masked__F1)

figure;histogram(CHT_vs_CHT_masked__TP)
figure;histogram(CHT_vs_CHT_masked__FP)
figure;histogram(CHT_vs_CHT_masked__FN)
figure;histogram(CHT_vs_CHT_masked__P)
figure;histogram(CHT_vs_CHT_masked__R)
figure;histogram(CHT_vs_CHT_masked__F1)

figure;histogram(CHT_masked_vs_ML_Masked_Center__TP)
figure;histogram(CHT_masked_vs_ML_Masked_Center__FP)
figure;histogram(CHT_masked_vs_ML_Masked_Center__FN)
figure;histogram(CHT_masked_vs_ML_Masked_Center__P)
figure;histogram(CHT_masked_vs_ML_Masked_Center__R)
figure;histogram(CHT_masked_vs_ML_Masked_Center__F1);hold on
xlabel('Difference')
ylabel('Density (absolute number)')
set(gca,'FontSize',16)
hold off

figure;histogram(CHT_vs_ML__TP)
figure;histogram(CHT_vs_ML__FP)
figure;histogram(CHT_vs_ML__FN)
figure;histogram(CHT_vs_ML__P)
figure;histogram(CHT_vs_ML__R)
figure;histogram(CHT_vs_ML__F1);hold on
xlabel('Difference')
ylabel('Density (absolute number)')
set(gca,'FontSize',16)
hold off
```

D.7. MATLAB code for mapping the TEM-grid orientation

The MATLAB code developed for mapping the orientation of the TEM-grid with respect to the tweezers to the Autogrid cartridge is given below.

```
clear
clc
close all

% addpath('Images')
% addpath('SolidWorksAutogridHolderImages')
addpath('FinalExperimentImages')

ExperimentName='Experiment_0_2';
ITERATION = '10_ZoomOut';

% scale=0.75;
scale=0.3;

% IM=imread('20201013_105257.jpg');
IM=imread([ExperimentName '_M.jpg']);


IM_AutogridBottom_empty=imread([ExperimentName '_B.jpg']);
IM_AutogridBottom_full=imread([ExperimentName '_A.jpg']);


% IM=imread('FIB_Auto_Full.jpg');
IMg=rgb2gray(IM);

figure;
imshow(IMg,'InitialMagnification',25);
disp('Draw a rectangle around the TEM-grid')
h_rect1 = imrect();
% Rectangle position is given as [xmin, ymin, width, height]
pos_rect1 = h_rect1.getPosition();
% Round off so the coordinates can be used as indices
pos_rect1 = round(pos_rect1);
% Select part of the image
IM_cropped = IMg(pos_rect1(2) + (0:pos_rect1(4)), pos_rect1(1) + (0:pos_rect1(3)));

figure;imshow(IM_cropped,'InitialMagnification','fit')


%% Estimate Center point using a canny edge filter
%%% This approach is not used in the current report,
%%% however it shows potential for automatic detection of TEM-grid and
%%% tweezers.

% % BW2 = rgb2gray(IM_cropped);
% % figure;imshow(BW2)
%
BW2=imadjust(IM_cropped);
% figure;imshow(BW2)
%
% [~, thresOut] = edge(BW2, 'Canny');
% % step_size = 0.55; %good for finding 1
```

```
% step_size = 0.1;
% sensitivity = thresOut + step_size;
%% sensitivity = [0 0.2];
%% sensitivity = [0.0250 0.0625];
% BW3 = edge(BW2, 'Canny', sensitivity);
%
%
% figure;imshow(BW3)
%
% s = regionprops(BW3, 'Orientation', 'PixelList', 'MajorAxisLength', '
    MinorAxisLength', 'Area', 'Eccentricity', 'Centroid','PixelIdxList');
%
% PlotOrientation(BW3,s)
%
% PlotOrientation2(s)
%
% A_v=zeros(length(s),1);
% for ii=1:length(s)
%     A_v(ii)=s(ii).Area;
% end
% Or_I2=find(A_v==max(A_v));
%
% CenterTEM=s(Or_I2).Centroid;

%% Choose TEM-grid center location and marker
figure;imshow(IM_cropped,'InitialMagnification',400)

% Uncomment for enabling an assisting grid.
% axis on;
% [rows, columns, numberOfColorChannels] = size(IM_cropped);
% hold on;
% for row = 1 : 5 : rows
%   line([1, columns], [row, row], 'Color', 'r');
% end
% for col = 1 : 5 : columns
%   line([col, col], [1, rows], 'Color', 'r');
% end
hold on
% p1=plot(CenterTEM(1),CenterTEM(2),'ro','LineWidth',1.5);
% legend([p1],{'Estimated Center Location'})
disp('Choose the center of the TEM-grid')
[Center_x,Center_y] = ginput(1);
p2=plot(Center_x,Center_y,'bx','LineWidth',1.5);
% legend([p1 p2],{'Estimated Center Location','Picked Center Location'})
legend([p2],{'Picked Center Location'})

disp('Choose the center of the Marker')
[Marker_x,Marker_y] = ginput(1);
p3=plot(Marker_x,Marker_y,'rx','LineWidth',1.5);
% legend([p1 p2 p3],{'Estimated Center Location','Picked Center Location','Picked
    Marker Location'})
legend([p2 p3],{'Picked Center Location','Picked Marker Location'})
hold off


%% Choose Tweezer orientation
```

```matlab

figure;
imshow(IMg,'InitialMagnification',25);
disp('Draw a rectangle around the black part of the tweezers')
h_rect2 = imrect();
% Rectangle position is given as [xmin, ymin, width, height]
pos_rect2 = h_rect2.getPosition();
% Round off so the coordinates can be used as indices
pos_rect2 = round(pos_rect2);
% Select part of the image
IM_cropped2 = IMg(pos_rect2(2) + (0:pos_rect2(4)), pos_rect2(1) + (0:pos_rect2(3)));


figure;imshow(IM_cropped2,'InitialMagnification',100)

[rows, columns, numberOfColorChannels] = size(IM_cropped2);
hold on;
for row = 1 : 25 : rows
  line([1, columns], [row, row], 'Color', 'r');
end
for col = 1 : 25 : columns
  line([col, col], [1, rows], 'Color', 'r');
end

disp('Pick the middle of the base of the tweezer')
[Base_x,Base_y] = ginput(1);
p21=plot(Base_x,Base_y,'bx','LineWidth',1.5);
legend([p21],{'Picked Base Location'})


disp('Pick the middle of the tip of the tweezer')
[Tip_x,Tip_y] = ginput(1);
p22=plot(Tip_x,Tip_y,'rx','LineWidth',1.5);
legend([p21 p22],{'Picked Base Location','Picked Tip Location'})

hold off


%% Find orientation of TEM-grid w. r. t. the x-axis

MarkerTEMcoordinates=[Marker_x;Marker_y];
CenterTEM=[Center_x;Center_y];

%Vector from the center of the TEM-grid to the marker in pixel-coordinates
Center_to_marker_v_pix=MarkerTEMcoordinates-CenterTEM;

%Changin to normal coordinates
Center_to_marker_v(1)=Center_to_marker_v_pix(1);
Center_to_marker_v(2)=-Center_to_marker_v_pix(2);

%%
% % Test with angle
% Center_to_marker_v(1)=1;
% Center_to_marker_v(2)=-1;


```

```

Center_to_marker_L=sqrt((Center_to_marker_v(1)^2)+(Center_to_marker_v(2)^2));

% Calculate angle
% atand(Center_to_marker_v(2)/Center_to_marker_v(1))
AngleMarkerCenter1=asind(Center_to_marker_v(2)/Center_to_marker_L);

% Convert to circular angle -180 <--> +180
if Center_to_marker_v(1)<0
    if Center_to_marker_v(2)>0
        AngleMarkerCenter2=180-AngleMarkerCenter1;
    elseif Center_to_marker_v(2)<0
        AngleMarkerCenter2=-180-AngleMarkerCenter1;
    elseif Center_to_marker_v(2)==0
        AngleMarkerCenter2=180;
    end
elseif Center_to_marker_v(1)==0
    AngleMarkerCenter2=AngleMarkerCenter1;
elseif Center_to_marker_v(1)>0
    AngleMarkerCenter2=AngleMarkerCenter1;
end

if AngleMarkerCenter2<0
    AngleMarkerCenter3=AngleMarkerCenter2+360;
else
    AngleMarkerCenter3=AngleMarkerCenter2;
end


disp('Angle of the marker on TEM-grid with respect to the x-axis is:')
disp('(angle can range from 0 <--> 360)')
disp(AngleMarkerCenter3)

%%
figure;imshow(BW2,'InitialMagnification',200)
hold on
plot([MarkerTEMcoordinates(1);CenterTEM(1)],[MarkerTEMcoordinates(2);CenterTEM(2)],'
    r','LineWidth',1.5)
plot([MarkerTEMcoordinates(1);CenterTEM(1)],[MarkerTEMcoordinates(2);CenterTEM(2)],'
    rx','LineWidth',1.5)
hold off


%% Find the orientation of the tweezers w. r. t. the x-axis


TweezerTipcoordinates=[Tip_x;Tip_y];
TweezerBase=[Base_x;Base_y];

%Vector from the center of the TEM-grid to the marker in pixel-coordinates
Base_to_Tip_v_pix=TweezerTipcoordinates-TweezerBase;

%Changin to normal coordinates
Base_to_Tip_v(1)=Base_to_Tip_v_pix(1);
Base_to_Tip_v(2)=-Base_to_Tip_v_pix(2);

```

```
% Test with angle
% Center_to_marker_v(1)=-10;
% Center_to_marker_v(2)=10;



Base_to_Tip_L=sqrt((Base_to_Tip_v(1)^2)+(Base_to_Tip_v(2)^2));

% Calculate angle
% atand(Center_to_marker_v(2)/Center_to_marker_v(1))
AngleTweezer1=asind(Base_to_Tip_v(2)/Base_to_Tip_L);

% Convert to circular angle -180 <--> +180
if Base_to_Tip_v(1)<0
    if Base_to_Tip_v(2)>0
        AngleTweezer2=180-AngleTweezer1;
    elseif Base_to_Tip_v(2)<0
        AngleTweezer2=-180-AngleTweezer1;
    elseif Base_to_Tip_v(2)==0 && Base_to_Tip_v(1)<0
        AngleTweezer2=180;
    end
elseif Base_to_Tip_v(1)>0
    AngleTweezer2=AngleTweezer1;
end

if AngleTweezer2<0
    AngleTweezer3=AngleTweezer2+360;
else
    AngleTweezer3=AngleTweezer2;
end


disp('Angle of the tweezers with respect to the x-axis is:')
disp('(angle can range from 0 <--> 360)')
disp(AngleTweezer3)

figure;imshow(IM_cropped2,'InitialMagnification',100)
hold on
plot([TweezerTipcoordinates(1);TweezerBase(1)],[TweezerTipcoordinates(2);TweezerBase
    (2)],'r','LineWidth',1.5)
plot([TweezerTipcoordinates(1);TweezerBase(1)],[TweezerTipcoordinates(2);TweezerBase
    (2)],'rx','LineWidth',1.5)
hold off


AngleTEM_Tweezers=AngleMarkerCenter3-AngleTweezer3;

if AngleTEM_Tweezers<0
    AngleTEM_Tweezers=360+AngleTEM_Tweezers';
end

disp('Angle of the TEM-grid with respect to the tweezers')
disp(AngleTEM_Tweezers)
```

```
figure;imshow(IMg,'InitialMagnification',25)
hold on
plot([TweezerTipcoordinates(1)+pos_rect2(1);TweezerBase(1)+pos_rect2(1)],[
    TweezerTipcoordinates(2)+pos_rect2(2);TweezerBase(2)+pos_rect2(2)],'r','LineWidth
    ',4)
plot([TweezerTipcoordinates(1)+pos_rect2(1);TweezerBase(1)+pos_rect2(1)],[
    TweezerTipcoordinates(2)+pos_rect2(2);TweezerBase(2)+pos_rect2(2)],'ro','
    LineWidth',4)
plot([MarkerTEMcoordinates(1)+pos_rect1(1);CenterTEM(1)+pos_rect1(1)],[
    MarkerTEMcoordinates(2)+pos_rect1(2);CenterTEM(2)+pos_rect1(2)],'r','LineWidth'
    ,4)
plot([MarkerTEMcoordinates(1)+pos_rect1(1);CenterTEM(1)+pos_rect1(1)],[
    MarkerTEMcoordinates(2)+pos_rect1(2);CenterTEM(2)+pos_rect1(2)],'ro','LineWidth'
    ,4)
% plot([TweezerTipcoordinates(1);TweezerBase(1)],[TweezerTipcoordinates(2);
    TweezerBase(2)],'rx','LineWidth',1.5)
hold off


%%



%% TopSide
figure;imshow(IM_AutogridBottom_full,'InitialMagnification',60)

%
% AngleTEM_Tweezers=-350;
% TopCenterCo=[612; 634];

% CenterCo=[985; 613];
hold on
disp('Select the center')
[Cen_x,Cen_y] = ginput(1);
CenterCo=[Cen_x; Cen_y];
plot(CenterCo(1),CenterCo(2),'ro','LineWidth',2)


AngleTEM_TweezersT=-AngleTEM_Tweezers+180;

if AngleTEM_TweezersT>360
    AngleTEM_TweezersT=AngleTEM_TweezersT-360;
end

% Center_to_marker_v_pix2=Center_to_marker_v_pix.*scale;
% TopMarkerCo=TopCenterCo+Center_to_marker_v_pix2;
% R_vec_co=round(Center_to_marker_v_pix)
unit_v=[1;0];
Qr=[cosd(AngleTEM_TweezersT) -sind(AngleTEM_TweezersT);
sind(AngleTEM_TweezersT) cosd(AngleTEM_TweezersT)];

unit_v_rot=Qr*unit_v;
% plot([0,unit_v_rot(1)],[0,unit_v_rot(2)])

CenAuto_to_MarkerEM=Center_to_marker_L.*unit_v_rot.*scale;
% CenAuto_to_MarkerEM=unit_v_rot.*1;
```

```
TopMarkerCo=CenterCo+CenAuto_to_MarkerEM;

%%
hold on
plot(CenterCo(1),CenterCo(2),'ro','LineWidth',2)
plot(TopMarkerCo(1),TopMarkerCo(2),'ro','LineWidth',2)
plot([CenterCo(1);TopMarkerCo(1)],[CenterCo(2);TopMarkerCo(2)],'r','LineWidth',2)

hold off


%% EmptyAutogrid


figure;imshow(IM_AutogridBottom_empty,'InitialMagnification',60)
hold on
plot(CenterCo(1),CenterCo(2),'ro','LineWidth',2)
plot(TopMarkerCo(1),TopMarkerCo(2),'ro','LineWidth',2)
plot([CenterCo(1);TopMarkerCo(1)],[CenterCo(2);TopMarkerCo(2)],'r','LineWidth',2)

hold off



%% Comparison

figure;imshow(IM_AutogridBottom_full,'InitialMagnification',60)
hold on
plot(CenterCo(1),CenterCo(2),'ro','LineWidth',2)
[Com_x,Com_y] = ginput(1);
plot(Com_x,Com_y,'ro','LineWidth',2)
plot([CenterCo(1);Com_x],[CenterCo(2);Com_y],'r','LineWidth',2)
hold off


RelCom_x=Com_x-CenterCo(1);
RelCom_y=Com_y-CenterCo(2);

% pixel to normal coordinates
RelCom_y=-RelCom_y;

RelMarker_x=TopMarkerCo(1)-CenterCo(1);
RelMarker_y=TopMarkerCo(2)-CenterCo(2);

RelMarker_y=-RelMarker_y;


ComAngle=atand(RelCom_x/RelCom_y);
MarkerAngle=atand(RelMarker_x/RelMarker_y);

AngleDifference=MarkerAngle-ComAngle


string3='.png';
folder= 'FinalExperimentImages\Matlab_images\';
saveas(figure(8),[folder ExperimentName '_TweezerTEMgridOri' ITERATION string3])
```

```
saveas(figure(9),[folder ExperimentName '_MappedOriFull' ITERATION string3])
saveas(figure(10),[folder ExperimentName '_MappedOriEmpty' ITERATION string3])
saveas(figure(11),[folder ExperimentName '_OriSelected' ITERATION string3])
```